

5 Detailed study of the efficiency in simulation

5.1 Introduction

The raw yield extracted from data have to be corrected for the efficiency of the experimental setup. The best situation is when the effect of the detector on the observed signal can be calculated analytically, but the current heavy ion experiments are too complicated for analytical treatment. The correction factors due to efficiency was studied using detailed Monte-Carlo simulation of the CERES setup.

The total efficiency was factorized into three parts: acceptance, tracking efficiency and peak extraction efficiency. The idea behind was to separate acceptance, which is weakly dependent on the details of the Monte-Carlo and determined by the geometrical shape of the detector from the parts that depend on the details of the simulation procedure.

Acceptance for a single track is defined as a fraction of tracks, which momentum is in a fiducial volume of the polar angle and transverse momentum. For pairs from K_S^0 the acceptance means a fraction of the primary K_S^0 particles, which both decay products fall into the single track acceptance and have certain orientation with respect to the primary track.

Tracking efficiency is defined as a fraction of reconstructed tracks (pairs) out of those that fall into the acceptance. The efficiency is not independent on the acceptance assumed, due to lower tracking efficiency at the borders of detector. More generous definition of the acceptance will lead to lower efficiency and a strict definition of the acceptance to higher efficiency. The product of acceptance and efficiency will be called overall efficiency. Actually, the overall efficiency has a direct interpretation, and the acceptance and the efficiency are useful terms to separate sources of the lost tracks.

After a pair is reconstructed, decision have to be made whether the pair comes from the real primary track or from the combinatorial background. This decision is based on the invariant mass of the pair. The peak extraction efficiency factorize with the overall efficiency and four methods of peak extraction will be discussed and their efficiencies presented.

5.2 Simulation chain

The Monte-Carlo framework for CERES experiment is composed of four cooperating programs. Two of these programs are specific for the analysis performed and two are universal simulation tools used by the CERES collaboration. The input and the output of the programs is standardized and they are used consecutively.

The first program, analysis specific, is used to generate primary tracks. These tracks are then propagated by the standard, GEANT [42] based program, and RAWMC digits are its output. The digits are processed by CERES analyzer which produces space points out of digits and performs tracking. Finally the reconstructed tracks are processed by V_0 analysis program to evaluate the efficiency of the K_S^0 reconstruction.

The notion MC, was used in the previous chapter for the Multiplicity Counter. In this chapter it stands for Monte-Carlo and exactly for the tandem of GEANT with the CERES setup and Monte-Carlo analyzer. These two programs are standard tools used by the CERES collaboration and they were not modified in this work.

The details of the simulation chain procedure is the following:

1. The primary K_S^0 tracks, following the Boltzmann distribution with $T = 210$ MeV and $y \in (1.85, 2.45)$ are generated. Since the resulting efficiencies are (weakly) dependent on the parameters of the distribution thus the temperature for the MC have to be iteratively adjusted. The generation is done in a Root macro and data are stored in text files, each containing 10 000 events with one K_S^0 . Additionally, for technical reasons two muons are generated with every event.
2. Every event is processed by the GEANT with CERES setup. The K_S^0 are propagated and decayed by the GEANT. If none of the decay products of the K_S^0 hits the detector the original particle is not present in the MC output. This feature was introduced to suppress gammas from bremsstrahlung which did not produce any hit. Storing all gammas and electrons from showers will blow-up output files. For the analysis of weakly decaying particles one would prefer to keep these primaries. The obstacle was work around injecting two muons and using the input text files for the final analysis.
3. Data are analyzed with Monte-Carlo analyzer which is in principle the same program as used for the reconstruction of real events (step2). The analyzer can be used in two ways: as a clean MC or an overlay MC. In the clean MC only the hits created by the simulation are present. In the overlay MC the signal – hits from tracks resulting from

a decaying K_S^0 are overlay with the raw-data events. The advantage of the clean MC is that it reproduces gross properties of the detector and requires less computing time and disk space. The overlay MC is more correct in particularly when deterioration due to additional hits is important: studying the number of hits per track or the invariant mass resolution. For tracks falling in the middle of the detector there is no difference in the reconstruction efficiency between clean and overlay MC. Moving to low polar angles, the occupancy increases and the efficiency falls in the overlay MC, but this feature is not represented in the clean MC. Similarly for large polar angles, the deterioration of performance is not reproduced in the clean MC. Data presented in the following sections were obtained with the overlay MC.

4. Reconstructed hits and tracks are associated with the simulated ones. The digits in the RAWMC format contain information, from which track they originate. This information is propagated further during the processing and for the reconstructed hit is can be said from which track it originate. If the reconstructed track is composed out of hits belonging to a given GEANT track, the tracks are associated. Track association algorithm have two parameters. The first is the maximum distance between simulated and reconstructed hit, measured in standard deviations of the expected resolution at this point. This parameter is usually set to 5. The second parameter is the purity: the fraction of the hits in the track that originate from this given simulated track, this parameter is usually set to 60%.
5. After the analyzer, the data are in the format corresponding to the *step2* output. Then the main part of the analysis takes place – the reconstruction of the secondaries and evaluation of the efficiency. This program will be described in great detail in the next section.

5.3 Analysis procedure

5.3.1 Phase-space segmentation

The transverse momentum – rapidity space of the primary K_S^0 is segmented into a number of bins. Five equally sized bins in the rapidity space each 0.15 units wide are created, spanning the range 1.85 – 2.60, the bins are numbered from (1) to (5). The three central bins (2)–(4) spanning 2.00 – 2.45 have full acceptance in the transverse momentum. The side bins have only some small fraction of the transverse momentum in the acceptance.

The transverse momentum is divided into 9 bins spanning area $p_T < 1.6$ MeV/c. The first 6 bins have width equal 100 MeV/c, next two bins have width equal 200 MeV/c and

finally the last bins are 300 MeV/c wide. The size of the bins is increased to compensate for the diminishing signal.

5.3.2 Analysis chain

The most important part of the simulation procedure is the analysis of the MC output by the V_0 analyzer. In this program data are processed in steps, after every step the properties of the primary K_S^0 are histogrammed. Each step reduces the number of K_S^0 left for the further analysis. The steps are the following:

1. The distribution of the transverse momentum and rapidity of the primary K_S^0 is reconstructed using data in the text files.
2. Output of the MC is read. The existence of K_S^0 in MC data is checked, its (p_T, y) is used for further analysis.
3. Number of decay products of the K_S^0 is counted. The fraction with 2 pions shall be equal to the branching ratio. Additional complication is the fact that the number of decay products is correlated with the probability neither of them will hit the active volume.
4. The polar angle of the MC track is checked. Three values of the lower cut were studied $\theta > 0.12, 0.13, 0.14$ rad and the upper cut is $\theta < 0.26$ rad. Since the particle can scatter at the path between target and entrance of the TPC the actual cut is extended by 5 mrad in both directions. This extend will be trimmed by a cut on the actual polar angle of the reconstructed track in step 8. The overall acceptance for the three scenarios will be compared further.
5. The orientation of the decay is checked using Armenteros–Podolanski space. The Armenteros cut is set to $\alpha \in (-0.5, 0.5) \wedge q_T \in (0.08, 0.5)$ and is applied on the α and q_T using MC track parameters. The definition of the Armenteros variables α and q_T are presented in Eqs. 4.23–4.24.
6. The existence of the TPC segments associated with both MC tracks is checked. At this point the refitting procedure is applied. In the *step2* format, used by MC, the local angles are not stored and to obtain them the Fitter program is used. This program uses the same class for refitting as used during *step3c* production. The refitting procedure ensures real data and MC data are equally processed.
7. The single track cuts are applied, following that in data:

- polar angle of the track, according to the cut performed in the step 4.
- number of fitted hits, dependent on the polar angle:

$$\begin{aligned} N_{hits} &\geq N_0 & \theta &\in (0.12, 0.22) \\ N_{hits} &\geq N_0 - (\vartheta - 0.22) * 150 & \theta &\in (0.22, 0.28) \end{aligned} \quad (5.1)$$

with N_0 set to 10, 12 and 14. The results presented are performed for $N_0 = 10$. Other values will be used to estimate the systematical error.

- transverse momentum $p_T > 100$ MeV/c and $p_T > 150$ MeV/c, the value presented here are for $p_T > 100$ MeV/c.

8. The pair cuts are applied:

- Armenteros cut – the same as in step 5 but performed using the variables from the reconstructed TPC tracks.
- opening angle cut $\psi \in (0.1, 0.45)$ rad.

9. The transverse momentum and rapidity is recalculated using data from the reconstructed TPC tracks. This step does not reduce the number of events but scatter them between bins.

10. The invariant mass is calculated using two momentum measurements: combined momentum and three-parameter fit.

The steps from 1 to 5 define the acceptance. These steps shall be weakly dependent on the correctness of the MC. The steps 6–9 define efficiency and are dependent on the details of the MC program. The steps 9 and 10 will be used to evaluate the efficiency of the peak extraction. The final numbers and effect of each step on the number of K_S^0 will be discussed in detail in the following subsections.

5.4 Results

5.4.1 Single track efficiency

The efficiency as a function of the azimuthal angle is shown on the first panel of Fig. 5.1. The efficiency is composed out of a flat part, at the level of 70 – 80% with a chamber structure visible. Additionally there are two holes: one deep at $\phi \simeq -3$ rad and second, less pronounced at $\phi \simeq -0.5$ rad.

The tracking efficiency as a function of the polar angle is shown on the consecutive panels. The upper right panel shows the whole range while the following panels zoom on the

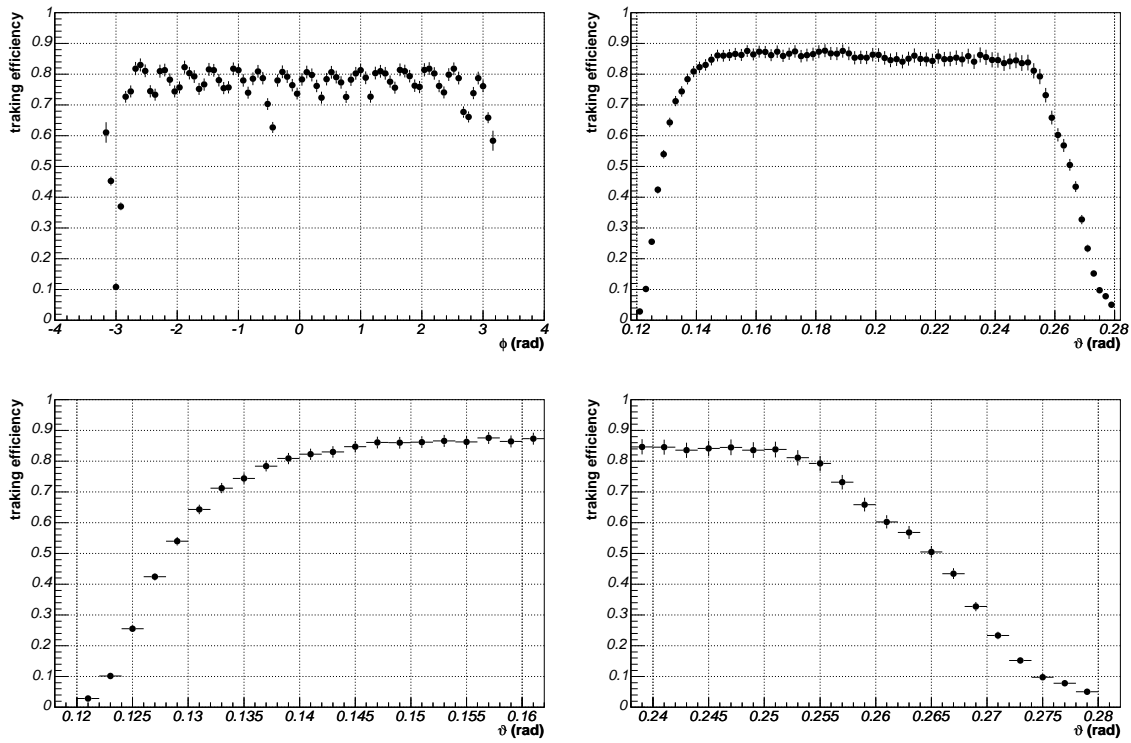


Figure 5.1: Single track efficiency in a function of the polar and azimuthal angle. Left top: efficiency as a function of azimuthal angle with chamber structure visible. Right top: efficiency as a function of polar angle. Bottom: efficiency as a function of the polar angle zoomed on the borders of the acceptance.

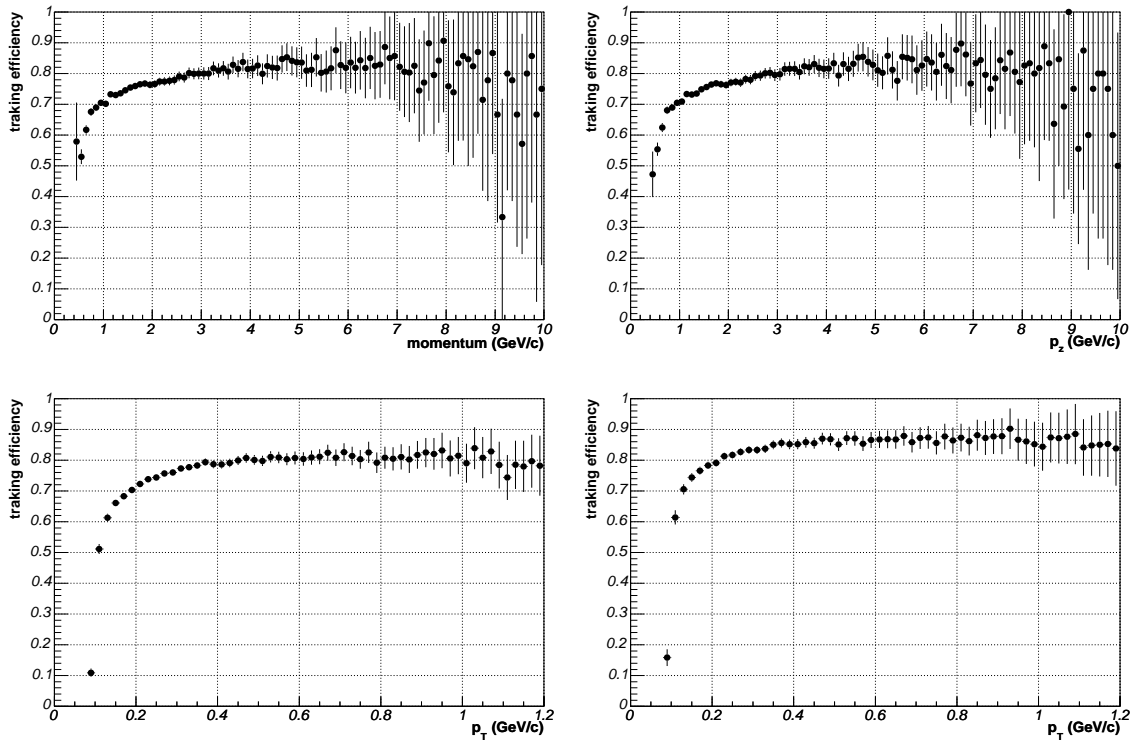


Figure 5.2: Single track efficiency. Left top: efficiency as a function of total momentum. Right top: efficiency as a function of the longitudinal momentum. Bottom: efficiency as a function of transverse momentum for two definition of the fiducial volume: $\theta > 0.12$ rad. (left) and $\theta > 0.13$ rad. (right)

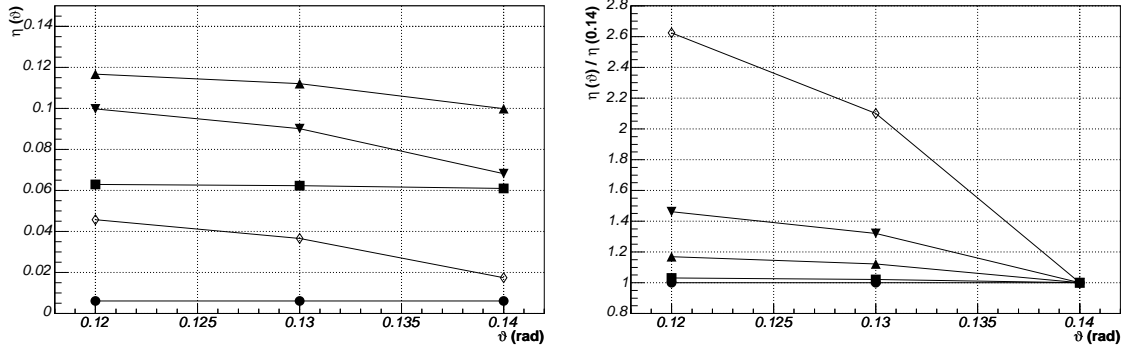


Figure 5.3: K_S^0 efficiency in rapidity bins as a function of the polar angle cut. Rapidity bins are shown by symbols: (1) – circles, (2) – squares, (3) – pointing up triangles, (4) – pointing down triangles, (5) – chevrons. Left panel: efficiency as a function of the cut. Right panel: efficiency divided by the reference efficiency with $\theta > 0.14$ rad.

edges: $\theta \in (0.12, 0.16)$ rad and $\theta \in (0.24, 0.28)$ rad. The efficiency rises slowly starting at $\theta \simeq 0.12$ rad and saturates at $\theta \simeq 0.14$ rad at the level of 80%. In this area the tracks have a full length in the TPC. The efficiency start falling for $\theta > 0.25$ rad and no tracks are reconstructed when $\theta > 0.28$ rad.

The efficiency as a function of the total and parallel momentum is shown in the upper row in Fig. 5.2. The second row shows the efficiency as a function of the transverse momentum for the two cuts on the polar angle $\theta > 0.12$ rad (left) and $\theta > 0.13$ rad (right). The efficiency is very low at $p_T \simeq 100$ MeV/ c and grows quickly at $p_T \simeq 150$ MeV/ c and finally slowly saturates. The stricter the cut on the acceptance, the higher the efficiency and faster the saturation.

5.4.2 Optimization of the polar angle cut

The pair efficiency is strongly dependent on the cut on the polar angle. With the Monte-Carlo framework discussed here it is possible to optimize the cut on the polar angle for a given rapidity range. The maximum theta cut was set to $\theta < 0.26$ rad, at the single track efficiency at the level of 60%. The optimization is performed for the minimum θ cut.

The overall pair efficiency as a function of the minimum theta cut is presented in Fig. 5.3. The rapidity bins are shown as different symbols, described in the figure caption. Releasing the cut will increase the signal in bins (3) – (5).

To better estimate then gain the results for $\theta = 0.12$ rad and $\theta = 0.13$ rad where divided by the reference value obtained for the cut $\theta = 0.14$ rad. The results are displayed in the

right panel in Fig. 5.3.

The low rapidity bins (1) and (2) are not influenced, and the higher the rapidity the higher the gain when releasing the cut. For the uppermost bin the difference is by a factor of 2.6. The increase in the efficiency is most pronounced changing cut from $\theta = 0.14$ rad to $\theta = 0.13$ rad. Changing the cut from $\theta = 0.13$ rad to $\theta = 0.12$ rad does not increase the efficiency substantially but in this area the precise understanding of the tracking efficiency becomes crucial. In particular the momentum resolution for the tracks without a hit in the first and the last active plane is not fully understood.

From the Monte-Carlo studies one can conclude, the optimum cut giving high efficiency and independence on the details of the simulation is for $\theta = 0.13$ rad. The higher cut $\theta = 0.14$ rad can be used for the evaluation of the systematical error. In real data it is visible, with the cut $\theta = 0.13$ rad the bin (5) can provide a partial spectrum, but with the cut $\theta = 0.14$ rad only three bins (2) – (4) can provide a signal. Thus the cut of $\theta = 0.13$ rad. was selected and the results will be discussed in detail only for the polar angle cut $\theta \in (0.13, 0.26)$ rad.

5.4.3 Acceptance and efficiency in rapidity bins

The acceptance for each rapidity bin is presented in the first panel in Fig. 5.4. The acceptance exceeds 16% for the tree central bins and falls below 7% for side bins.

The efficiency follows similar pattern, and is the highest for the central bins at the level of 60 – 70% and falls below 50% for side bins. The reason for the lower efficiency in the side bins are the fall of the single track efficiency at the border of the polar acceptance.

The overall efficiency is shown in the next panel. The highest efficiency, for the (3) bin exceeds 12%. The overall efficiency is low, but it is dominated by the geometrical acceptance.

The expected relative strength of the signal is shown on the next panel. Higher yield closer to midrapidity partially compensate for the low acceptance for the bin (5). The first bin is unfavored by the acceptance, the efficiency and the low yield and thus practically no signal is present in this bin. The sizable signal can be expected in the tree central bins and the weak signal in the (5) bin.

The number of events surviving every cut is shown in Fig. 5.5. The first panel shows the number of events after a given cut is applied, and the second panel shown fraction of the events rejected by a given cut. The Fig 5.6 shows the same for bins (2)–(5).

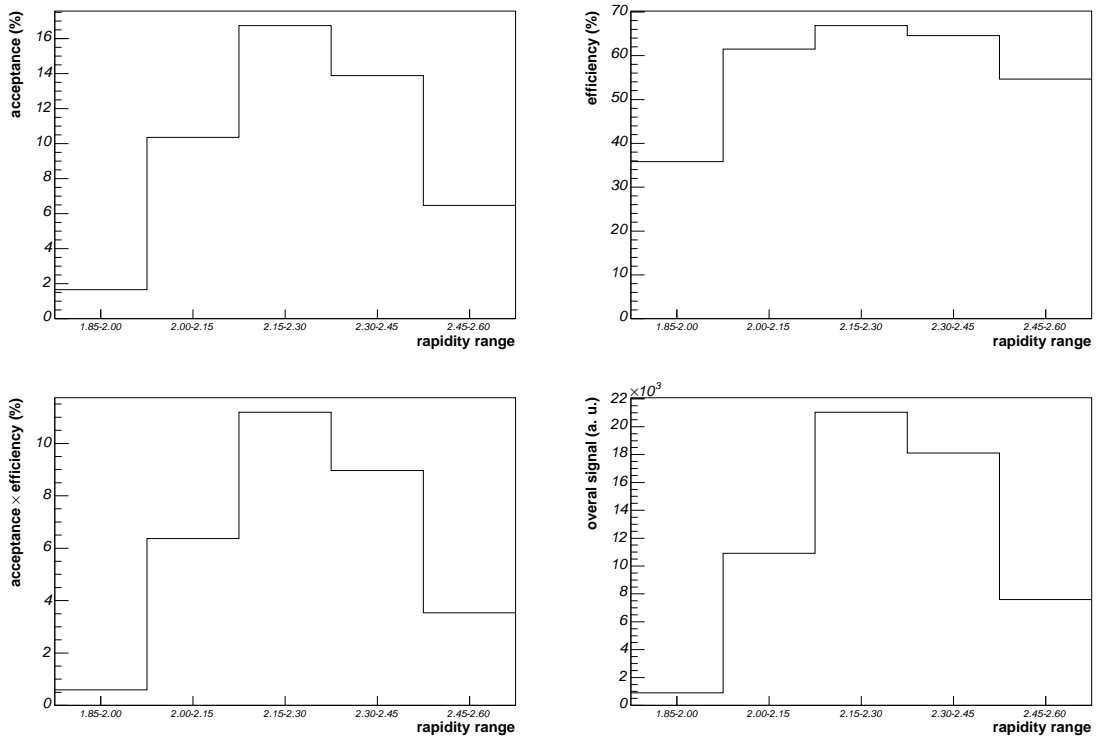


Figure 5.4: Signal, acceptance and efficiency in the rapidity bins

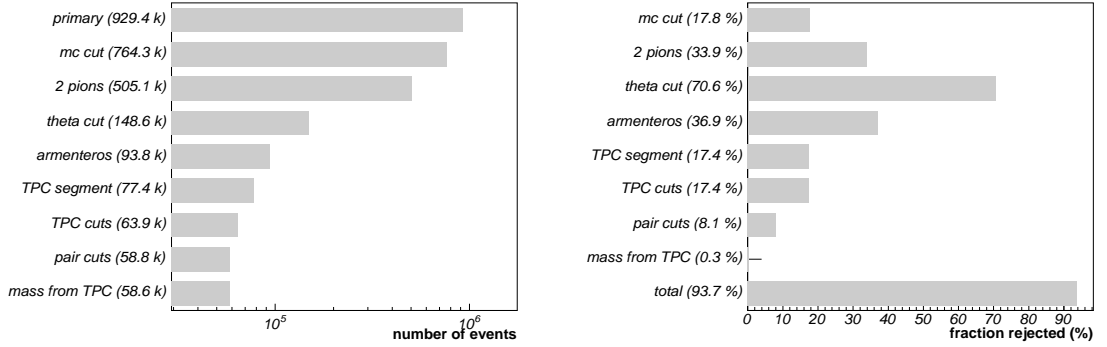


Figure 5.5: Impact of different cuts. Left panel: a number of events after a given cut, right panel: fraction of events rejected by a given cut.

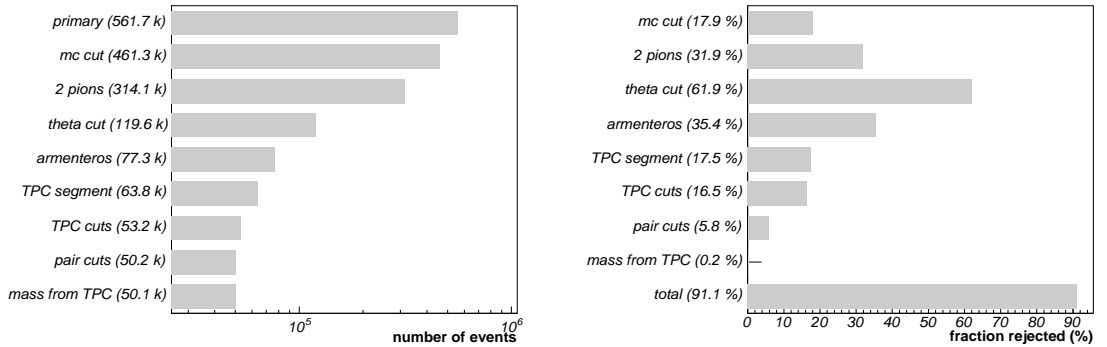


Figure 5.6: Impact of different cuts for bins (2)–(4). Left panel: a number of events after a given cut, right panel: fraction of event rejected by a given cut.

The most important cuts is the polar angle and Armenteros cut, rejecting respectively 70% and 35% of the K_S^0 . The two cuts involving the details of the TPC simulation are rejecting around 17% each.

5.4.4 Acceptance and efficiency in transverse momentum bins

The overall signal in each (p_T, y) bin after full reconstruction chain is shown in the first panel in Fig. 5.7. The colors represents different rapidity bins: black for bin (1), red for bin (2), green for bin (3) and blue for bin (4). The highest signal is in the first bin of width 200 MeV/c. Due to adjusted bin width the signal is almost constant over a wide range of the transverse momentum spectrum.

The efficiencies after different steps are displayed on the consecutive panels. The efficiency due to decay topology, shown in the first panel in Fig. 5.7 is at the level of 80% – 90%

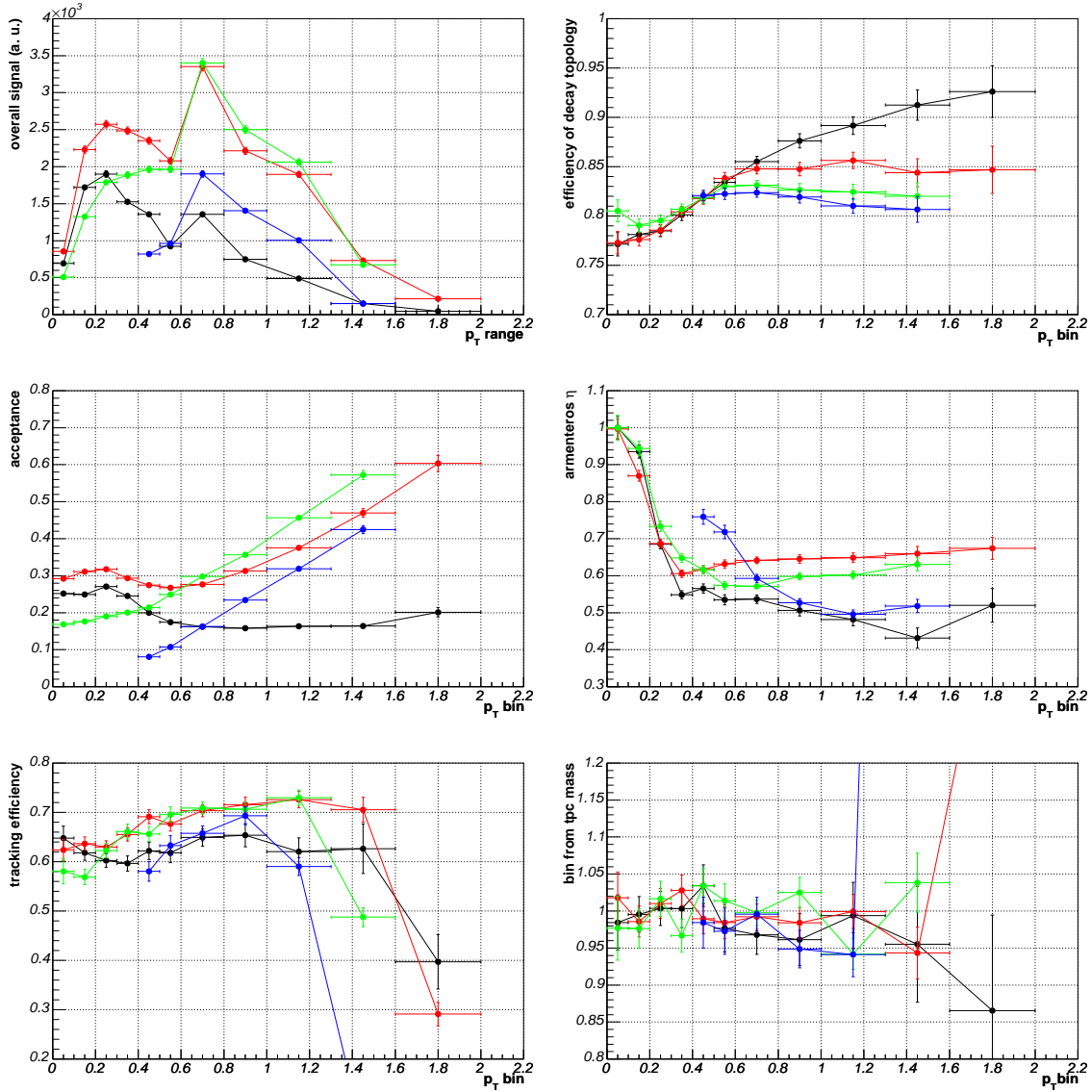


Figure 5.7: Details of the acceptance and efficiency. In consecutive panels: total signal expected in every bin, efficiency of decay topology, acceptance due to polar angle cut, acceptance due to Armenteros cut, efficiency due to track reconstruction and due to resolution of the mass. Rapidity bins depicted in colors: (2) – black, (3) – red, (4) – green, (5) – blue.

and is increasing with the transverse momentum. The higher the transverse momentum, the lower the opening angle and thus the lower probability, neither of the tracks will hit active volume of the TPC, taking into account, all generated K_S^0 in the discussed rapidity range are heading toward the TPC.

The acceptance of the fiducial volume is shown on the next panel. The acceptance increase with the transverse momentum for bins (3) – (5) and stays relatively flat for the bin (2). At transverse momentum of $p_T \simeq 200$ MeV/ c there is a non-monotonic behavior of the acceptance, this is due to change of the accepted topology from back-to-back with large opening angle to the topology with the two tracks heading in the same part of the detector.

The acceptance is strongly connected with the decay orientation, which can be seen on the next panel displaying efficiency of the Armenteros cut. If a decay would be oriented randomly in θ with respect to the direction of the K_S^0 the efficiency would be around 60%. For low transverse momenta, only these K_S^0 are accepted which decay parallel to the direction of K_S^0 , decay products open wide and hit opposite sides of the TPC. Due to this topology the Armenteros cut does not remove any K_S^0 . With increasing transverse momentum this topology is less pronounced and when $p_T > 500$ MeV/ c the Armenteros cut rejects around 60% of the pairs – for these particles the decay topology in θ is not correlated with the acceptance. The area of steep variation of the efficiency of the Armenteros cut is the same as non-monotonic area in the acceptance discussed in the previous paragraph.

The tracking efficiency is presented in the next panel. The efficiency is relatively constant and is at the level 60% – 70%. The pair cuts, in particular opening angle cut are included into tracking efficiency which is visible as lose of efficiency of high momentum kaons. The strong opening angle cut of $\psi > 0.1$ rad kills the high transverse momentum spectrum in rapidity bins (4) and (5). This strong cut is not justified by MC but by the shape of the invariant mass in data. The high momentum spectrum were sacrificed to obtain a reliable yield of the kaons. The option of momentum dependent opening angle cut was studied in data and the results will be used for the estimation of the systematic error.

In the MC studies the (p_T, y) bin of the K_S^0 was taken form the Monte-Carlo, in reality the (p_T, y) bin is taken from the TPC tracks momenta. The reconstructed tracks and thus also the momentum of the pair have a finite resolution. Due to this fact some of the primary tracks are histogramed into a wrong bin. When the spectrum is falling rapidly, as it does at high momentum, the resolution effect smears the signal into higher momentum and an artificial increase in the slope parameter is observed. The correction factor due to this effect is shown on the next panel. The correction is small, well below 5% and some trend with the mass is visible.

The overall efficiency is shown on the Fig. 5.8. For the first bin, the efficiency drops with

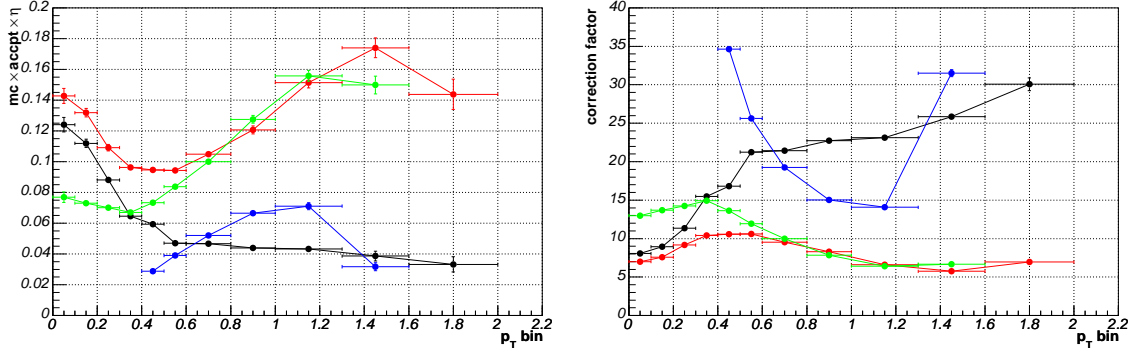


Figure 5.8: Overall efficiency and the correction factor, colors as in Fig 5.7.

the increasing transverse momentum, for the highest bin it increases and for the middle bin it have a U-shape with minimum at 500 MeV/c. The inverse of the efficiency – the correction factor is display on the next panel. It ranges form 7 up to 25, the flattest is the middle bin.

5.5 Peak extraction efficiency

The reconstructed invariant mass is histogrammed for every (p_T, y) bin. The transverse momentum and rapidity is taken using information from the TPC tracks, as in the real data. The results for both possibilities of choosing the momentum: combined momentum and three-parameter fit will be presented.

The distribution of the invariant mass using *pcomb* for three rapidity bins are shown in Figs. 5.9–5.11. consecutive panels presents consecutive transverse momentum bins. The width of the bin of the spectra is $5 \text{ MeV}/c^2$ as used in data.

Each invariant mass spectrum was fit with a Gaussian and the parameters of the fits are shown in Fig. 5.12. The left column shows the results for the scenario using combined momentum and the right column using three-parameter fit momentum. For most of the points, for both scenarios, the mean value is off the PDG value of $m = 497.6 \text{ MeV}$ by 1 MeV. The resolution behaves differently for the two scenarios. When combined momentum is used, the best resolution is achieved for the low transverse momentum at the level of $\sigma = 10 \text{ MeV}/c^2$ and increases steeply with the transverse momentum up to $\sigma = 30 \text{ MeV}/c^2$ for high p_T tracks. When *pcor3* is used, the resolution for low transverse momentum K_S^0 is 20% worse, but the resolution deteriorates slowly with the increasing transverse momentum reaching resolution $\sigma = 20 \text{ MeV}/c^2$ for the highest transverse momenta.

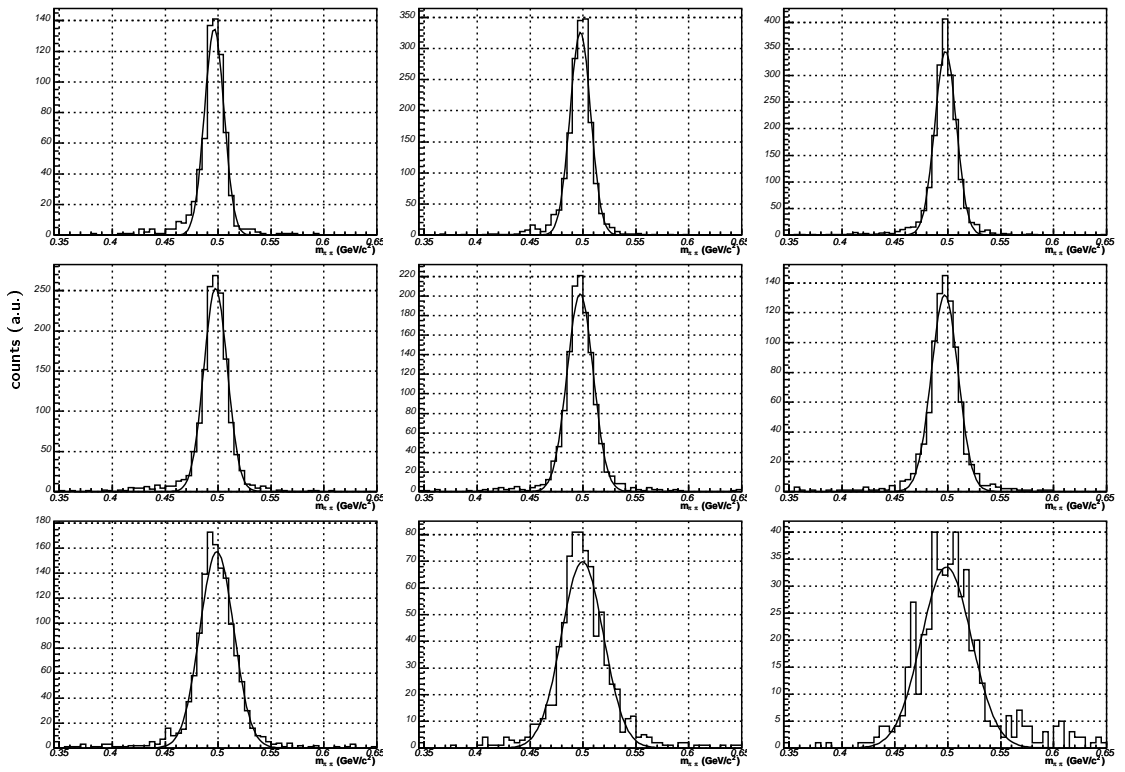


Figure 5.9: Invariant mass spectra for rapidity bin $y \in (2 - 2.15)$. Consecutive panels show transverse momentum bins.

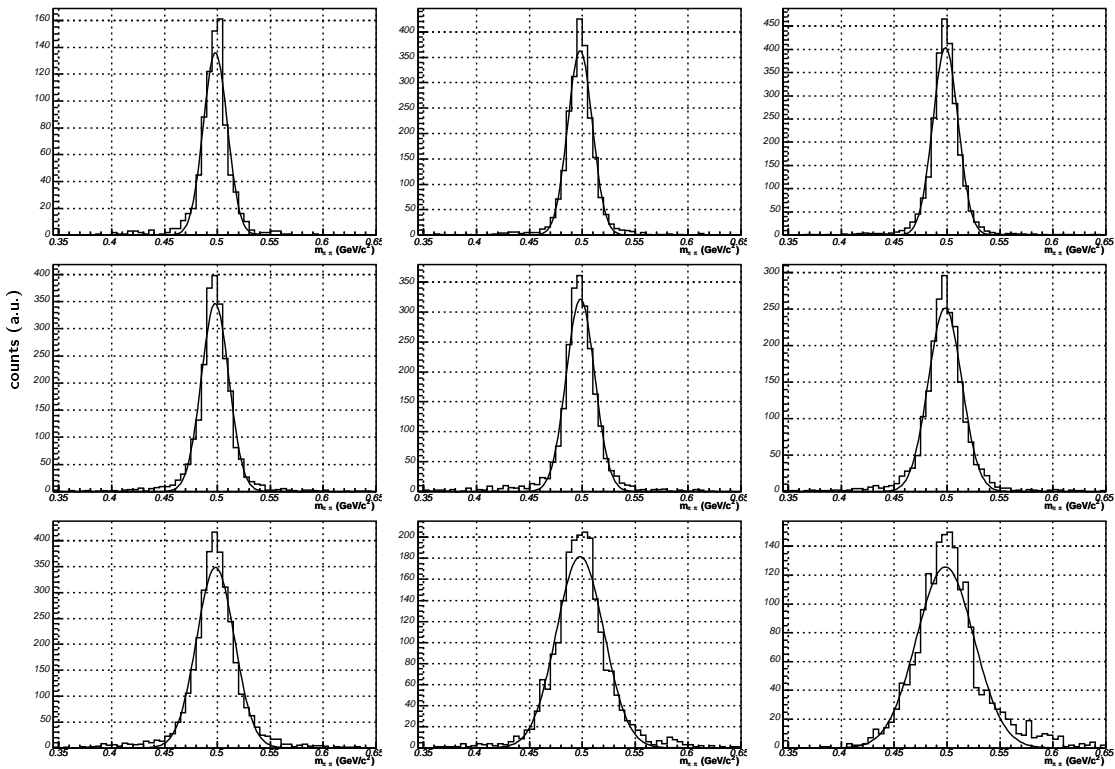


Figure 5.10: Invariant mass spectra for rapidity bin $y \in (2.15 - 2.30)$. Consecutive panels show transverse momentum bins.

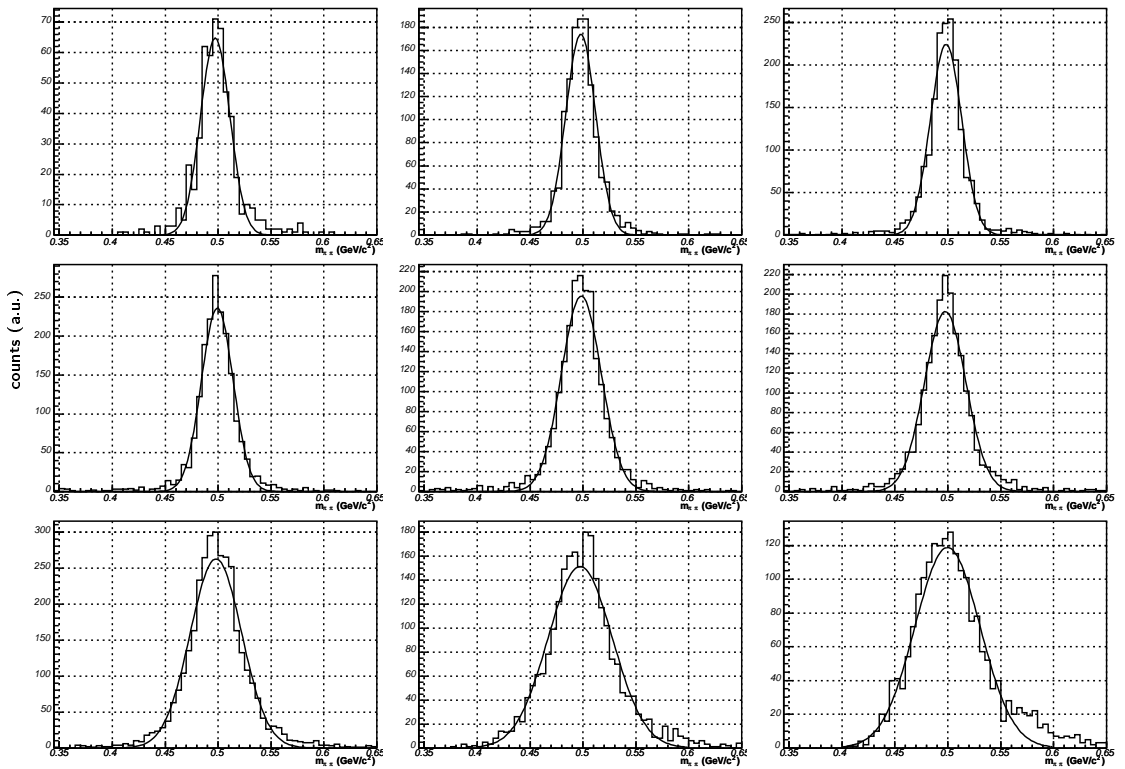


Figure 5.11: Invariant mass spectra for rapidity bin $y \in (2.30 - 2.45)$. Consecutive panels show transverse momentum bins.

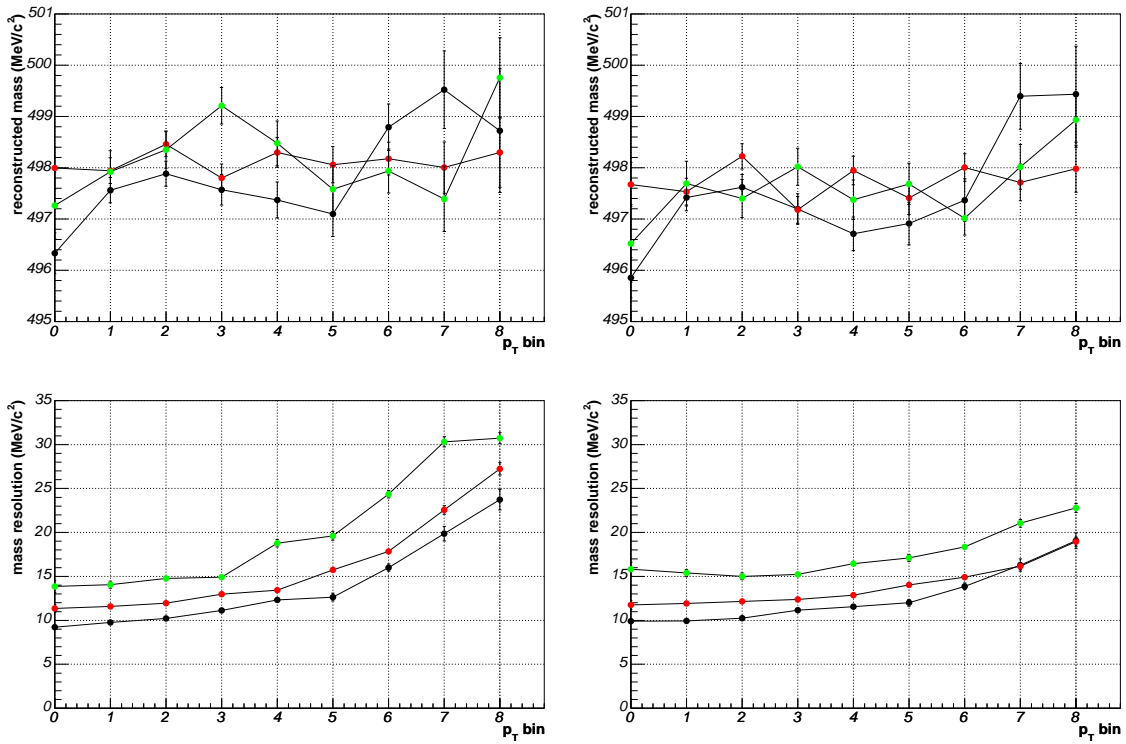


Figure 5.12: Parameters of the Gaussian fit to invariant mass spectra. Top: reconstructed mass using combined momentum (left) and $pcor3$ (right). Bottom: peak resolution using combined momentum (left) and $pcor3$ (right)

The peaks does not follow the Gaussian shape. For the low momentum, with narrow peaks the tails on the left side develop. For the high momentum peaks the sizable tails on the high invariant mass are present. The reasons for the tails are manifold:

- multiple scattering for low momentum tracks
- usage of *pcomb* for late decays, pronounced mostly for high $\beta\gamma K_S^0$

For the middle momentum tracks the shape is not completely Gaussian, but the differences are less pronounced and the non-Gaussian part is concentrated in the peak.

Two methods are used to extract the peak. The first method is to fit a Gaussian and use the area under the curve as a yield. In this case the peak extraction efficiency will be the ratio of the area under the curve and the total number of entries. If the peak will be Gaussian the efficiency would be $\eta = 100\%$. The second method consist on counting the number of entries in a given area, for example $\pm 2\sigma$ around the center, the width taken from the fit. In this case the efficiency is the number of counted entries divided by the total number of entries. If the peak would be fully Gaussian the second method shall have the efficiency of $\eta = 95\%$.

The peak extraction efficiency is shown in Fig. 5.13. The upper row for the first method, lower for the second. The left column for the combined momentum and the right for *pcor3*. When the fit is used, for most of the points the efficiency is at the level of 92 – 94%. At the edges, for high transverse momenta, it behaves differently for both scenarios: in case of *pcomb* it drops to 80% and stays relatively constant when *pcor3* is used. When simple counting is employed, the efficiency is accidentally similar to the case of fitting and is below the value of $\eta = 95\%$.

The four methods can be used for the data analysis and the differences between results will give and insight into systematic errors. The numbers presented depend on details of the simulation and to justify their use the resolutions obtained with data have to follow the resolutions obtained with the simulation.

For the final analysis of data the tree parameter fit will be used and not combined momentum. This decision is based on two results from the Monte-Carlo. The first is better peak resolution of the tree-parameter fit at high momentum and the second is a flat correction due to peak extraction efficiency.

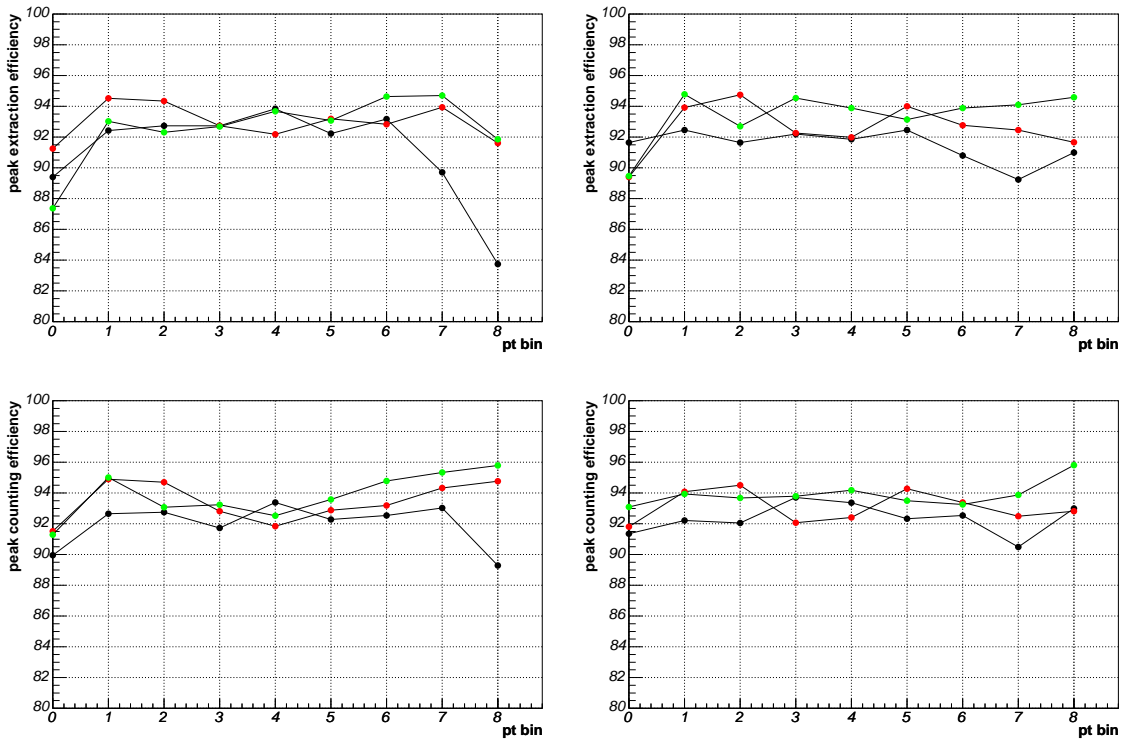


Figure 5.13: Peak extraction efficiency for two methods and two types of momentum. Top: integral of the Gaussian fit for combined momentum (left) and *pcor3* (right). Bottom: counting the entries using combined momentum (left) and *pcor3* (right)

6 Final data analysis and results

After data processing, the invariant mass spectra were obtained. A few more steps have to be performed to obtain the final results. The first step is the extraction of the peak from the invariant mass spectrum, with the help of the background estimated with mixed events. Here it is important to note that with the signal-to-background as small as in this case not only the shape but also the normalization are crucial. The raw yields extracted from the spectra will be then combined with the reconstruction efficiency to obtain transverse momentum spectra and finally, after integration, the rapidity spectrum.

The assessment of the quality of data and the estimation of the systematic errors are necessary steps before comparing data to other measurements and to theoretical predictions.

6.1 Peak extraction procedure

The invariant mass spectra of same and mixed events were analyzed to extract the peak. Since the signal of the K_S^0 is very weak compared to the combinatorial background the key issue in the peak extraction is a precise normalization of the mixed events. As an additional challenge is securing the stability of the procedure to obtain a handle on the systematic error introduced during peak extraction.

The procedure has a number of steps and starts with scaling mixed events to match the number of entries in same events. The scaling factor has two parts, the first due to mixing with eg. 4 events and the second due to different number of pairs when events with different multiplicity are mixed. The second component varies from bin to bin and is small, at the level of 10^{-4} .

After scaling, the signal spectra are created by subtracting mixed events from same events. Since the mixed events are not exactly reproducing the combinatorial background a set of 50 signal spectra is created by scaling the mixed events spectra by an additional small factor ε :

$$G_\varepsilon(m) = S(m) - (1 + \varepsilon)M(m) \tag{6.1}$$

where $G_\varepsilon(m)$ is the signal spectrum, $S(m)$ is same events spectrum and $M(m)$ is normalized spectrum of mixed events. The small factor ε is changing from -10^3 to $+0.6 * 10^3$. It is worth noting that the mixed events spectrum is multiplied by a number, not by a function. Multiplying mixed events by a function, for example a second-order polynomial, can simplify the procedure. On the other hand it would introduce an additional level of arbitrariness into data analysis.

Every signal spectrum $G_\varepsilon(m)$ is analyzed by fitting a formula representing a Gaussian sitting on a slope:

$$f(m) = A + B * m + C * \frac{1}{\sigma\sqrt{2\pi}} \exp\left(-\frac{(m - m_0)^2}{2\sigma^2}\right) \quad (6.2)$$

where m is the invariant mass and the fit parameters: A , B , C , m_0 and σ represent respectively: A – the offset of the background, B – the slope of the background, C – the integral under the Gaussian, m_0 – the reconstructed mass of the K_S^0 and σ is the width of the Gaussian peak. The range of fitting is chosen arbitrarily to be $0.37 < m < 0.8$ GeV. The variation of the upper limit does not influence the fit stability, while the variation of the lower limit has an impact on the results obtained at the level of 3% of the extracted yield.

The spectrum with the best fit is selected. The selection is based on the smallest value of the reduced χ^2 of the fit. Other methods were also tried, based on the smallest value of fit parameter B , the slope. The second method gives essentially the same results. For the control over the systematic error the method can introduce, the parameters of the fit – integral under the Gaussian and the width of the Gaussian – are histogrammed for every spectra fit with reduced $\chi^2/NDF < 2$.

The best spectrum is analyzed further. The function $g(m) = A + B * m$ is subtracted from it and the number of entries in the histogram in the range $m \in (m_0 - 2\sigma, m_0 + 2\sigma)$ is counted. The range was selected arbitrarily, but this range contains most of the signal and the fluctuations of the background are not very strong. This estimation of the signal has to be corrected for the range used. Theoretically, the number has to be scaled by $1/erf(2) = 1/0.95$. Due to the experimental effects, eg. multiple scattering, the peak is not fully Gaussian in particular at the tails. Thus the correction factor is estimated using full Monte-Carlo simulation. The correction factor for tails is presented in Fig. 5.13.

After this procedure there are three estimates of the raw yield: integral under the best fit, counted entries after subtracting the slope and integral from a set of good fits. The statistical error of the third estimation is the standard deviation of the obtained values.

The statistical error of the yield is calculated using total number of entries in the given range of the histogram. Strictly speaking the error Σ equals:

$$\Sigma = \sqrt{\sigma(S) + \sigma(B)} \quad (6.3)$$

where the $\sigma(S)$ is the statistical error of the signal and background and $\sigma(B)$ is the error of the background. In this case the fluctuations of the signal are negligible and the background has to be counted twice (in same and in mixed events) thus the statistical error is:

$$\Sigma = \sqrt{2} * \left[\int_{M-a}^{M+a} dm S(m) \right]^{1/2} \quad (6.4)$$

where the integration is performed in some arbitrary range. The range is usually chosen to span 4 units of standard deviation – the same range as used to estimate the yield by counting the entries. The estimated error scales like $\sim \sqrt{a}$, thus changes of range will not give much difference in the estimation of the error.

Another possibility to estimate the error is to take the value from the fitting program. This value shall contain some information on non-Gaussian shape of the signal, but in practice both values of error agree.

After extracting the peak for every bin in (p_T, y) in a given rapidity range the same procedure can be applied to the total signal in the rapidity bin – to assess the stability of the procedure.

6.2 Results – transverse momentum spectrum

6.2.1 The raw signal

In the chapter discussing Monte-Carlo simulations the rapidity space was divided into 5 bins starting from $y = 1.85$. Since no signal was observed in the first bin, in this chapter the rapidity bins, numbered from (1) to (4) cover the range $y \in (2.0 - 2.45)$. The bins have the width of 0.15, the same as in Monte-Carlo simulations.

The signal with the best fit for every rapidity bin is shown in Fig. 6.1. The number of entries and its error is shown on the picture. The signal looks properly extracted. The procedure in fact was not expected to work properly on the data from the whole rapidity bin. The fit expects a Gaussian, and this assumption is true when analyzing a particular transverse momentum – rapidity bin. When analyzing the whole rapidity bin, the signal is a set of many Gaussians with different widths.

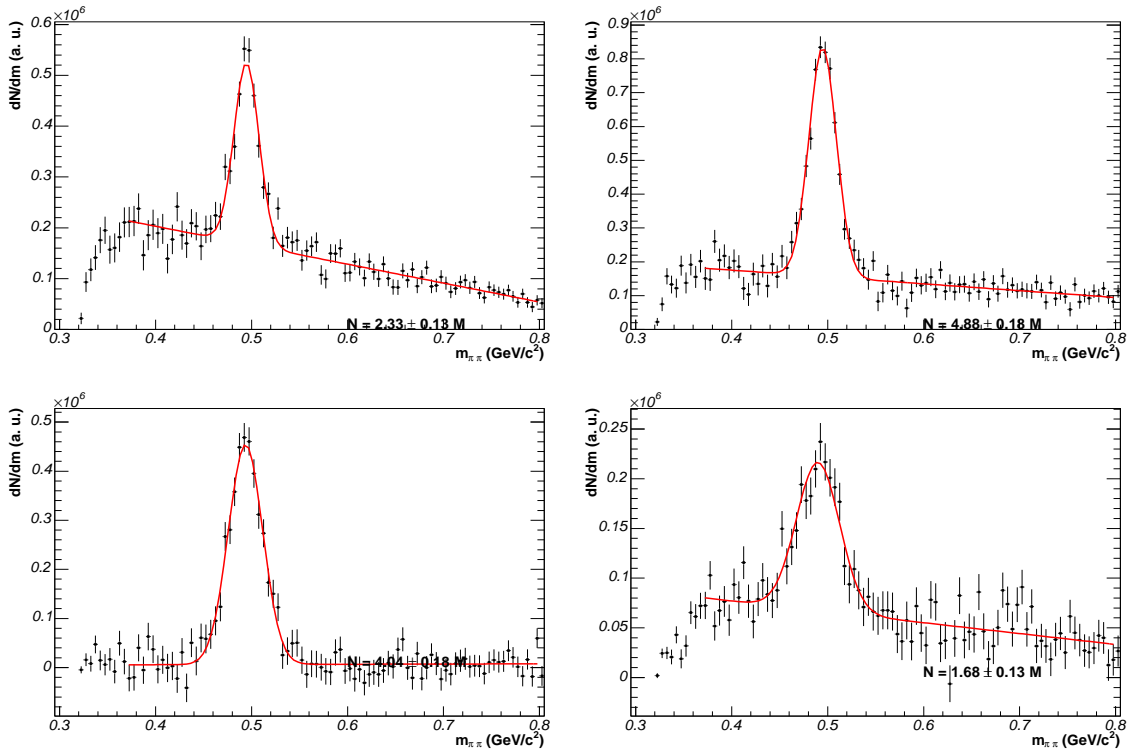


Figure 6.1: Signal spectrum for four rapidity bins with the fit. The number on the figure shows the raw yield.

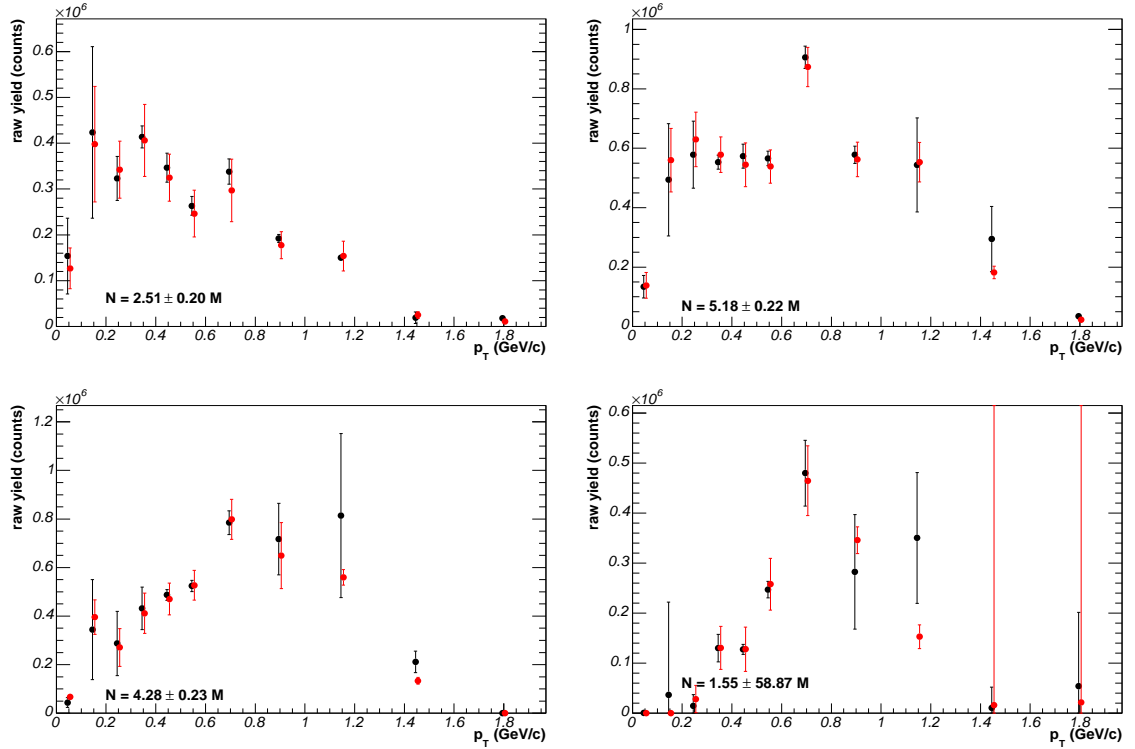


Figure 6.2: Extracted raw yield for four rapidity bins. The red points show the signal extracted from the best spectrum, the black points shows the mean value from the normalization scan.

The signal spectra for every (p_T, y) bin using best fit and counting method are collected in Appendix A.

6.2.2 The raw yield

The raw yield for every transverse momentum bin is shown in Fig. 6.2. The red points show the signal from the best fit while the black points shows the mean value from the normalization scan.

Note that the raw yield is not corrected for the acceptance or the width of the transverse momentum bin. The signal is relatively constant due to increasing bin size with transverse momentum. The highest signal is usually in the bin $0.6 - 0.8 \text{ GeV}/c$ – the first bin with the width 0.2 of GeV/c .

Both estimations of the yield agree very well. The discrepancies are well below statistical error. The statistical errors of the red points represent the real fluctuation of the signal. The error of the black points represents the stability with respect to the variation of the

background normalization and the spectra thus obtained are not statistically independent, so the black errors are often smaller than the red errors. This fact also means that the systematic error introduced by the normalization of the background is below statistical errors.

The total signal and its error is also displayed and both numbers can be directly compared with the numbers from Fig. 6.1. The comparison between the raw signal taken from whole rapidity bins and the sum of signals taken from every (p_T, y) bin is shown in Fig. 6.3. The left panel shows the raw yield in rapidity bins using two methods. Black points show the yield extracted from the total rapidity bin and the red points show the yield extracted bin by bin.

The points are analyzed statistically and the reduced variable is created:

$$\Delta Y = \left(\frac{(Y_T - Y_B)^2}{\sigma_T^2 + \sigma_B^2} \right)^{1/2} \quad (6.5)$$

where Y_T is the yield extracted from the whole rapidity range and the Y_B is the yield extracted bin-by-bin, and their errors are σ_T and σ_B respectively. The variable created should follow Gaussian distribution if the data are statistically independent. The results of the statistical analysis are shown in the right panel of Fig. 6.3. The data are fully compatible and the residuals are below the values expected from the statistical distributions.

While looking carefully at the raw yields from different method, one can observe that the black points are systematically lower than the red points. This suggest that extracting the yield from the whole bin leads to a lose of yield. The lost yield is smaller than statistical error and can be explained by the fact that the signal is not Gaussian in this case.

6.2.3 Fit parameters

The goal of this analysis is the reconstruction of the number of kaons. The other parameters of the fit: reconstructed mass and the width of the Gaussian are important to assess the data quality.

The parameters of the fit – reconstructed mass and the width of the Gaussian – are shown in Fig. 6.4. The fit parameters from data are depicted in black and overlaid with the Monte-Carlo values, depicted in blue. The straight blue line shows the PDG value of K_S^0 mass equal $m = 497 \text{ MeV}/c^2$.

The reconstructed mass is systematically lower than the value expected from the Monte-Carlo studies. The systematic shift is comparable with the statistical error of the reconstruction and smaller than bin-size of the invariant mass spectrum equal to $5 \text{ MeV}/c^2$.

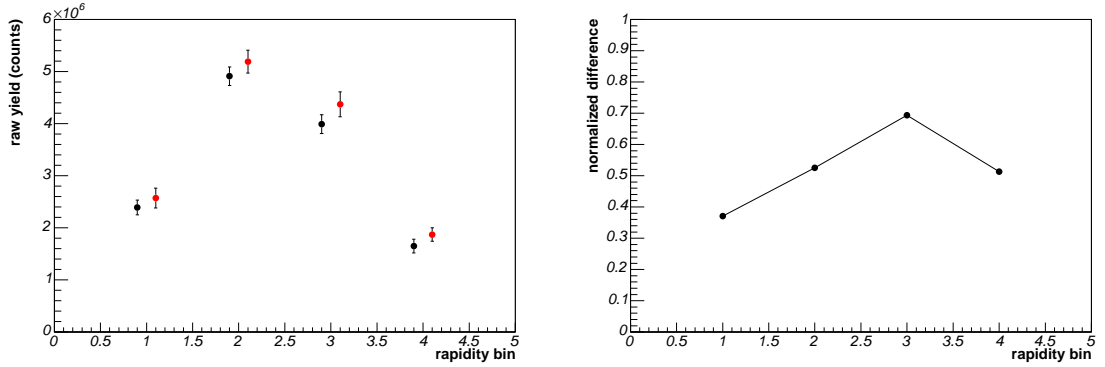


Figure 6.3: Crosscheck of the raw yield extraction for all rapidity bins. Left panel: black – total signal in a rapidity bin, red – sum of signal in (p_T, y) bins. Right panel: difference between two methods normalized to statistical fluctuations.

The reconstructed resolution agrees very well with values expected from Monte-Carlo studies. The peak widths from data fluctuate around Monte-Carlo values at the level of statistical error. Some tendency to higher widths can be observed, but they are not statistically significant. This agreement justifies both using the peak extraction algorithm described and the validity of the Monte-Carlo program.

Experimentation with the normalization factor shows that overestimating the background lead to a narrower peak and underestimation of the background to a broader peak.

6.2.4 Transverse momentum spectra

The first physics result are the transverse momentum spectra shown in the left column of Fig. 6.5.

The transverse momentum spectra $dN^2/(dp_T dy)$ were obtained by correcting the raw yields by the efficiencies calculated using Monte-Carlo studies and described in Chapter 5. The spectra were fit by the Boltzmann distribution; the details of the fitting procedure will be described below. The values displayed in the panels are:

1. rapidity range
2. the yield dN/dy obtained by summation of the measured signal, the errors of individual points added in squares.
3. the yield dN/dy obtained from the fit, the error is the statistical error of the fit.
4. the temperature T with the statistical error.

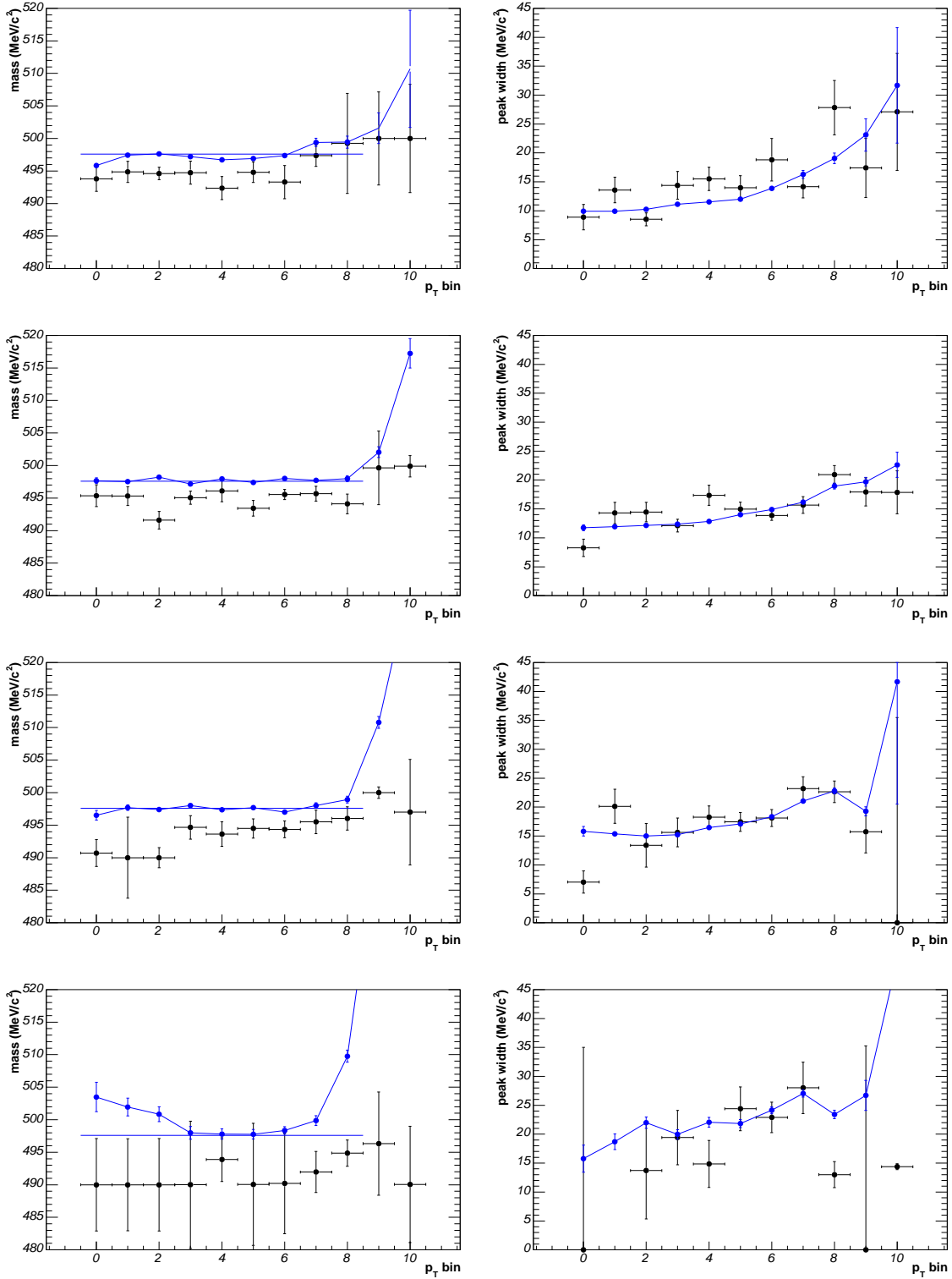


Figure 6.4: Fit parameters: reconstructed mass and the mass resolution for four rapidity bins. Data are drawn as black points and Monte-Carlo as blue.

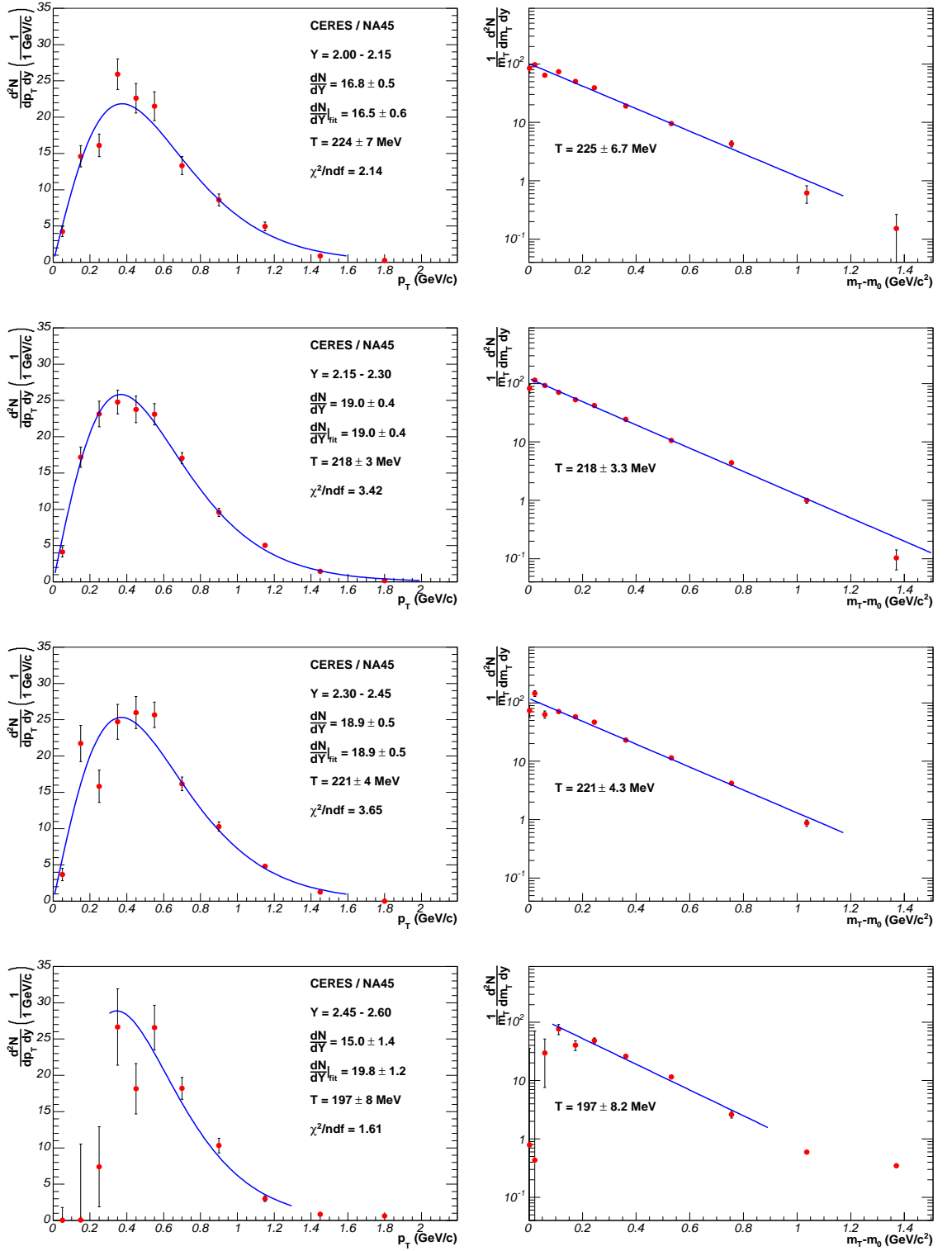


Figure 6.5: Transverse momentum and transverse mass spectrum for four rapidity bins.

6.2.4.1 Transverse momentum fit representation

The transverse momentum spectrum was fit with the Boltzmann function. The commonly used form

$$\frac{d^2 N}{dy dp_T} = A p_T \exp\left(-\frac{\sqrt{m^2 + p_T^2}}{T}\right) \quad (6.6)$$

with two parameters of the fit: scale A and temperature T is not the best choice to fit data. In this representation the total yield – integral of the function – depends on both parameters of the fit and thus the error of the yield is correlated with the error of the scale and temperature. A different representation of the function can be found with two uncorrelated parameters: total yield and temperature. This can be achieved by substituting parameter A by two parts: the total yield N and the temperature dependent normalization factor $1/C(T)$. The normalization factor $1/C(T)$ can be found by integration:

$$C(T) = \int_0^{p_T^{max}} p_T \exp(-m_T/T) dp_T \quad (6.7)$$

The integration yields the formula:

$$\frac{d^2 N}{dy dp_T} = N * \frac{p_T \exp(-m_T/T)}{[T(m_0 + T) \exp(-m_0/T) - T(m_T^{MAX} + T) \exp(-m_T^{MAX}/T)]} \quad (6.8)$$

where both parameters of interest: N – the total yield – and T – the temperature – are direct parameters of the fit. This form has an arbitrary number m_T^{MAX} , but when this number runs to infinity the factor:

$$\lim_{m_T^{MAX} \rightarrow \infty} T(m_T^{MAX} + T) \exp(-m_T^{MAX}/T) \rightarrow 0 \quad (6.9)$$

runs to 0, and this part can be neglected. This results in the equation:

$$\frac{d^2 N}{dy dp_T} = N * \frac{p_T \exp(-m_T/T)}{T(m_0 + T) \exp(-m_0/T)}. \quad (6.10)$$

which was actually used for fitting.

6.2.4.2 Discussion on the shape of the spectrum

The data points in Fig. 6.5 follow the fit very well. In particular for the bin (2) the points are aligned on the fit line. For side bins there are deviations which are connected with the rapid changes of the decay topologies: from back-to-back to the topology with two tracks at the same side. The change of the topology means that at least one track is at the border of the geometrical acceptance of the detector. The deviations are comparable to the statistical fluctuations.

The values of the χ^2/NDF are at the level of $\chi^2/NDF \sim 3$, higher than expected for the statistical distributions. The relatively large values of χ^2/NDF can be explained by one of two points with underestimated error. The structure of the relation between data points and the fit will be studied further.

The important aspect of the transverse momentum spectrum is the fact that the total yield in the rapidity range can be calculated by two methods: from the fit and by directly counting the points. The second method is free from the uncertainties due to the extrapolation.

Since two methods use the same points the results of both estimations agree below the statistical error.

6.2.5 The transverse mass spectra

The transverse mass spectra are shown in the left column of Fig. 6.5. The points are recalculated from the transverse momentum and drawn in the logarithmic scale. Both spectra – transverse momentum and transverse mass – are mathematically equivalent. However different properties of the spectra are visible when displaying both quantities. On the plot with transverse momentum spectra, the points with the highest yield are most visible, and the points with low yield, at high transverse momentum are practically invisible. On the other hand, in the plot of the transverse mass spectra the alignment of the points, the temperature, is the most visible. Both methods of presentation provide complementary insight into the quality of the data. The presented transverse mass is fit with the exponent

$$\frac{1}{m_T} \frac{d^2 N}{dm_T dy} = A * \exp\left(-\frac{m_T}{T}\right) \quad (6.11)$$

with two fit parameters: scale A and the temperature T . The temperature obtained is shown in the panel. The transverse mass spectra and its fits are not used for further analysis, they are used to check the quality of the data.

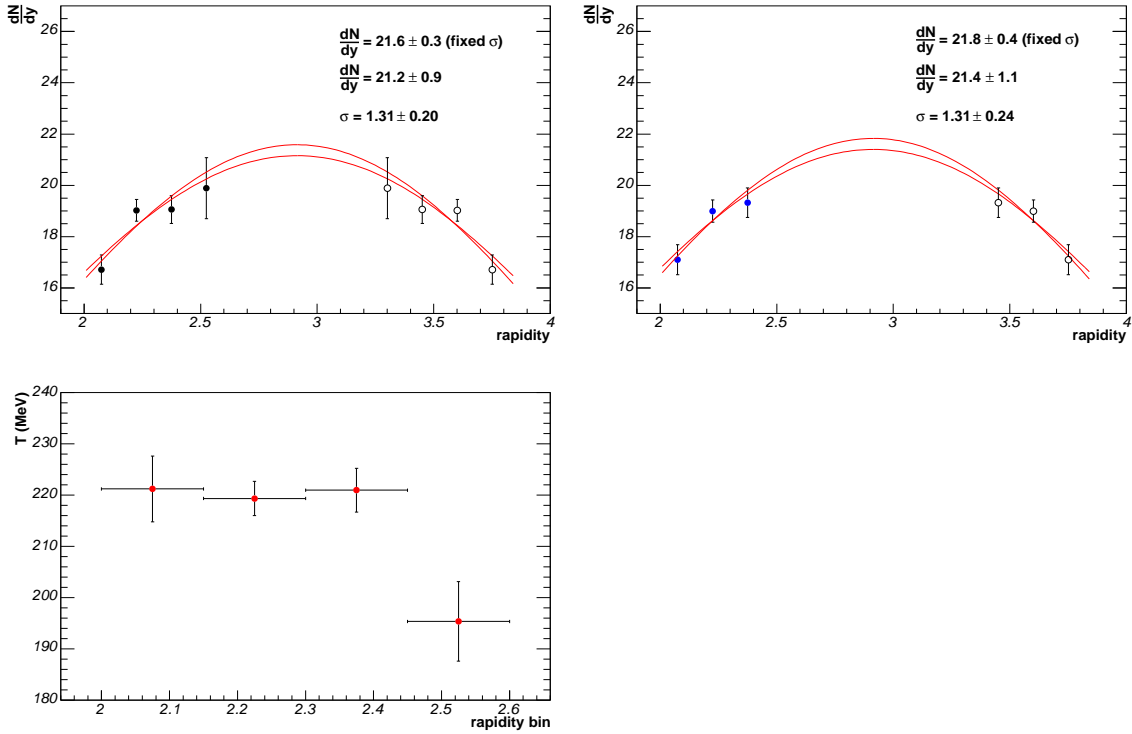


Figure 6.6: Summary: the yield dN/dy obtained from the fit and by integration of the points. Temperature in the rapidity bins.

6.3 Rapidity spectrum

The parameters of transverse mass spectra can be analyzed further. The measured temperatures in the rapidity bins are displayed in the bottom panel of Fig. 6.6. The precision achieved is at the level of 5 MeV, which corresponds to around 3%. The first three points lie on a flat line at $T = 220$ MeV only the last point does not follow the systematics. The value measured for the last point has to be treated with caution because of a large statistical error due to the severely limited acceptance.

The yields are shown in the upper row of Fig. 6.6. The left panel shows the yields obtained from the fit while the right panel shows the integration of individual points. Due to the acceptance, the summation is limited to the first three bins in the rapidity. The points are reflected at midrapidity and the reflected points are displayed as open symbols. Both yields were fit by a Gaussian and the parameters of the fit are displayed on the panels. The center of the Gaussian is set to midrapidity equal to $y_0 = 2.973$. Fitting a two-parameter function to three or four points is problematic, because the χ^2/NDF distribution with the number of degrees of freedom below 3 does not peak at $\chi^2/NDF \simeq 1$, but is broad [43].

However, the two fits give similar result. The width $\sigma = 1.31 \pm 0.20$ and the extrapolated yield at midrapidity $dN/dy|_{y=0} = 21.2 \pm 0.9$.

6.4 Data quality

The statistical error of the measurement is at the level of 5%. An analysis of the quality of data has to be performed in order to establish systematic error. The quality of data was checked in two different ways. In the first method, the fitting procedure was analyzed in detail, by fitting a part of the spectrum and by the study of the relative errors with respect to the fit. This method gives an insight into the structure of the data and its relation to the fit.

The second method is based on the coherent variation of the cuts in data and simulation. Two data sets will be presented: one with different opening angle cuts and the second with different cuts on the minimum transverse momentum of the tracks. Additional data sets were obtained and analyzed, but the results will not be detailed here.

Additional checks were performed, for example dividing the data into two subsets with different orientation of decay (positive track forward or backward). This method gives an insight into the peak extraction procedure. Both data samples have the same signal but the background is different due to proton contamination (see Fig. 4.23). The details of this analysis will not be presented here only the final results will be quoted.

6.4.1 Stability of the Boltzmann fit

The stability of the Boltzmann fit to the transverse momentum spectrum was checked by fitting a subset of data. Five consecutive points are fit by Boltzmann function, the starting point ranging from (0) to (6). The graphs with the fit parameters, the yield and the temperature, as a function of the starting point of the fit are shown in Fig. 6.7. Since the fits share data points they are not statistically independent, however the fit starting at (5) do not share points with the first fit, starting at (0), thus the two are independent measurements of the yield and the temperature.

The Boltzmann fit has a fixed value at $p_T = 0$ and the rise at $p_T \simeq 0$ is dominated by the phase-space factor not by the temperature. This feature makes the fit starting at high transverse momentum stable but the fit starting at $p_T = 0$ is not sensitive to the temperature. This is visible in the first points of the temperature scan.

The data shows high quality and the variation of the reconstructed parameters are at the level of the statistical errors. The rapidity bin (3) and (4) are not very stable for

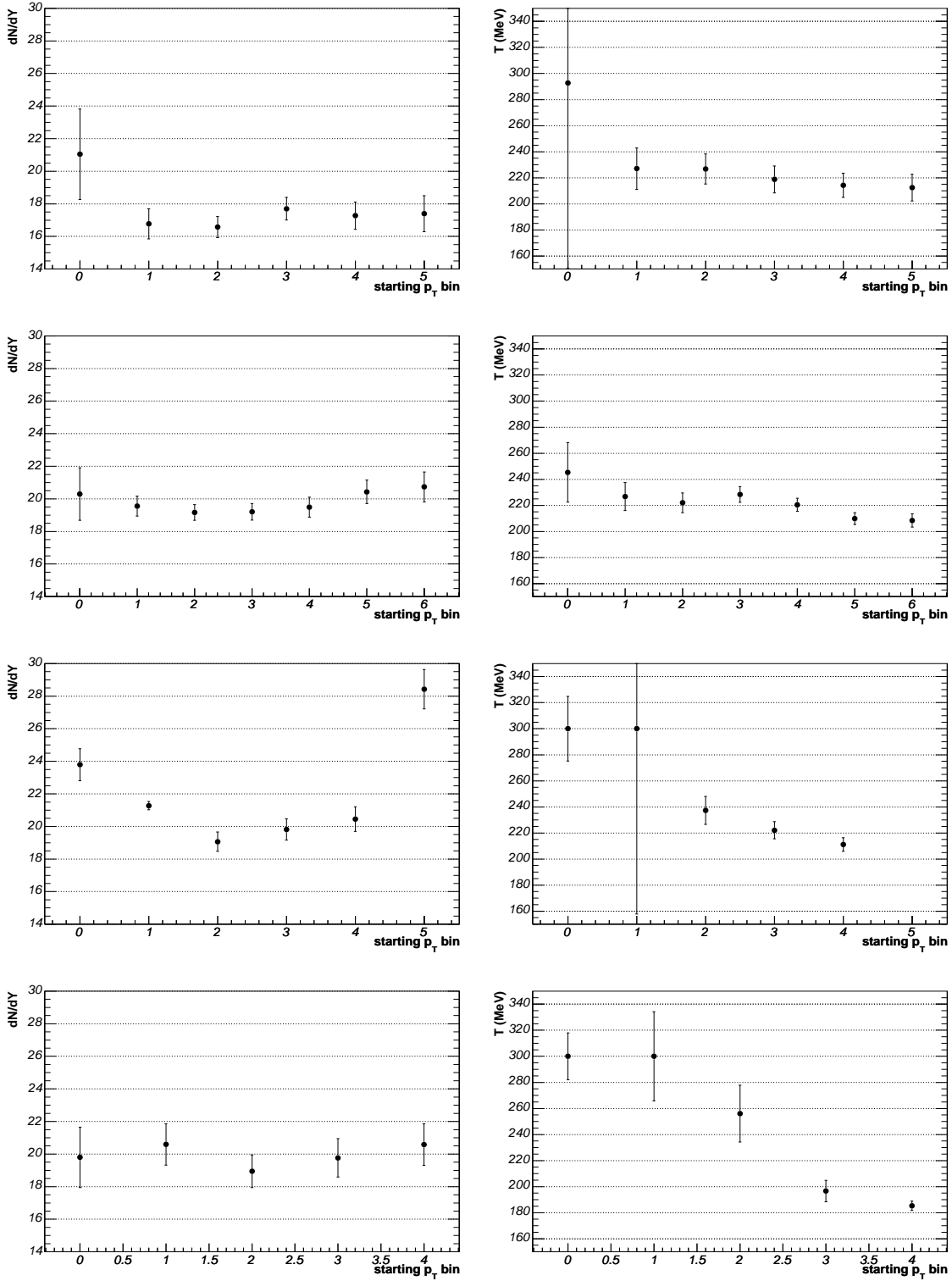


Figure 6.7: Stability of the Boltzmann fit. Left column: reconstructed yield as a function of the starting bin. Right column: reconstructed temperature. The rows are for rapidity bins. See text for details of fitting procedure.

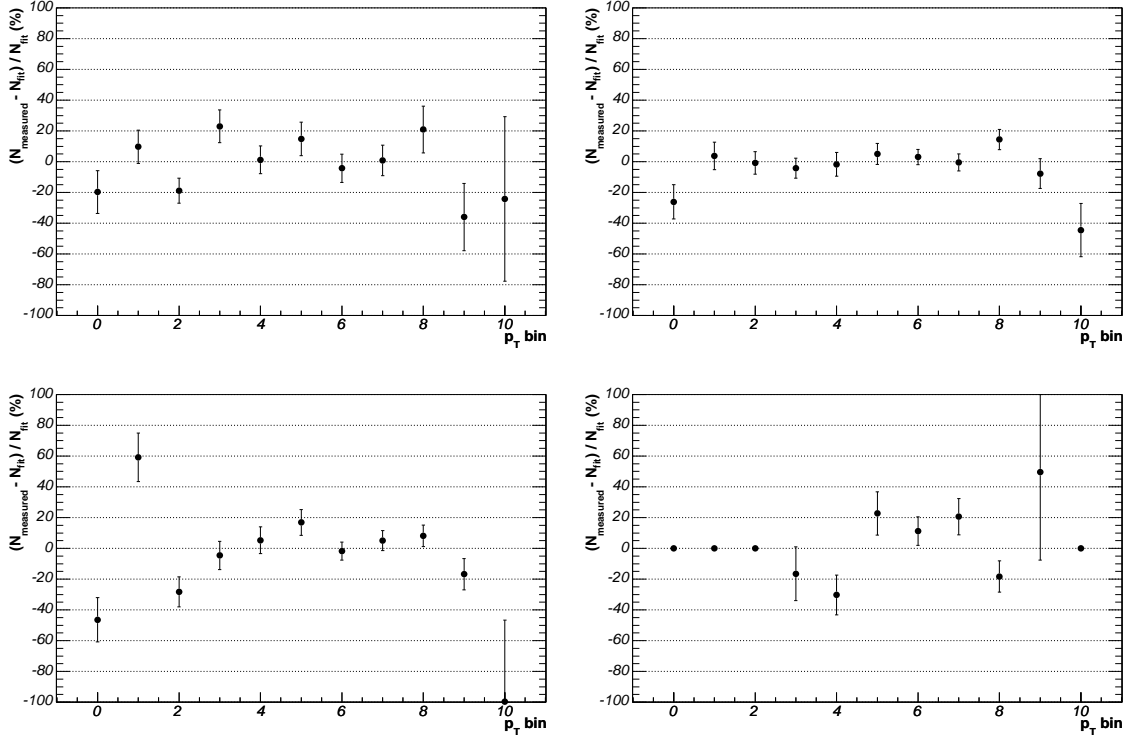


Figure 6.8: Residuals of data points with respect to the fit for four rapidity bins. See text.

the reconstruction of the temperature, but the yield is stable. The bin (2) which has the cleanest acceptance offers the best quality in terms of the fit stability test.

6.4.2 Alignment of the points on the fit

The alignment of the points on the fit was studied by plotting the variable:

$$\delta(p_T) = \frac{N_{meas}(p_T) - N_{fit}(p_T)}{N_{fit}(p_T)} \quad (6.12)$$

where $N_{meas}(p_T)$ is the measured point at a given transverse momentum and the $N_{fit}(p_T)$ is the fit value for this momentum. In short $\delta(p_T)$ shows the difference between data and fit normalized to the fit value.

The results obtained are shown in Fig. 6.8. When only statistical errors are present 68% of the points shall cross the line $\delta(p_T) = 0$ with their error bars. In the plots shown, no structure develops, suggesting that the data follow random distribution. The only visible correlation is that the first point tends to be underestimated by $\delta(p_T) \simeq 20\%$. This can be correlated with the fact that the resolution of the peaks for these points is narrower than

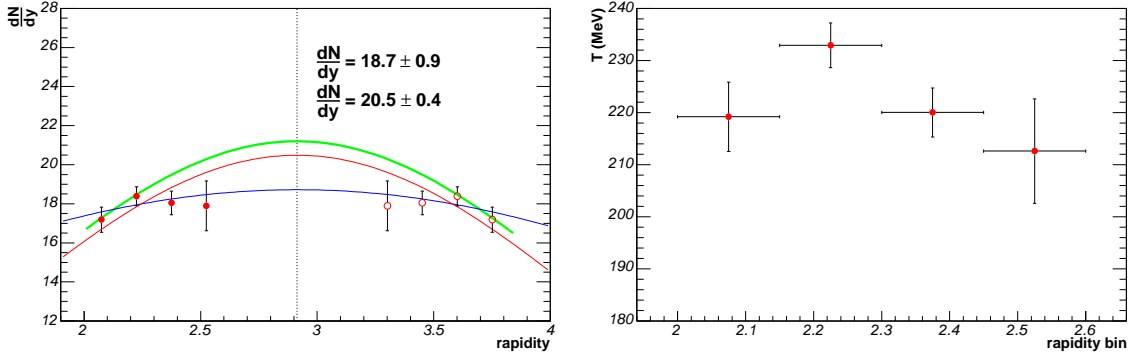


Figure 6.9: Results with different mixing strategy and cuts on the opening angle. Left: rapidity spectrum, green line: the reference data, red line: fit with constrained width, blue line: two-parameter fit. Right: reconstructed temperature in rapidity bins

expected. This correlation is visible when analyzing a set of spectra, for a single spectrum this can be explained by the statistical fluctuations.

6.4.3 Results using different cuts

The best method for the analysis of the systematical error is to process data and Monte-Carlo simulations with a different set of cuts. The difference in the final results are then used as the estimation of the systematic error. The cuts in the main analysis are chosen to obtain the best signal, so a small deterioration of the quality of data is also expected.

In addition to the reference data set presented before two additional data sets will be presented. The first set has the opening angle cut changed. In the standard analysis the opening angle cut was chosen to be $\psi > 0.1$ rad. This cut removes the small range correlation and provides a good shape of the invariant mass spectrum. The drawback of this cut is the fact that it removes a substantial part of the high transverse momentum kaons. The variable opening angle cut was applied. The cut was adjusted to the expected opening of the decay product for every momentum of the kaons obtained in the simulations. This data set produced a longer spectrum but the low transverse momentum part is distorted. The spectrum with the highest penalty due to the opening angle cut of $\psi > 0.1$ rad is the last spectrum, with the new data set this spectrum will gain an additional 2 points.

The results of this data set are shown in Fig. 6.9. This set has a different spectrum in the temperature space. The spectrum in the rapidity bin (2) has temperature of $T = 235 \pm 7$ MeV and the last spectrum, which gain most on the cut, has a temperature $T = 212 \pm 10$

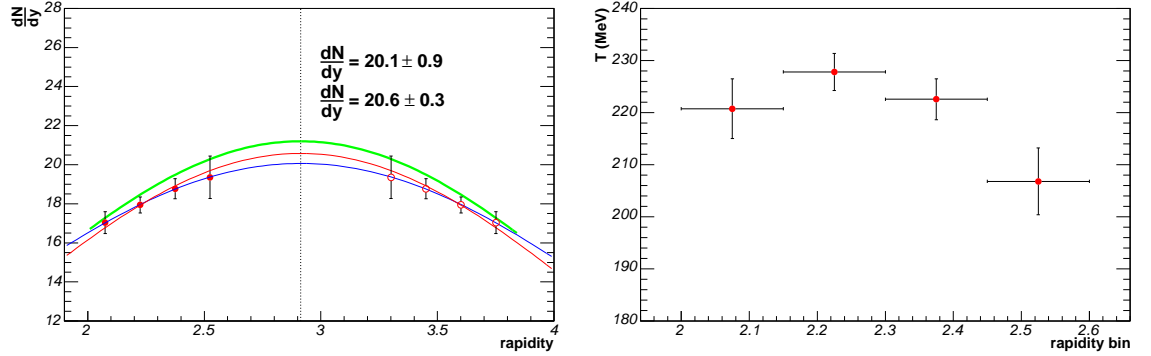


Figure 6.10: Results obtained with the transverse momentum cut of $p_T > 0.15$ GeV/ c . Left: rapidity spectrum, green line: the reference data, red line: fit with constrained width, blue line: two-parameter fit. Right: reconstructed temperature in rapidity bins

MeV and is now inside the systematics established by the other points. From this diagram a conclusion can be drawn with regard to the systematic error of the temperature, which is at the level of $\delta T = 10$ MeV.

The yield obtained in this data set has a different shape than that seen in the reference data. The data set was fit twice with two Gaussians: the first with two parameters (the yield at midrapidity and the width) and the second with one parameter, the yield and the width is fixed to the value obtained in the reference data set. The difference between the yield at midrapidity in this data set and the reference set is $\delta Y \simeq 1$.

The second data set was obtained by changing of the lower cut on the transverse momentum of the tracks from $p_T > 100$ MeV/ c to $p_T > 150$ MeV/ c . However, his cut reduced significantly the signal in the low transverse momentum part, with the topology of two pions going back-to-back.

The results of this data set are shown in Fig. 6.10. In the case of this data set the shape of the yield in the rapidity space is the same as for the reference set – thus the fit with two and one parameters give essentially the same value at midrapidity.

The maximum temperature difference to the reference implementation is $\delta T \simeq 10$ MeV.

6.5 Systematic error and the final result

From the checks reported above the systematic error of temperature can be set to $\delta T = 10$ MeV. This value is greater than the statistical error of the individual points.

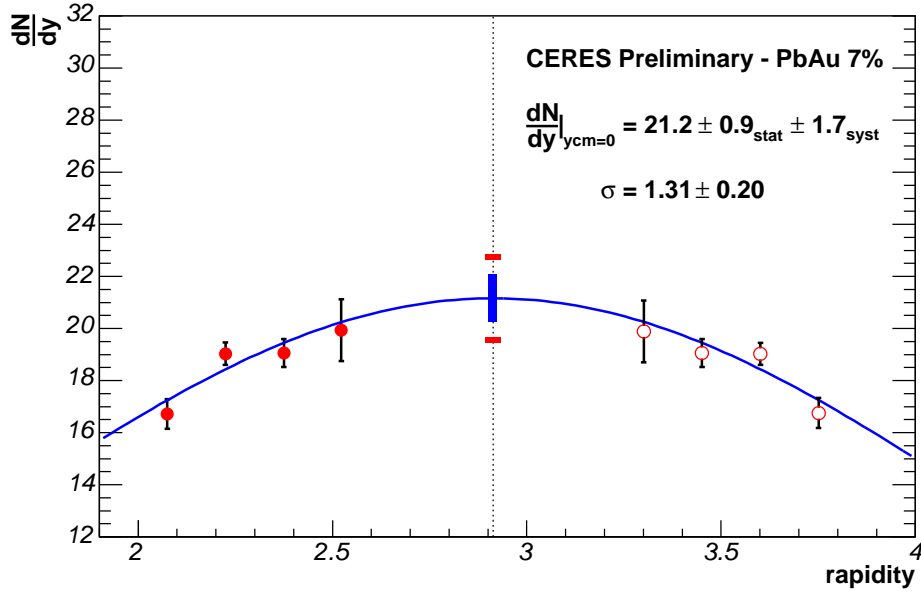


Figure 6.11: Final result. Closed point: measured values with statistical errors, open points: reflection at midrapidity, statistical error of the fit is marked by a blue box and the systematic error by red lines.

The systematic error of the yield is estimated to be 5%, for all points. This error is expected to move all points coherently (not point by point). Additional checks done by dividing the data into subsets yielded the result for the systematic error due to peak extraction procedure to be 3%.

Taking the conservative approach namely that, the two errors are independent and add linearly gives a total error of 8%. In absolute numbers the total error of the yield at midrapidity is $\delta Y = 1.7$.

The final result of this analysis is shown in Fig. 6.11, as presented at the Strange Quark Matter conference in the talk about the CERES results [44].

7 Discussion

The data presented in the previous chapter can be compared with other experiments at top SPS energy and with theoretical predictions. Three measurements can be used for the comparison. The first is the K_S^0 yield reported by the NA57 experiment [23, 45, 46], the second is the mean value of the charged kaons published by NA49 [48] and the last is the preliminary data on K_S^0 from NA49 [47].

The results of other experiments were obtained with different initial conditions: they are Pb on Pb collisions with 5% centrality for charged kaons from NA49 and neutral kaons from NA57 and 10% centrality for K_S^0 from NA49. Before the qualitative comparison can be made the data have to be scaled to CERES conditions. Results will be scaled to the same number of participants using the Glauber model.

From a theoretical point of view, it is difficult to interpret the yield of the neutral kaons in isolation. Instead, the yield will be compared to the global fit of the thermal model to top SPS data.

7.1 Results

Before comparing the obtained results to other experiments, they will be repeated. The transverse momentum spectra for four rapidity bins are shown in Fig. 7.1. The full spectrum was obtained in the range of $2 < y < 2.45$ and a partial spectrum in the range $2.45 < y < 2.6$. The spectrum was reconstructed up to a transverse momentum of $p_T < 1.6$ GeV/ c .

The rapidity spectrum and the temperature as a function of the rapidity are shown in Fig. 7.2. The rapidity spectrum follows a Gaussian shape centered at midrapidity. The statistical precision of the extrapolation to midrapidity is at the level of 4% and the systematic error is 8%.

The temperature was obtained independently for each spectrum. For the full spectra in the first three bins, the reconstructed temperature is $T = 220 \pm 4$ MeV and decreases for the short spectrum. The systematic error of the temperature is estimated to be $\delta T = 10$ MeV.

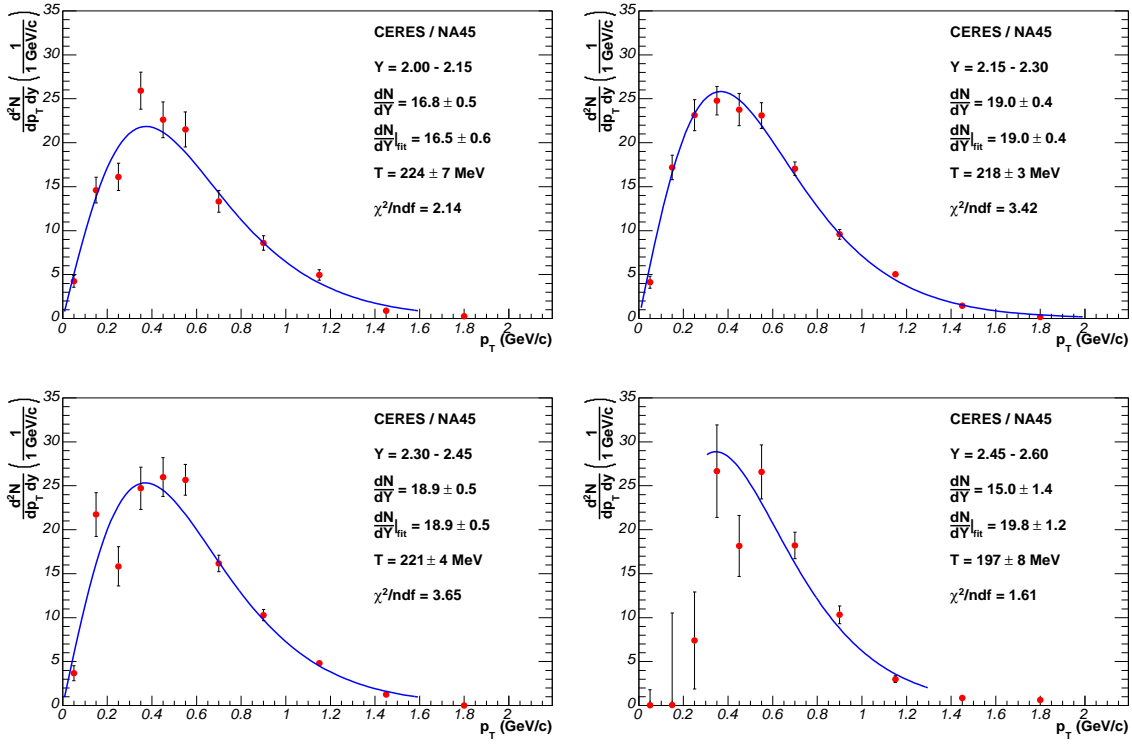


Figure 7.1: Transverse momentum spectra for four rapidity bins.

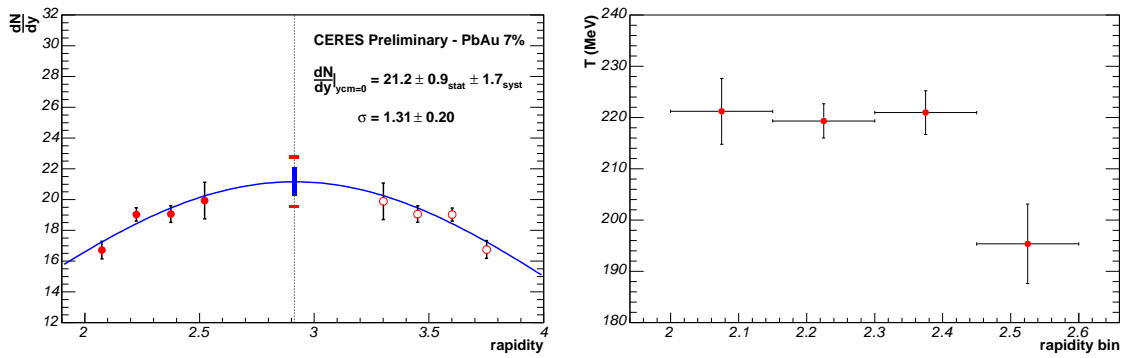


Figure 7.2: Rapidity spectrum (left) and the reconstructed temperature (right)

7.2 The Glauber model

The experimental data show that the particle multiplicities scale with the number of nucleons participating in the reaction. The geometrical picture allowing the calculation of the number of participants and the number of binary collisions in heavy ion reactions was developed by Glauber and also Bialas [50]. The presentation of the method can be found in Ref. [51].

Within the model it is possible to calculate the number of binary collisions and the number of participants as a function of an impact parameter b for given nuclei of target and projectile. The values are obtained by numerically sampling the transverse plane to calculate the number of nucleons in the target n_T and in the projectile n_P in a given transverse plane cell. The number of binary collisions is:

$$n_{NN} = \sigma_{NN} * n_P n_T, \quad (7.1)$$

where $\sigma_{NN} = 30$ mb is the cross section of inelastic nucleon–nucleon collision. If at least one binary collision was recorded for a given nucleon it is counted as a participant. The procedure was implemented in the program [52] used for the calculations presented here.

In the previous paragraph it was assumed that the bulk properties depend on the number of participants. This statement can be verified with the CERES data. The multiplicity density of charged particles at midrapidity measured by CERES is shown on the left panel of Fig. 7.3. The multiplicity density at midrapidity $dN_{ch}/dy|_{y=0}$ was measured in the centrality classes of 5% of the geometrical cross section σ_G . The measurement was performed in the Monte-Carlo independent way, using the silicon tracker. Details of the procedure are presented in Ref. [53].

The mean values of the number of participants were calculated for the centrality classes using the program in Ref. [52]. The multiplicity density divided by the number of participants is shown in the right panel of Fig. 7.3 together with a linear fit. The data points are compatible with the linear dependence and the mean multiplicity is:

$$\frac{dN_{ch}}{dy}|_{y=0} = (1.189 \pm 0.005) \times N_{part}.$$

Using this value, the mean multiplicity density for the analyzed data sample of 0–7% σ_G is:

$$dN_{ch}/dy = 337 * 1.189 = 400.$$

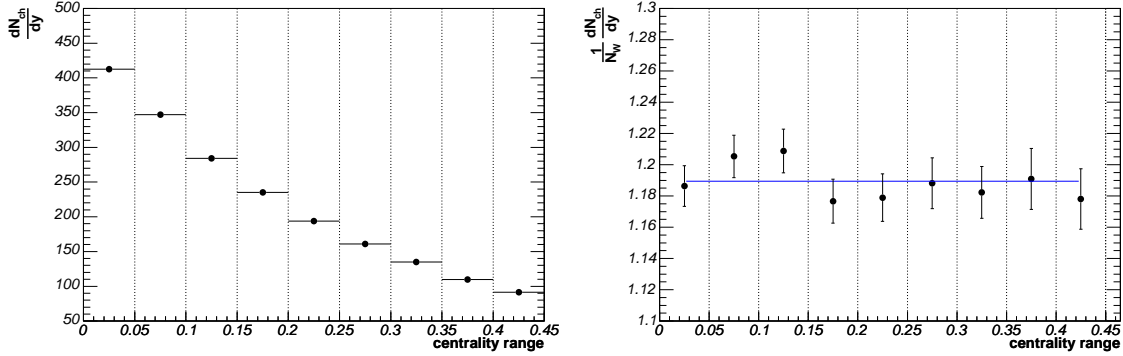


Figure 7.3: Multiplicity density of charged particles dN_{ch}/dy in centrality classes (left panel), multiplicity density per participant (right).

system	centrality	number of participants	scaling factor
PbAu	7%	337.4	
PbPb	5%	357.2	1.059
PbPb	10%	326.6	0.967

Table 7.1: Parameters of the collisions obtained from the Glauber model

This plot also shows that the number of the particles produced scales with the number of participants over a wide range of centralities.

The number of participants was calculated for the centrality used in this work as well as for 5% and 10% centrality of PbPb collisions. The calculation was performed using the program [52] and the results obtained are presented in Table 7.1.

Another possibility of scaling consist of dividing observed yields by the total multiplicity at midrapidity measured by the individual experiments. From Fig. 7.3 and arguments in the previous paragraphs, one can conclude that the number of participants and multiplicity scaling are equivalent. However, the two methods have different systematics.

The actual measurement of the centrality is not “5% most central” but 5% of highest multiplicity, and depending on the calorimeter this can lead to some differences in the actual impact parameter range studied. This bias cancels when dividing a given observable by the multiplicity, but not necessarily when scaling by the number of participants.

On the other hand, the multiplicity of charged particles is not a well defined quantity. In particular the impact of the weak decays can be treated differently in different experiments. All three experiments offer conceptually different methods for the multiplicity measurement. For comparison of different experimental results both methods of scalings will be used and the difference in the multiplicity measurement methods will be discussed.

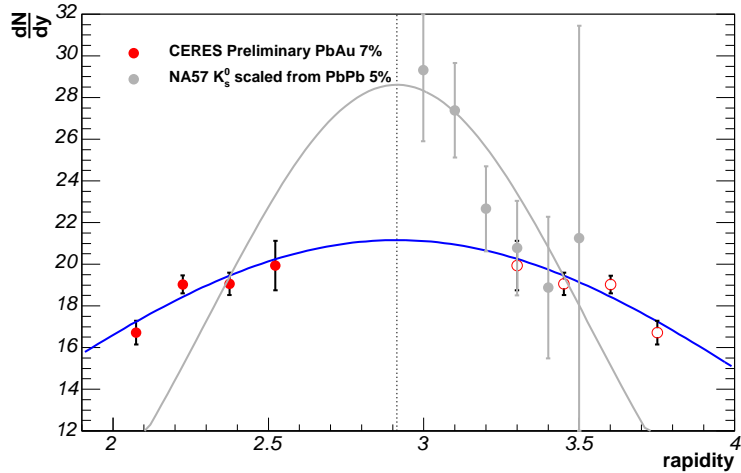


Figure 7.4: Comparison of CERES results with NA57. The former results are depicted with red closed points and reflected at midrapidity (open points) and fit with a Gaussian (blue line). NA57 results are depicted with gray points and fit with a gray line. For clarity no reflection at midrapidity is shown. Data from NA57 are from Ref. [23], scaled to CERES centrality.

7.3 Comparison to other measurements

7.3.1 NA57 – neutral kaons

The rapidity spectrum of the neutral kaon yield was presented for a set of centralities in Ref. [23]. Also the spectra of other strange particles (Λ , $\bar{\Lambda}$, Ξ and Ω) were shown. Here only the most central bin with 5% of the σ_G will be quoted. The result of the comparison is presented in Fig. 7.4.

The interpretation of the plot is manifold. The two fits are in disagreement. The yields at midrapidity differ by about 30% and the widths by a factor of 2. The surprising fact is that the two lines cross in the place where both measurements have a large acceptance. The data have to be considered at on a point by point basis.

In the region where both experiments have large acceptance a remarkable agreement is visible, well below the statistical fluctuations. When comparing NA57 data points with a CERES fit, four out of six points are compatible within statistical errors and two points at midrapidity are outside by about 2 standard deviations. One could assume that the 2 points deviate from the CERES fit because of the statistical fluctuations. This conclusion is not confirmed by the measurements at other centralities. For all 5 measurements, shown in Fig. 7.5, the two points closest to midrapidity are significantly above the other points.

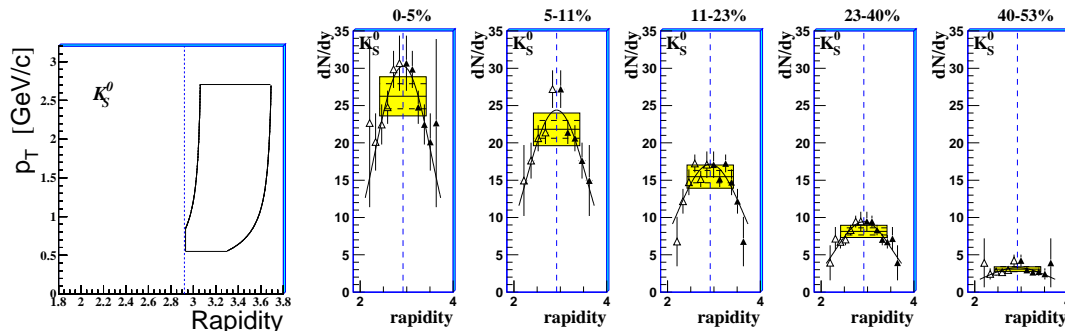


Figure 7.5: Results from NA57. Left panel: acceptance for K_S^0 . Right panel: yield of K_S^0 for 5 centrality classes, note consistent width of all spectra. All plots from Ref. [23] .

It is also interesting to note that the two points at midrapidity have a limited acceptance in the transverse momentum as shown in the left panel of Fig. 7.5.

The data points measured by CERES can not be reconciled with the fit obtained by the NA57 collaboration. Two points are incompatible with the curve by more than 5 standard deviations. One of the points is the one with the cleanest acceptance.

Another interesting feature of the comparison is the fact that the statistical precision of the measurement performed in this work is better than that of NA57 – an experiment designed and optimized for the detection of weakly decaying strange particles. This fact can be explained by the difference in the acceptance. The CERES acceptance starts from $p_T = 0$ GeV/ c , while NA57 acceptance starts at $p_T \simeq 0.6$ GeV/ c , thus the yield is actually not measured but extrapolated. For extrapolation a common temperature estimation is used, which can also explain why data fluctuate less than the statistical error indicates.

The transverse momentum spectrum of the neutral kaon measured by the NA57 experiment was published in Ref. [45]. The temperatures measured by both experiments are in good agreement. The value reported by NA57 is:

$$T = 234 \pm 9_{stat} \pm 24_{syst} \text{ MeV} \quad (7.2)$$

The value obtained in this work:

$$T = 220 \pm 3_{stat} \pm 10_{syst} \text{ MeV} \quad (7.3)$$

is compatible within statistical errors.

The comparison of the K_S^0/N_{ch} ratio gives additional information. For data reported here the value is:

$$K_S^0/N_{ch} = (21.4 \pm 1.1)/400 = (5.35 \pm 0.27)\% \quad (7.4)$$

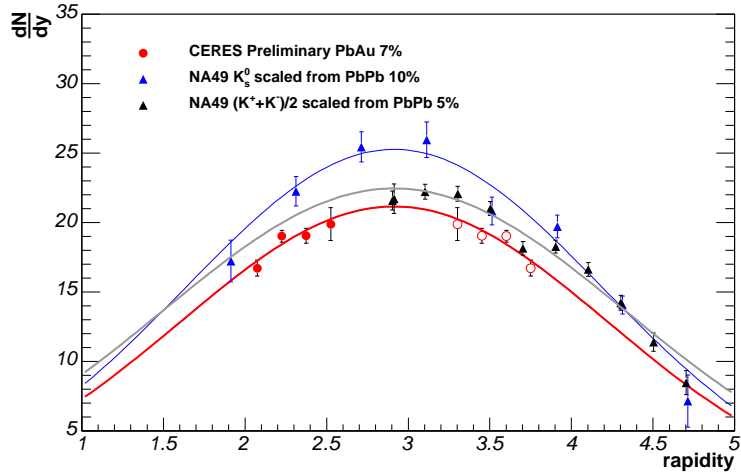


Figure 7.6: Comparison of CERES results with the mean value of the charged kaons from NA49 and preliminary results on neutral kaons. The CERES points are depicted in red, with the red fit. The NA49 charged kaons are shown as black points (note two points at midrapidity) and neutral kaons as blue triangles.

The total multiplicity measured by NA57 was published in Ref. [46]. In the measurement no particle identification was used and also tracks were not reconstructed. The value is the correlation of the number of the hits in the telescope with the multiplicity obtained using Monte-Carlo studies. The reported result is the density in the pseudo-rapidity at the maximum of $dN/d\eta$. This value is close but not equal to the maximum of dN/dy .

The NA57 result for 5% centrality is $N_{ch} = 478 \pm 10_{stat}$. The ratio of neutral kaons at midrapidity to the total multiplicity is:

$$K_S^0/N_{ch} = (30.3 \pm 2.2)/478 = (6.33 \pm 0.46)\% \quad (7.5)$$

The difference between the ratios reported by both experiments is at the level of 20%. One has to stress that the discrepancy is not in the absolute normalization but in the shape of the spectrum.

Summarizing: agreement was found with data points measured by NA57 in the area of long transverse momentum acceptance. It is unlikely that the shape as proposed by NA57 can be reconciled with the precision data presented in this work.

7.3.2 NA49

The NA49 data on charged kaons were published in Ref. [48]. Charged kaons are identified using the specific energy loss dE/dX in the TPC. The statistical error of the measurement is at the level of 2%, the systematic error for positive and negative particles is estimated to be 5%. In the case of a dE/dX measurement the statistics is not a limitation, the real issue is the proper description of the tails and is reflected in the systematic error. At midrapidity an additional point was presented with the particle type separation using the Time Of Flight (TOF) detector.

The $0.5 * (K^+ + K^-)$ values were scaled to 7% centrality and overlaid with the CERES results. The comparison is shown in Fig. 7.6. The data from CERES and NA49 agree well. The shape of both spectra is the same, with the normalization differing by around 5%, at the level of the statistical errors. The two midrapidity points from NA49 agree better with the fit from CERES than with the fit from NA49.

The difference observed, at the level of 5%, can have different sources. It can be due to the systematic error or imprecision in the centrality measurement scaling. This error is however at the level of the statistical one and below the systematic error quoted by both experiments, thus the full compatibility can be claimed.

As an additional check, the comparison of the ratio of neutral kaons to multiplicity can be made. The value from CERES is:

$$K_S^0/N_{ch} = (21.4 \pm 1.1)/400 = (5.35 \pm 0.27)\% \quad (7.6)$$

The NA49 value of the total multiplicity was constructed in [49] from the yields of pions, kaons and protons. The ratio is:

$$K_S^0/N_{ch} = (23.2 \pm 0.5)/430 = (5.39 \pm 0.12)\% \quad (7.7)$$

The ratios are in perfect agreement, at a level below 1% of the yield, below statistical errors. One has to remember the multiplicity in CERES was measured independently of this measurement. This not the case for NA49. The multiplicity is the sum of primary pions, kaons and protons thus the numerator and denominator in the ratio are correlated.

The preliminary data on K_S^0 production were obtained for 10% centrality. The interesting feature of this measurement is a wide acceptance in the rapidity around midrapidity allowing comparison of reflected points. The data points after scaling are shown in Fig. 7.6 as blue triangles.

The data points and the reflections are compatible within the statistical limit. In the rapidity range commonly measured the CERES data are compatible with one point of the NA49 data, but not with the reflected point. The large rapidity points are compatible with the extrapolation of the fit, but the midrapidity points are not.

The shape of the fit to the rapidity spectrum is similar, with the same width but the discrepancy is visible in the details and the absolute normalization. No conclusion can be drawn, due to the lack of the systematic errors in the NA49 measurement.

7.3.3 Conclusion

The results obtained with this analysis are compatible with the mean of charged kaons obtained by the NA49 experiment at the level of statistical error of 5%. Partial agreement with results from NA57 is observed.

7.4 Comparison to the thermal model

With the neutral kaons alone one can not reconstruct the temperature and the baryochemical potential of the chemical freeze-out. One can extract the parameters of the fireball using other results from central collisions at top SPS energy. The fit to all published ratios is shown in Fig. 7.7.

The global fit gives the temperature of $T = 160$ MeV and baryochemical potential of $\mu_B = 240$ MeV. For the volume of 350 participants the predicted number of K_S^0 in one unit of rapidity at midrapidity is $N = 24.8$ [54].

The prediction has to be scaled using the number of participants scaling by a factor of $\alpha = 338/350 = 0.965$, thus the prediction of the thermal model for AuPb collisions with centrality of 7% is $N = 23.9^1$.

The value obtained in this work after integration of the fit is $N = 20.6 \pm 0.9_{stat} \pm 1.6_{syst}$. The value is extrapolation dominated, since in the range of one unit around midrapidity there are no measured points. The thermal model gives yield greater by 16%.

The best method to compare the data and the model would be a statistical analysis. This can not easily be performed here, because the measurement has both statistical and systematic errors. Two options will be discussed. The first option is to add statistical and systematic errors quadratically and treat the result as statistical, then the error is:

$$\epsilon_1 = 9\%. \tag{7.8}$$

¹The error of the model prediction, due to fitting experimental data and scaling to CERES trigger is not evaluated. The error can be expected to be lower than the experimental error.

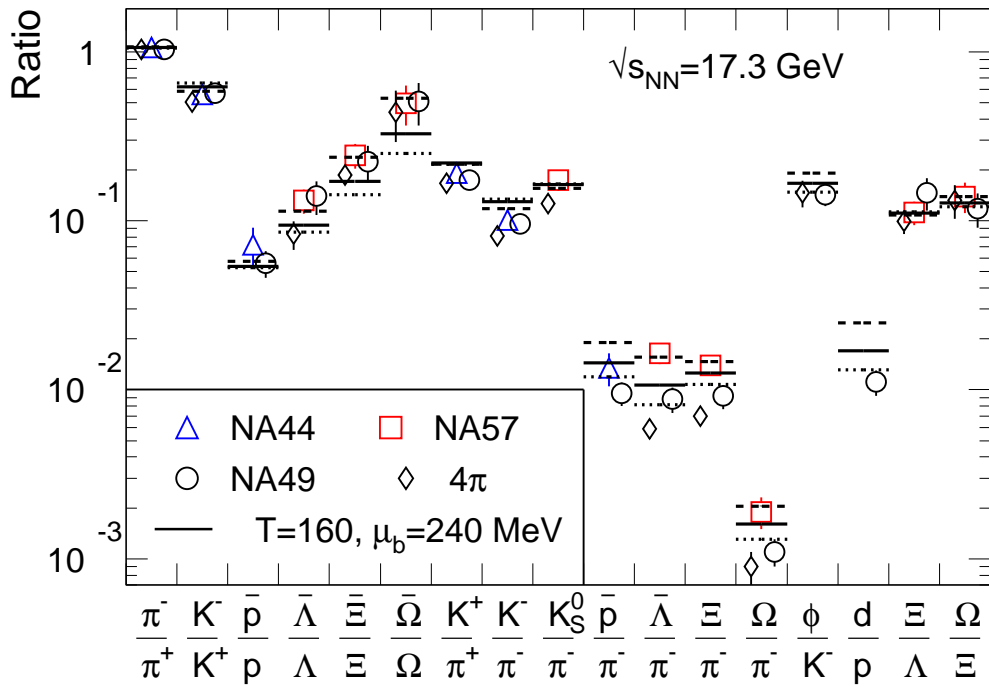


Figure 7.7: Fit of the thermal model to data at top SPS energy. Plot from Ref. [9].

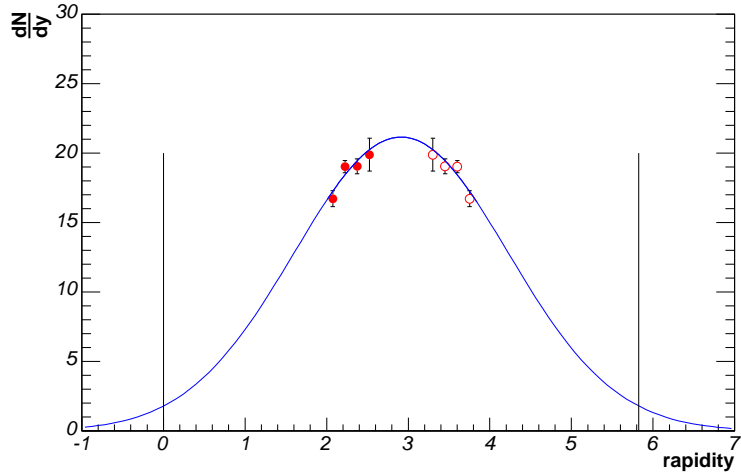


Figure 7.8: The full rapidity spectrum. The closed symbols represent measured and open symbols reflected points. The Gaussian fit is extended to range $(-1, 7)$ and two lines show rapidity of the target and of the beam.

Using this estimation of the error the difference between the data and the prediction of the thermal model is 1.8σ . Statistically around 5% of measurements will give results different by more than 1.8σ , which means a compatibility of data and the model within the statistics.

The second option is based on the assumption that all the values inside the systematic error are equally probable and outside this range the statistical error, following Gaussian distribution, is used. In this approach the difference is $(16\% - 8\%)/4\% = 2\sigma$.

Two important aspects have to be taken into account. The first is the fact that the thermal model was fit to all available data, which also contain the results from NA57, which are incompatible with the results presented here. Thus a small correlation to previously discussed values has to be taken into account. The second complication is the fact that the data at hand are an extrapolation to midrapidity

Summarizing, the results obtained are in agreement with the thermal model of hadron gas. The models with the strangeness suppressed by around 10 – 20% with respect to the thermal model of hadron gas will also be supported by data.

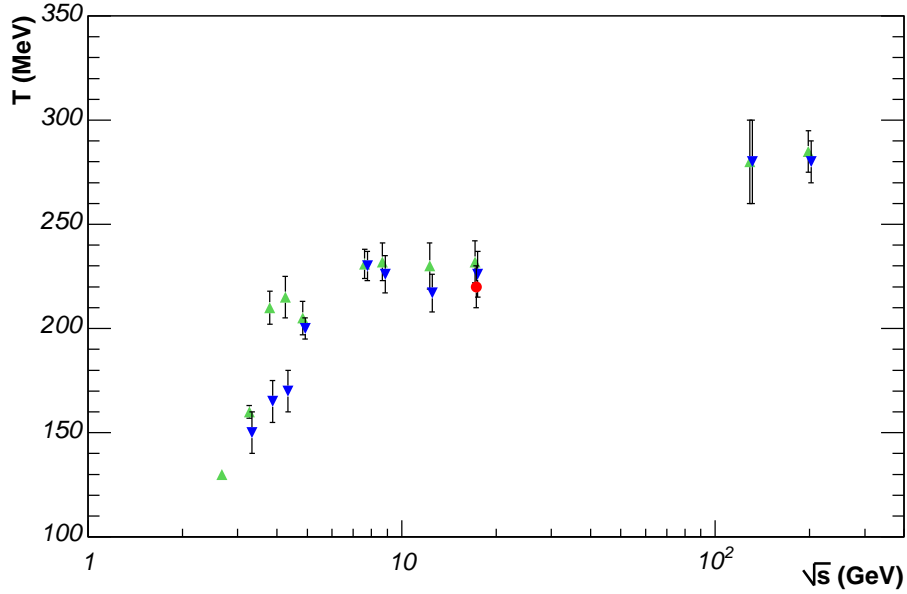


Figure 7.10: Temperature of kaons. Positive kaons: green, negative kaons: blue, this analysis: red. The error bars represent statistical and systematic errors added linearly.

increase in temperature stops at critical temperature T_c due to the steep rise of the energy density with the temperature. For higher energies the temperature grows slowly with energy. The calculation shows that the system created at SPS has a temperature equal to the critical temperature and the RHIC energies give higher temperatures.

The systematics of kaon temperature, which is a convolution of the actual temperature and the collective expansion, is shown in Fig. 7.10. The error bars represent statistical and systematic errors added linearly. The point obtained in this work, is in the agreement with the overall systematics.

The data shows an increase in the number of degrees of freedom at SPS energies. The current data set can not discriminate between a smooth function and a mixed phase scenario. The RHIC results at energy $\sqrt{s} = 60$ AGeV with precision better than $\delta T = 10$ MeV would provide discriminating power between the two scenarios.

8 Reconstruction of neutral strange baryons

The aim of this thesis was the precision measurement of the neutral strange mesons – K_S^0 . With the programs and the procedures developed for this purpose the reconstruction of the strange baryon Λ and anti-baryon $\bar{\Lambda}$ is possible. The full procedure of the reconstruction will not be described; only the results and important differences of this analysis to the K_S^0 analysis are presented.

8.1 Hyperons in heavy ion collisions

The Λ have decay pattern similar to that of K_S^0 :

$$\Lambda \rightarrow p\pi^- \tag{8.1}$$

with the branching ratio $r = (63.9 \pm 0.5)\%$. In case of Λ , unlike the case of K_S^0 , the decay is not symmetric and the proton carries most of the momentum. This asymmetry is visible in the Armenteros plot of the decay topology shown in Fig. 4.23.

In case of K_S^0 the pions were not only symmetric but also have the same momentum distribution as the primary pions, thus the decay topology was determined by the detector. This is not the case for Λ particle. The momentum released during the decay is low, $q = 101 \text{ MeV}/c$, and thus also the opening angle is low. Due to low opening angle, one can not expect the back-to-back decay topology will fall into the acceptance, thus the acceptance will not start at $p_T = 0 \text{ MeV}/c$ and obtaining the yield of the neutral strange baryon will need extrapolation of the transverse momentum spectrum.

Λ is feed-down by Σ^0 particle and multi-strange particles. The Σ^0 decays electromagnetically $\Sigma^0 \rightarrow \Lambda\gamma$ with branching ratio $r = 100\%$. This decay is very difficult to resolve and thus the Λ content in the thermal model contains feed-down from Σ^0 .

The multi-strange baryons Ξ decay weakly into Λ and the pion:

$$\Xi^0 \rightarrow \Lambda\pi^0 \tag{8.2}$$

$$\Xi^- \rightarrow \Lambda \pi^- \quad (8.3)$$

with the branching ratio greater than $r > 99\%$. Other decay channels also lead to Λ . The relative abundance of Ξ^- particles is $\Xi^-/\Lambda = 0.1$ according to the results from NA57 [23]. For the isospin-symmetry reasons the same number of Ξ^0 shall be present. Additional correction, suppressed by the order of magnitude is the contribution from triple strange baryon Ω^- . The Ω^- decays:

$$\Omega^- \rightarrow \Lambda K^- \quad (8.4)$$

with the branching ratio of $r = (67.8 \pm 0.7)\%$. Other decay channels include Ξ thus at the end every Ω particle produces one Λ .

The data presented here will not be corrected for feed-down from multi-strange baryons. The important question is if the efficiency for the reconstruction of late Λ s is the same as for prompt ones and if the spectrum of the Λ s from decays is the same as the spectrum of the prompt Λ s.

The lifetime of multi-strange baryons is smaller than that of Λ and the Λ carries most of the momentum of the original particle. These two facts suggest, the reconstruction efficiency of prompt and late Λ s is the same. If both conditions are fulfilled the numbers have to be corrected down by around 20% – 25%. If the reconstruction efficiency or the spectrum are different, even by a small amount, the results can be significantly influenced due to large extrapolation of the spectrum to low transverse momentum.

8.2 Data analysis and reconstruction scenario

8.2.1 Acceptance and Phase-space segmentation

The acceptance after phase-space segmentation is shown in Fig. 8.1. The upper panel shows the signal in a given bin and the bottom shows the acceptance. The measurement is possible in the rapidity range $1.8 < y < 2.6$ which was segmented into 4 bins covering 0.2 units each. The rapidity bins will be numbered from (1) to (4).

The acceptance for the Λ starts at transverse momentum $p_T > 0.5$ GeV/c. This fact means, a small fraction of the cross-section will be actually measured and obtaining total number of Λ will need extrapolation. As discussed in the introduction, this is due to the absence of the back-to-back topology. The shape of the acceptance is aligned along the polar angle of the Λ and thus has a banana shape in the rapidity – transverse momentum

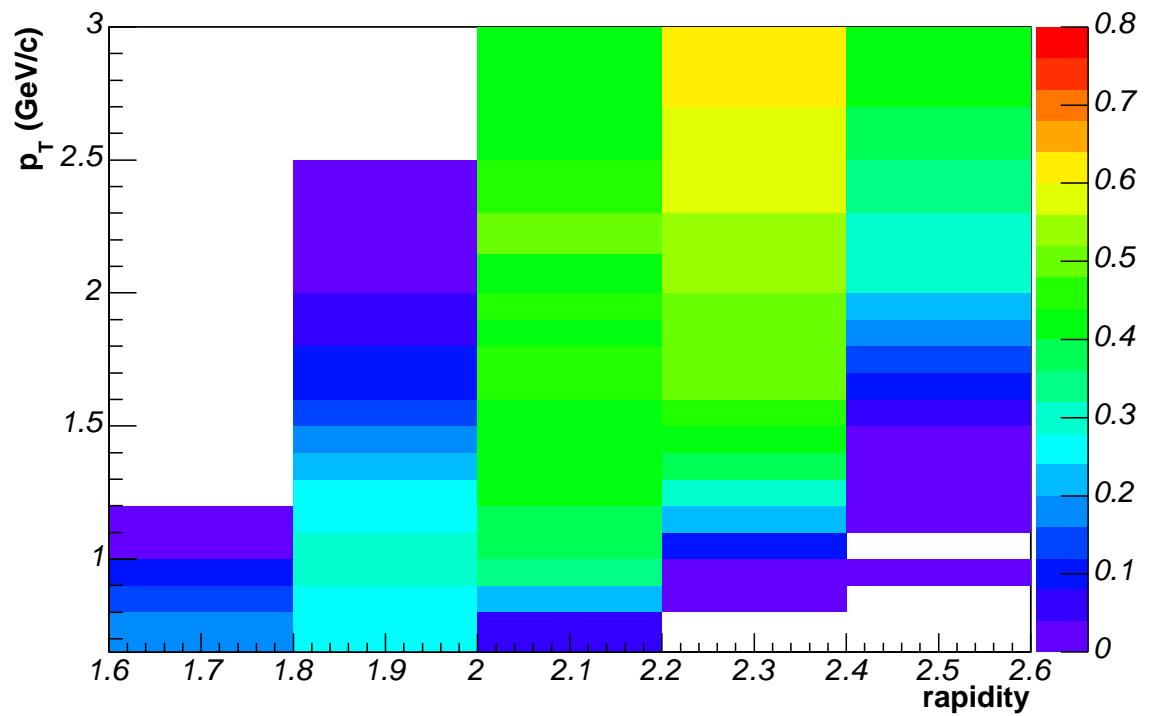
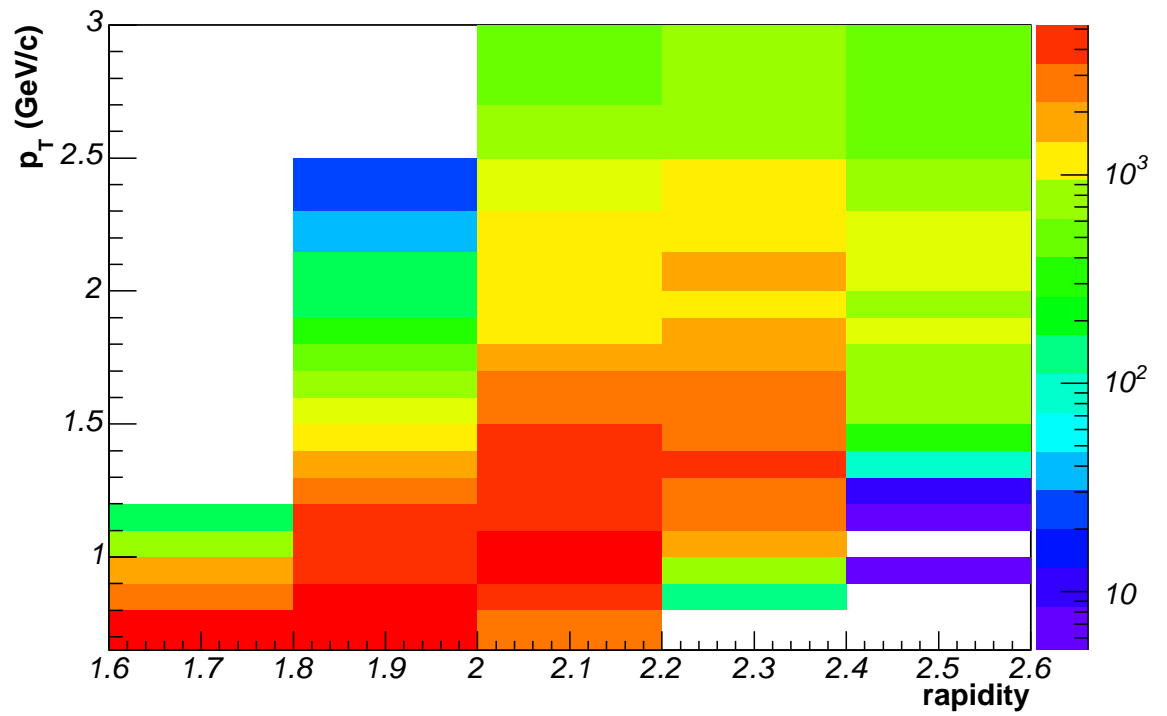


Figure 8.1: Acceptance for Λ . Upper panel: expected signal after acceptance cuts, lower panel: acceptance in transverse momentum – rapidity bins.

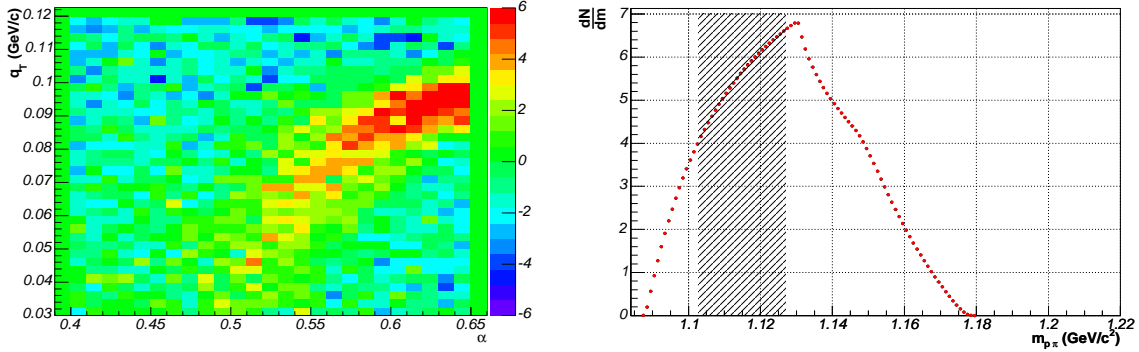


Figure 8.2: Λ reconstruction. Left: Armenteros plot, right: invariant mass spectrum, shaded region shows the position of the Λ peak.

space. The last rapidity bin has transverse momentum cut of $p_T > 1$ GeV/ c thus it can be used to control the systematics but the extrapolation to obtain the multiplicity measurement will be problematic.

Acceptance efficiency is relatively flat, at the level of $\eta \simeq 40\%$ and falls to lower values at the borders.

8.2.2 Pair cuts and contamination

When a positive pion originating from a neutral kaon is misidentified for a proton, a pair can look like a Λ . This is illustrated on the Armenteros plot, in the region where the lines of neutral kaon and Λ cross.

The contamination can be removed in many different ways. One of the methods is the cut in the Armenteros space. This method worked very well to clean K_S^0 from Λ ; however, in the opposite case, the cut shapes the invariant mass spectrum in a drastic way as illustrated in Fig. 8.2. The rapid fall of the spectrum, beyond the Λ mass is due to the Armenteros cut. The shape of the spectrum at the border of the Λ signal brings many problems with the normalization of the mixed events.

The characteristics of pions from K_S^0 is the same as from the bulk, and the opening angle distribution is shaped by the acceptance. This is not the case with Λ . The transverse momentum of the pion is low and also the opening angle is below $\psi < 0.2$ rad. These were used to remove neutral mesons and do not destroy the shape of the invariant mass spectrum.

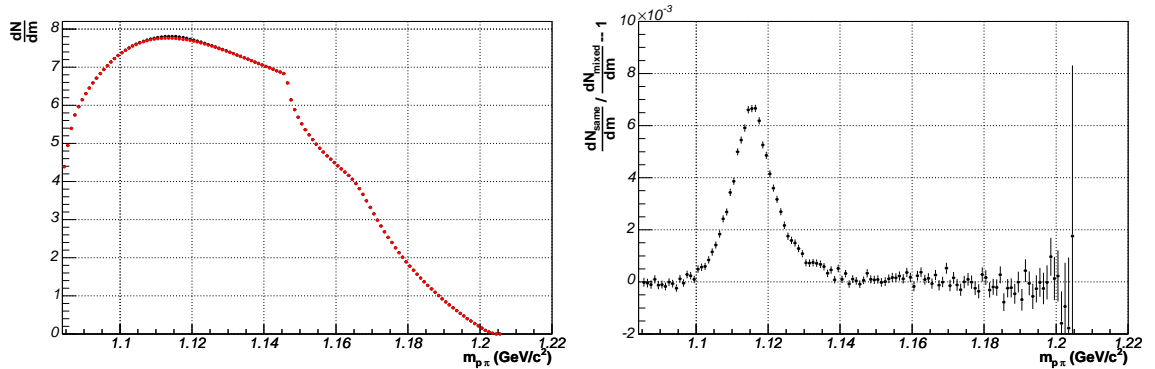


Figure 8.3: Proton–pion invariant mass spectrum. Left panel: the spectrum, same events in black and mixed events in red. Right: ratio of the same events to mixed events, suppressed for unity. The spectra were normalized above the Λ mass.

8.2.3 Invariant mass spectrum

The invariant mass spectrum is shown in Fig. 8.3. The spectrum was shaped using the Armenteros cut so the Λ peak is located at the top of the distribution at a smooth plateau. The ratio of same-to-mixed events is shown in the right panel in Fig. 8.3. The mixed events were normalized to same events above the Λ mass and the normalization works well also in the range below the Λ mass.

The signal of Λ particles was obtained by subtracting normalized mixed events from same events. The resulting spectrum is shown in Fig. 8.4. The spectrum was fit with a Gaussian. The fit has three parameters: the yield, the mass and the mass resolution. The reconstructed mass is: $\mu = 1115.77 \pm 0.06 \text{ MeV}/c^2$ in the agreement with the PDG value of $\mu = 1115.683 \pm 0.006 \text{ MeV}/c^2$ [14]. The difference of $0.09 \text{ MeV}/c^2$ is compatible with the statistical error. The spectrum is not fully described by the Gaussian shape due to the different mass resolution of Λ s with different momentum. The peak is an overlay of many Gaussians with different widths.

8.3 Results in rapidity – transverse momentum bins

8.3.1 Normalization of the mixed events

Initially the number of pairs in same and mixed events is the same, due to the selection of the events for mixing. After applying pair cuts, in particular the Armenteros cut, this is no longer the case. The true Λ always pass the Armenteros cut, while the combinatorial pair have some probability to pass it.

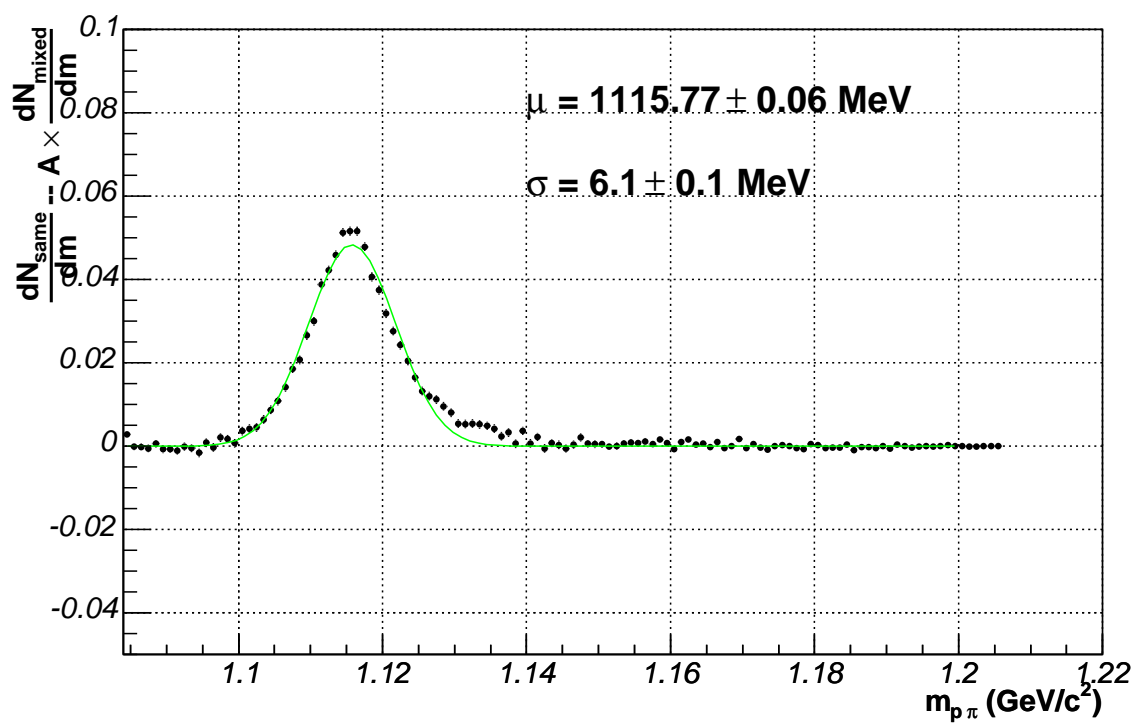


Figure 8.4: Signal of the Λ with a Gaussian fit.

There are two extreme possibilities in the normalization of the mixed events. In the first, no normalization is applied and the second is to normalize to the number of entries in same and mixed events. The second method does not work properly, because the ratio of the number of entries in the Λ peak to the total number of entries is at the level of 10^{-3} . The difference in the extracted Λ peak with two extreme normalizations amounts to around 5% and is greater than the statistical error of the yield.

The actually applied procedure normalizes the mixed events to the background entries in same events. The procedure works on the bin-by-bins basis and is the following. First the signal is created without any arbitrary normalization of mixed events and the Λ signal is extracted. Then mixed events are normalized to the number of pairs in same events minus number of entries in the Λ peak. The number of entries in the Λ peak depends on the normalization so the procedure is repeated iteratively for 10 times.

8.3.2 Fit parameters and the raw yield

The signal was divided into transverse momentum – rapidity bins and after the normalization was fit with a Gaussian. No offset or residual background were present in the fit. The extracted parameters are shown on the consecutive panels. The extracted raw yields are shown on the left column in Fig. 8.5 for four rapidity bins and the right column shows the statistical significance of the signal. The signal is strong, the maximum significance is around 20 – 30 in the bulk and decreases slowly toward high momentum.

The reconstructed mass and the mass resolution on the bin-by-bin basis are shown in Fig. 8.6 The left column shows the difference between the reconstructed mass and the PDG value. Except the (3) rapidity bin where the high momentum Λ have higher reconstructed mass, the mass does not diverge more than allowed by the statistical fluctuations. The mass resolution is shown in the right column in Fig. 8.6. The trend of the resolution in Monte-Carlo and in data is the same and the two lines agree well. The resolution obtained in data tends to be worse up to 10%.

8.3.3 Corrected transverse momentum spectrum

The raw yields presented in Fig. 8.5 were corrected for the acceptance and efficiency and are shown in Fig. 8.7. The left column shows the transverse momentum spectrum in linear scale while the right column in the logarithmic scale. The data points are accompanied by a set of lines. The black lines show the correction factors. The four correction factors have all different systematics. For low rapidity bins the correction factor increases with transverse momentum, for high rapidity bin it decreases and for central bins it is flat. The

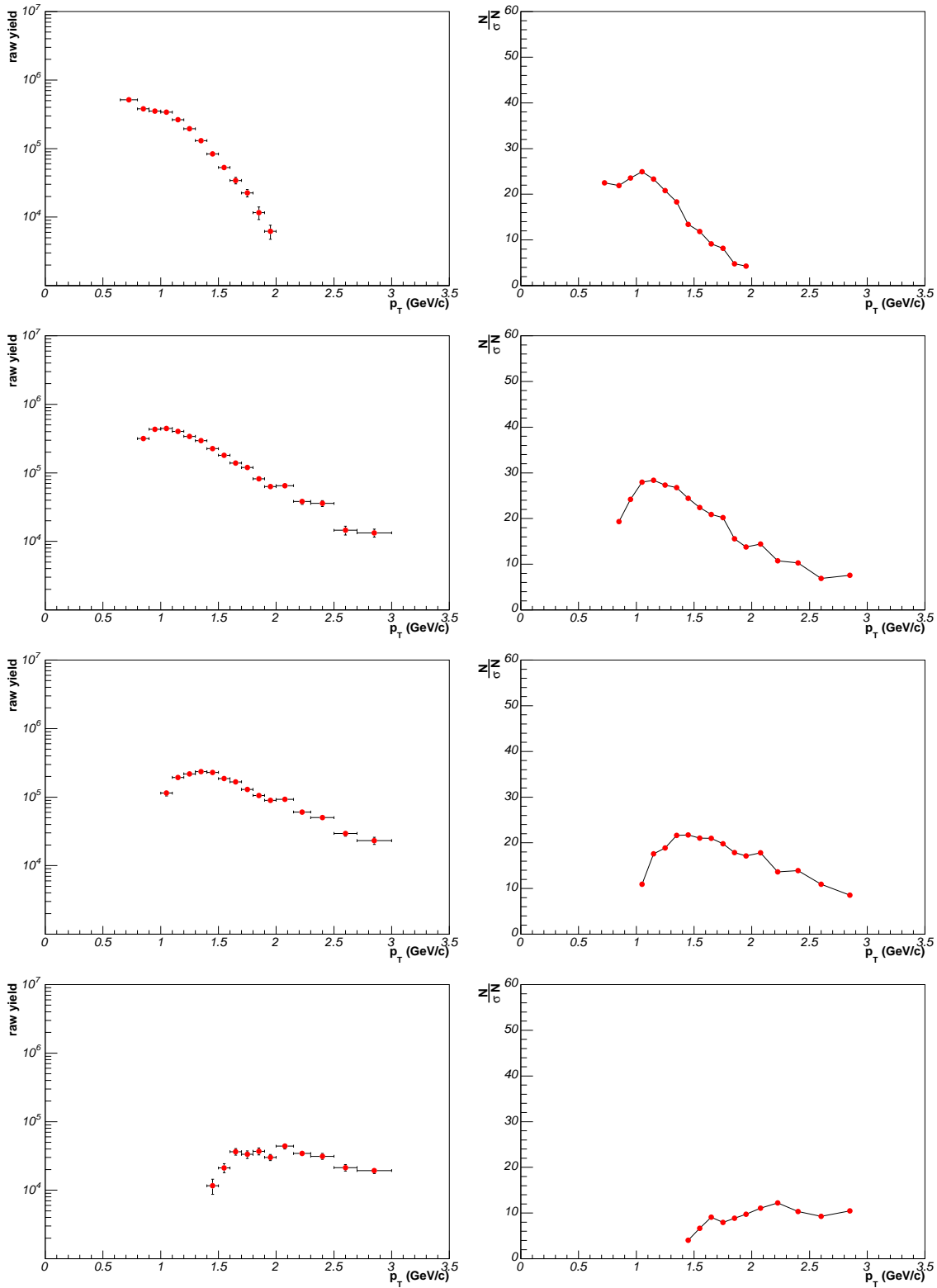


Figure 8.5: Extracted yield. Left column: raw yield, right column: statistical significance of the peak. Rows are for four rapidity bins.

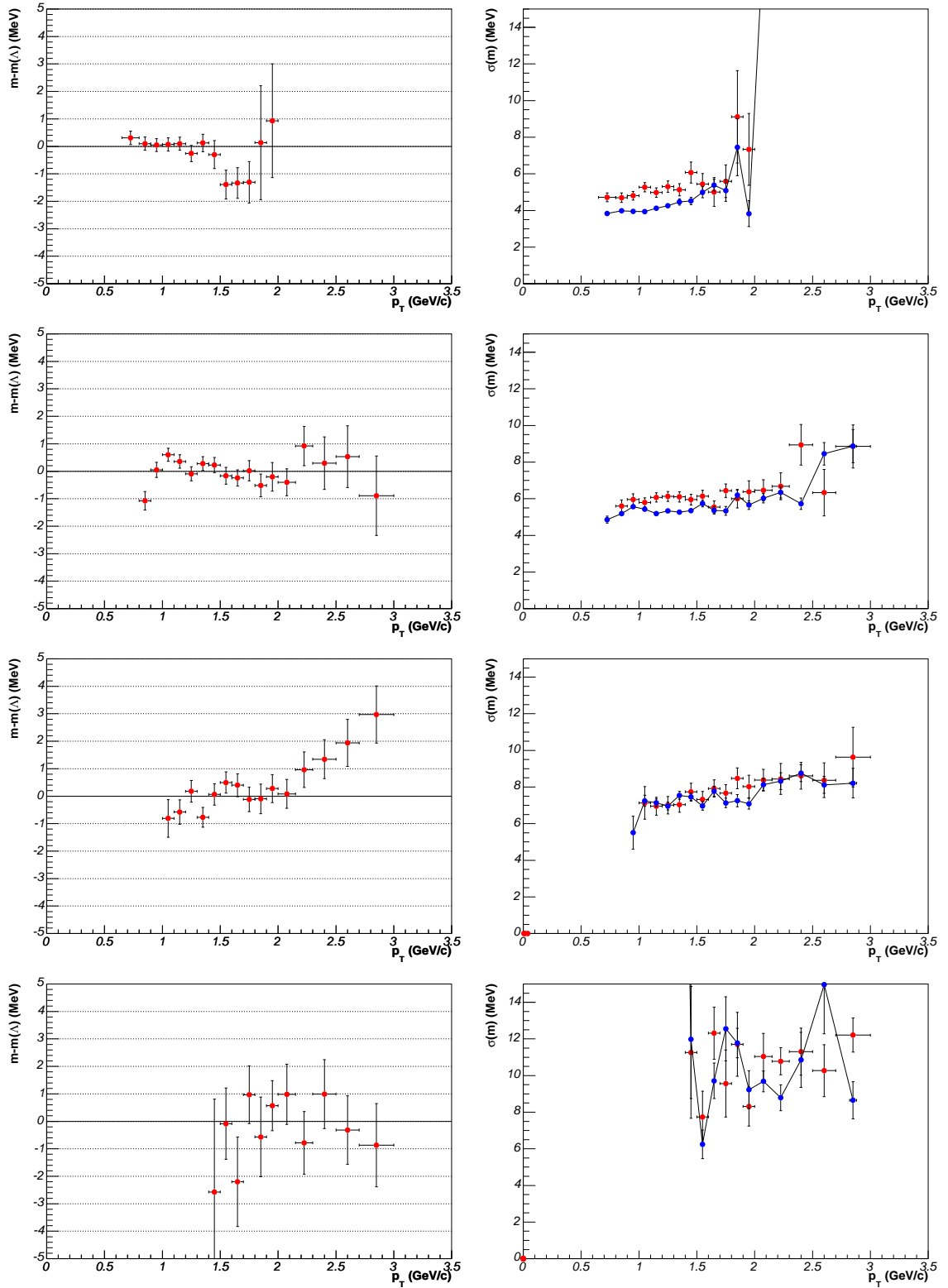


Figure 8.6: Extracted mass and the resolution. Left column: offset of the reconstructed mass, right column: reconstructed width of the peak, data are depicted in red and the Monte-Carlo value in blue. Rows are for rapidity bins.

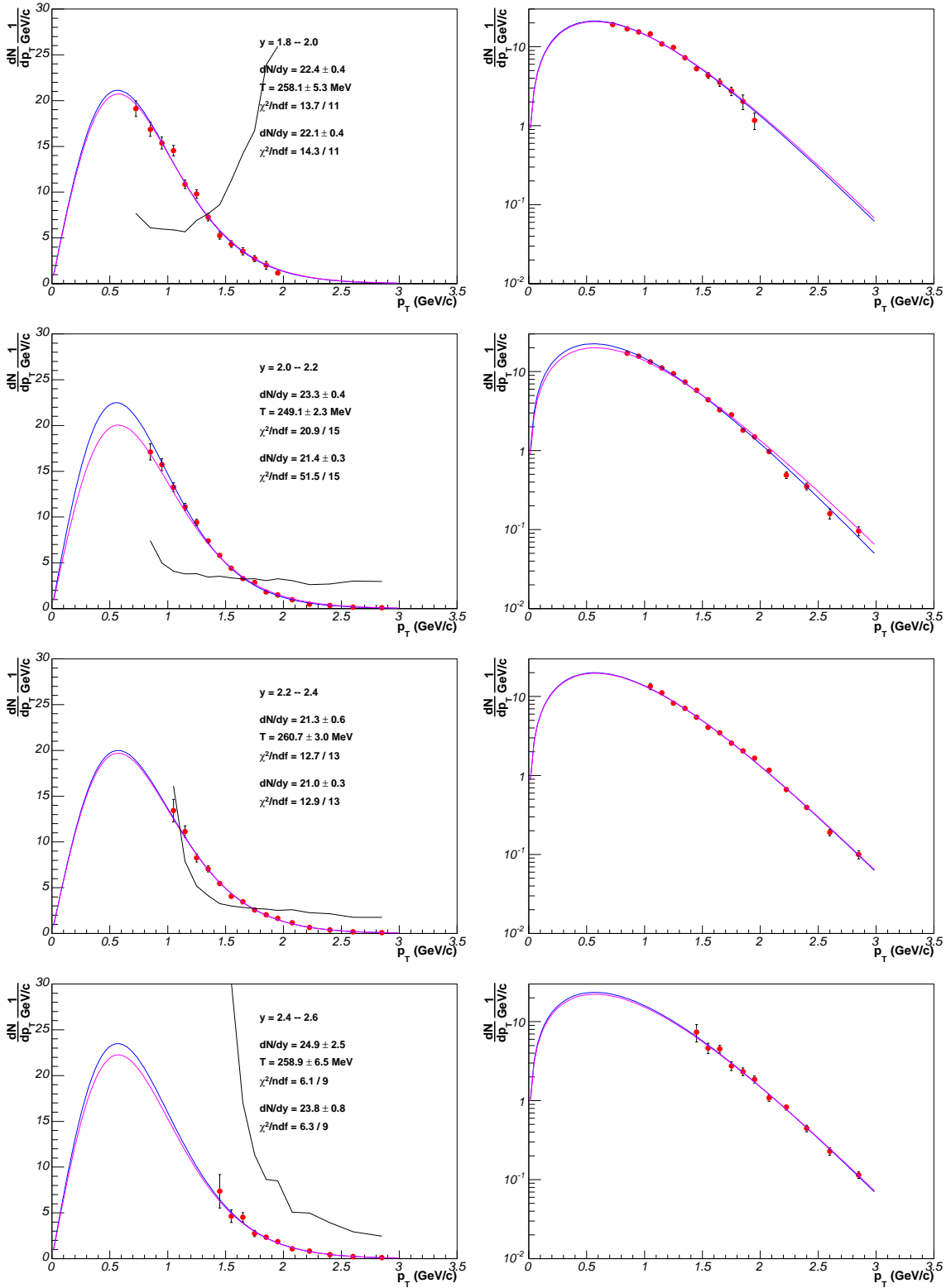


Figure 8.7: Corrected spectra in linear (left) and logarithmic scale (right). The Boltzmann fit with two parameters is depicted in blue and the fit with the common temperature in magenta. The black like shows total correction factor. Fit parameters are displayed on the panels.

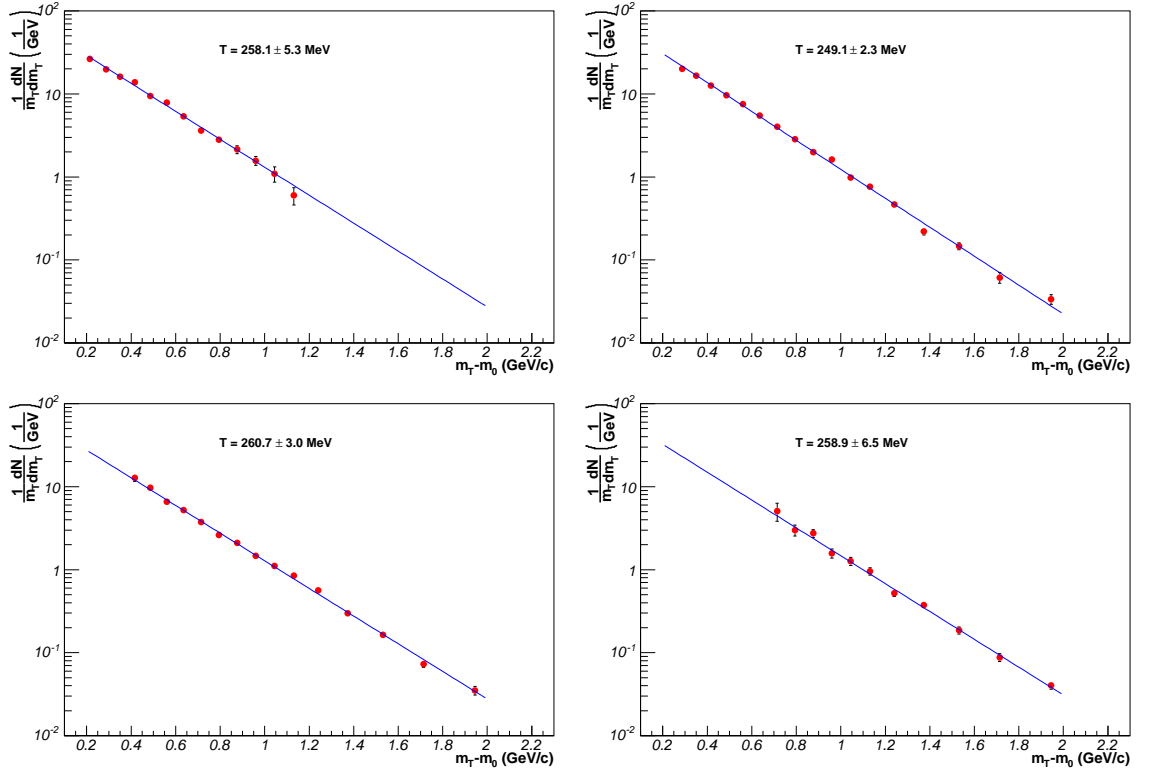


Figure 8.8: Transverse mass spectra for four rapidity bins.

red line shows the three-parameter fit by Eq. 6.6 while the blue line shows the same fit performed with the common temperature of 260 MeV.

The panels contain the following informations:

- rapidity range
- parameters of the fit: dN/dy , temperature and χ^2/NDF
- parameters of the fit with common temperature: dN/dy and χ^2/NDF

The data follows the fit line, which is also visible in the χ^2/NDF value displayed on the plot. For all cases the χ^2 value is comparable with the number of degrees of freedom. The resulting temperatures are consistent with the common temperature except for the bin (2) where the reconstructed temperature is lower by 10 MeV.

8.3.4 Transverse mass spectrum

The transverse mass spectrum, recalculated from the transverse momentum spectrum is shown in Fig. 8.8. It is important to note, the spectrum in bin (2) with the temperature lower than the others is the longest spectrum spanning transverse mass range of $1.8 \text{ GeV}/c^2$.

8.3.5 Test of the transverse momentum spectrum

The stability of the fit was tested by fitting a subset of the spectrum. This procedure is the same as for K_S^0 and the results are displayed in Fig. 8.9. The left column shows the reconstructed yield and the right the reconstructed temperature.

For most of the spectra the fits are stable. The results obtained in bin (3) are difficult for the interpretation, taking into account that the points are correlated. Considering uncorrelated points: the first, 5th and 10th, the shape can be attributed to the statistical fluctuations.

From the plots presented above the conclusion can be drawn the transverse mass of Λ follows the exponential distribution in the region $m - m_\Lambda = 0.3 - 2 \text{ GeV}/c^2$.

8.3.6 Rapidity spectrum

The rapidity spectrum is presented in the left panel in Fig. 8.10. The spectrum was fit with a straight line and the result of the fit is displayed in the figure. The rapidity dependence of temperature is shown in the right panel of Fig. 8.10. The spectrum was fit with a straight line and gave the result $T = 254 \pm 2 \text{ MeV}$.

8.4 Comparison to other experiments

The data can be compared to results from NA49 and NA57. The yield reported by NA57 [23] in the central events, without feed-down correction is:

$$\frac{dN}{dy} = 18.5 \pm 1.1_{stat} \pm 1.8_{syst} \quad (8.5)$$

and the temperature [45]:

$$T = 305 \pm 15_{stat} \pm 30_{syst} \text{ MeV} \quad (8.6)$$

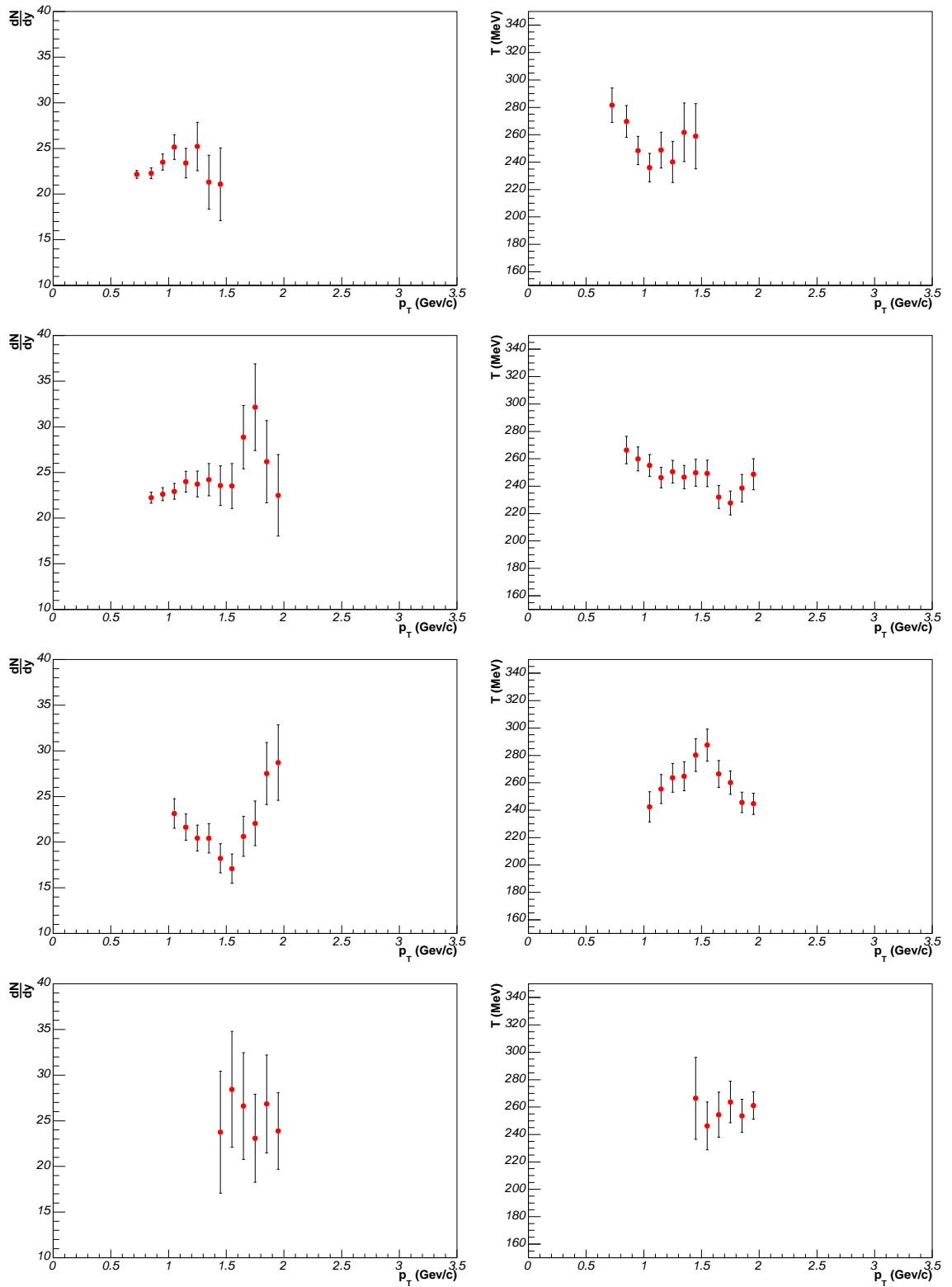


Figure 8.9: Analysis of the transverse momentum spectrum by fitting subsets of data. See text.

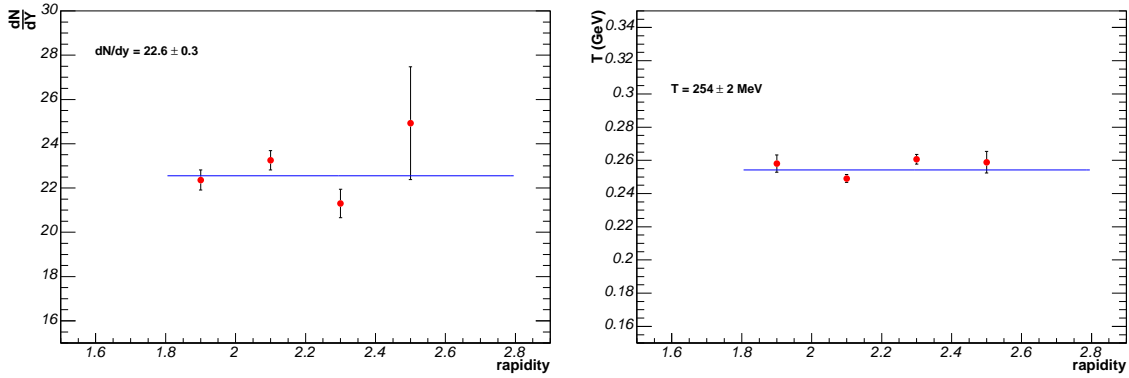


Figure 8.10: Rapidity spectrum of the Λ yield (left) and of the temperature (right).

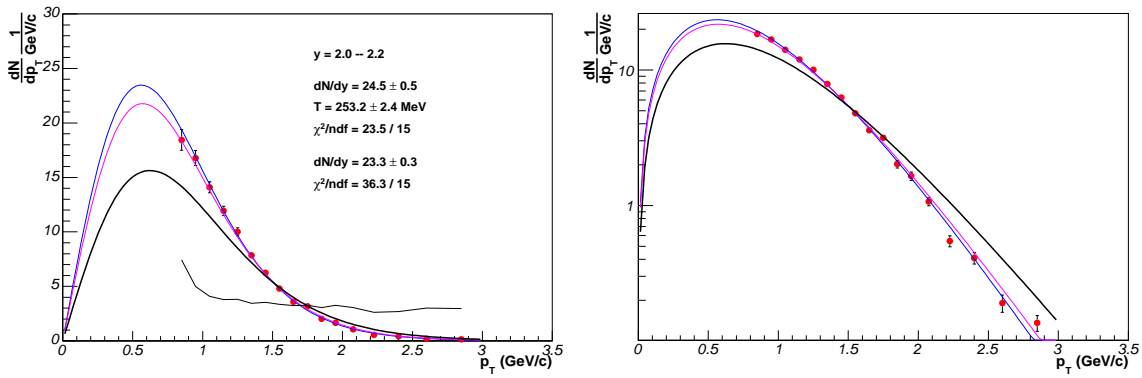


Figure 8.11: Comparison of the Λ spectrum to NA57, the NA57 fit is presented as a black line. Left: linear scale, right: logarithmic scale.

Both values of the multiplicity density are similar, but this has to be treated as accidental since the temperatures differ by $\Delta T = 50$ MeV. In a case of the spectrum with a large extrapolation the yield and the slope are strongly correlated. The transverse momentum spectra have to be directly compared.

Comparison between two spectrum is presented in Fig. 8.11 where disagreement at the level of 30% is visible. The NA57 have lower yield in the range below $p_T = 1.5$ GeV/c then the two yields agree and the NA57 yield is greater at higher transverse momentum. The difference at low transverse momentum can be connected with the steeply changing correction factor of this analysis. In short, a disagreement between the two results was found and the source is probably in the data reported here, most probably in the impact of the feed-down correction on the spectral shape.

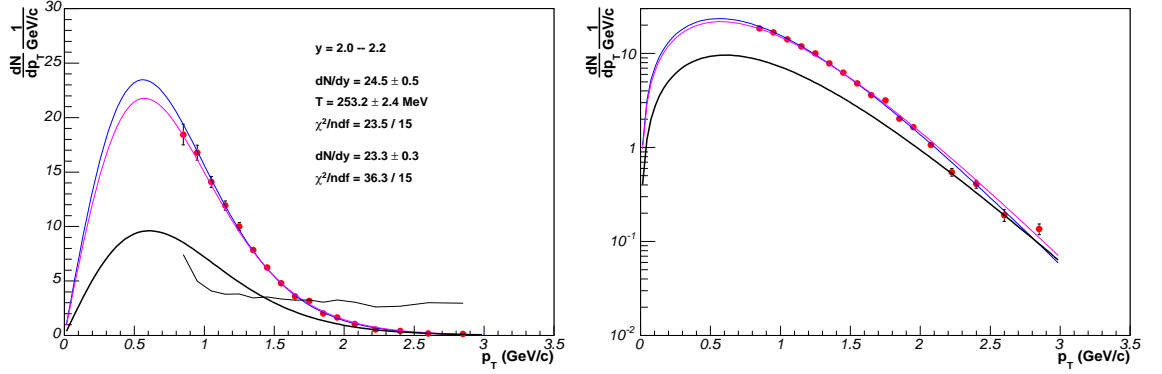


Figure 8.12: Comparison of the Λ spectrum to NA49, the NA49 is presented as a black line. Left: linear scale, right: logarithmic scale.

The NA49 experiment reported the results in Ref. [59]. The obtained yield corrected for feed-down contributions is

$$\frac{dN}{dy} = 11 \pm 1_{stat} \pm 1.3_{syst} \quad (8.7)$$

and the temperature is:

$$T = 290 \pm 19_{stat} \text{ MeV}. \quad (8.8)$$

The transverse momentum spectrum does not fully follow exponential line, the low transverse momentum points are above the fit. The comparison is shown in Fig. 8.12 where difference between the two experiments is visible in the low transverse momentum range and partial agreement at high p_T .

Summarizing, the data disagree with other experiments at the level comparable to general disagreement between SPS experiments. The two experiments: NA49 and NA57 disagree substantially on the absolute yield but the shape of the spectrum reflected in the temperature is similar. This is not the case for this measurement with the reconstructed temperature lower than reported by other experiments.

Before any conclusion can be drawn data presented here have to be upgraded with the simulation of the impact of the multi-strange baryons on the spectrum. With the results at hand the SPS Λ puzzle can not be resolved.

8.5 Anti-baryon to baryon ratio

Since the reconstruction efficiency of the Λ and $\bar{\Lambda}$ is the same the anti-baryon to baryon ratio can be made on the raw signal. The invariant mass spectrum of the $\bar{p}\pi^+$ pairs is

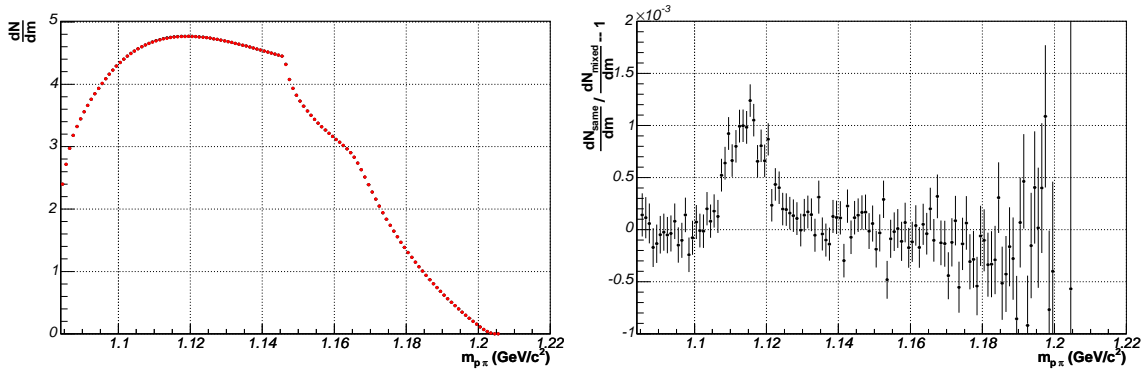


Figure 8.13: Anti-proton – pion invariant mass spectrum. Left: the spectrum from same (red) and mixed pairs (black). Right: the ratio of same to mixed events after normalization.

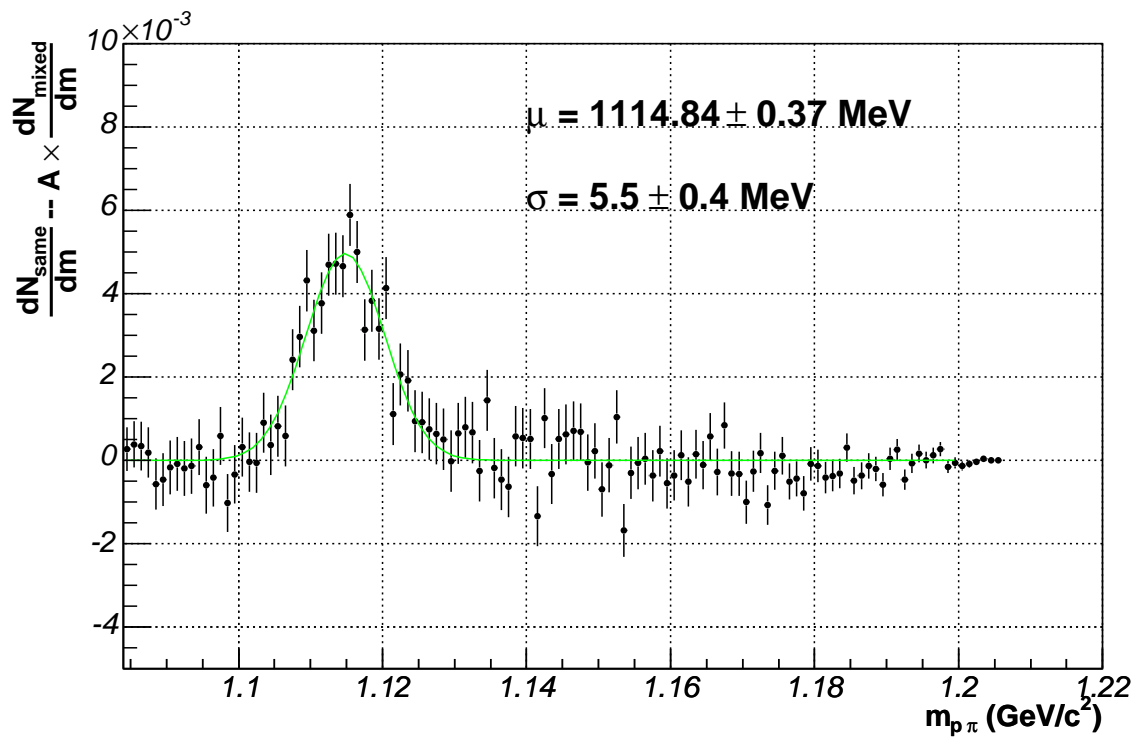


Figure 8.14: $\bar{\Lambda}$ peak fit with a Gaussian.

shown in Fig. 8.13 and the $\bar{\Lambda}$ peak, after subtraction of the combinatorial background is shown in Fig. 8.14. The signal-to-background ratio is at the level of 10^{-3} and the significance of the peak is at the level of 15, thus the overall statistical precisions is low.

The raw signal of $\bar{\Lambda}$ and Λ in four rapidity bins in the range $1.8 < y < 2.6$ is shown in Fig. 8.15. The signal for Λ was obtained for all bins and for $\bar{\Lambda}$ for the first three bins. The last bin contains practically no signal.

The $\bar{\Lambda}/\Lambda$ rapidity spectrum was fit with a Gaussian and the result is presented in Fig. 8.16. The points are well aligned on the fit and the extrapolated ratio at midrapidity is:

$$\frac{\bar{\Lambda}}{\Lambda}|_{y=0} = 0.125 \pm 0.014 \quad (8.9)$$

the width is $\sigma = 1.0 \pm 0.2$. The data were compared in Fig. 8.17 to data points from NA49 and the fit from NA57, the fit covers the acceptance of NA57.

Relatively good agreement between all three experiments is visible. The data from NA49 have higher ratio but the width of the spectrum is the same as for data reported here. The NA57 have the same value but the width reported by the collaboration is factor 2 smaller than the data obtained here. In terms of the acceptance the two measurements are complementary and the smooth transition from CERES to NA57 is visible.

8.6 Interpretation and Outlook

The data presented here are not fully elaborated in terms of impact of decays of the multi-strange hyperons. Additional simulations are needed to clear the impact of the feed-down on the spectrum and total yield. With optimization of the kinematic cuts one can expect to decrease the lower border of the acceptance by $\Delta p_T \sim 100$ MeV/c this will give better constrain on the shape of the transverse momentum spectrum. With data at hand the SPS Λ question can not be answered in a reliable manner.

The anti-baryon to baryon ratio gives similar results by all experiments. The data presented here are closer to NA49 in terms of the width of the distribution and closer to NA57 in terms of absolute value.

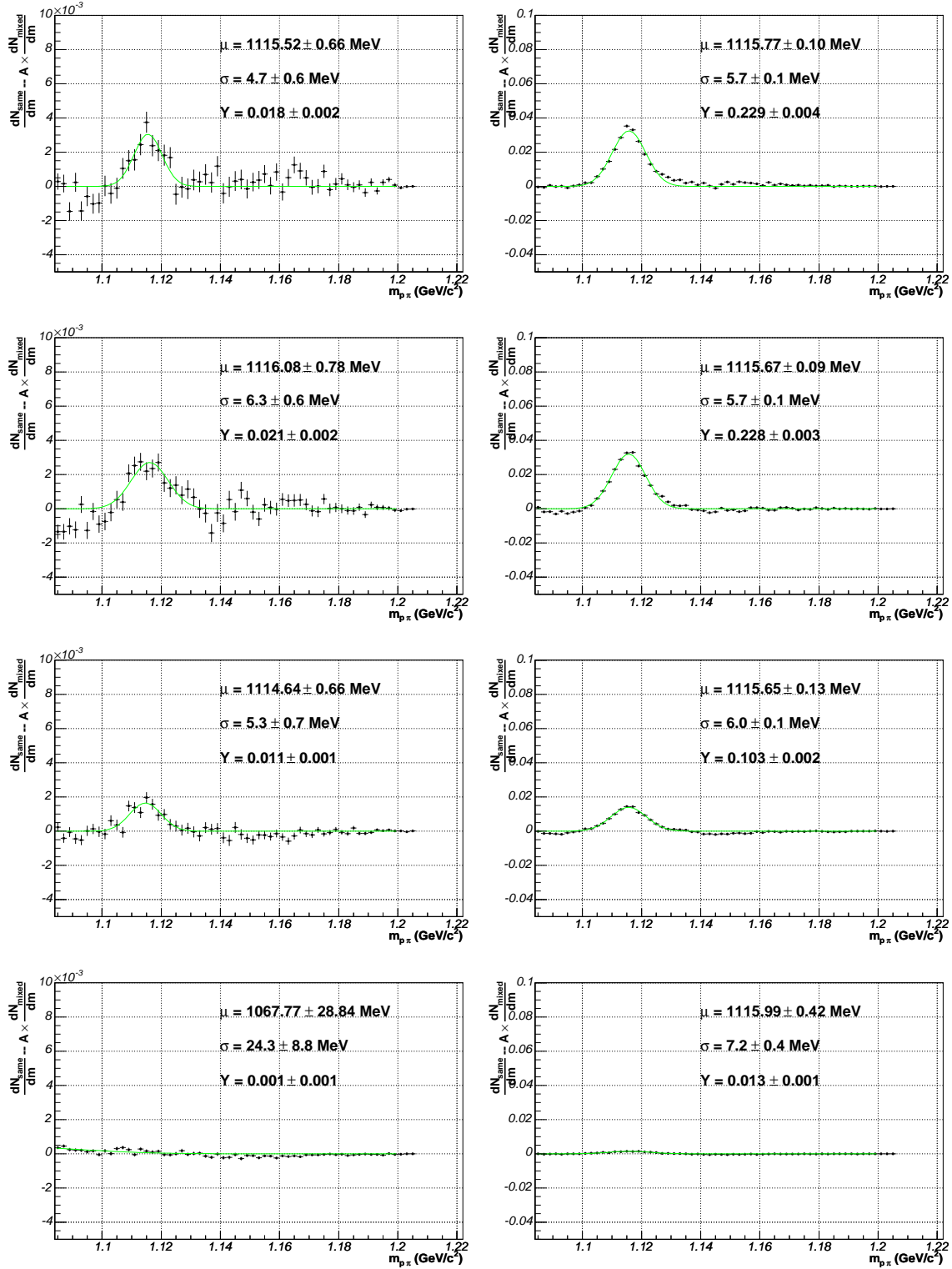


Figure 8.15: Raw signal of $\bar{\Lambda}$ (left) and Λ (right) in 4 rapidity bins.

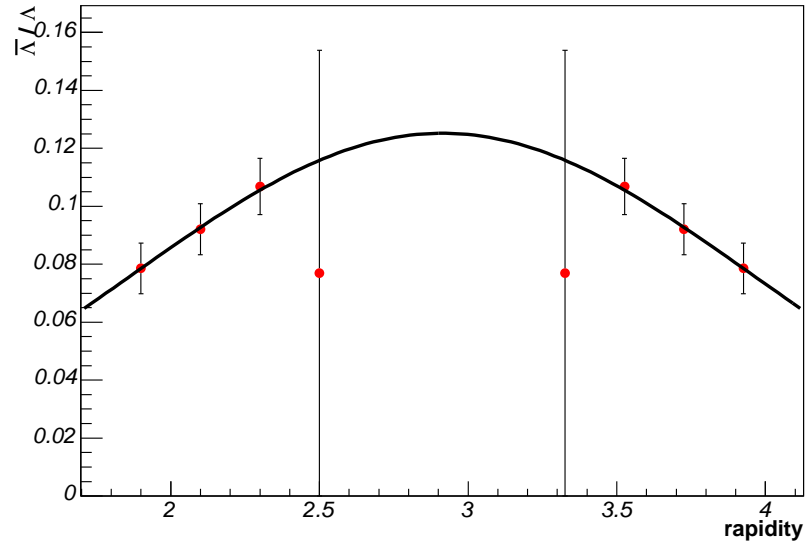


Figure 8.16: $\bar{\Lambda}$ to Λ ratio.

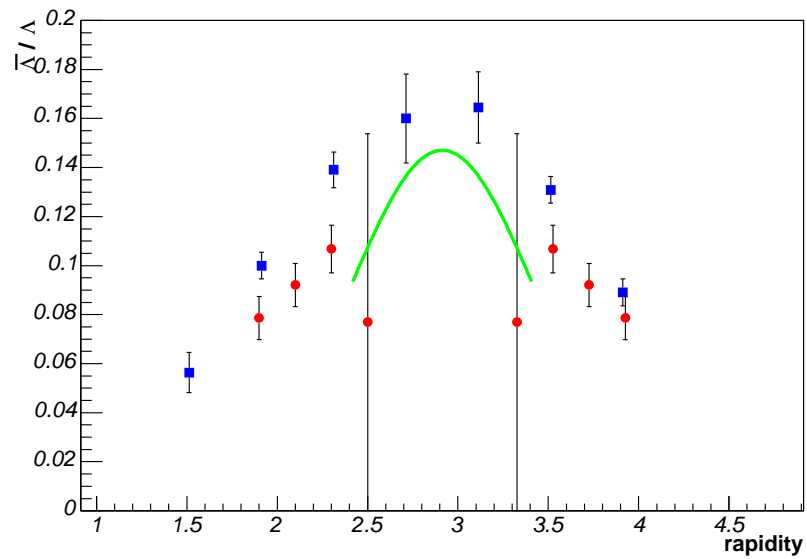


Figure 8.17: $\bar{\Lambda}$ to Λ ratio, comparison to NA49 (blue points) and NA57 (green line)

9 Summary and outlook

In the first chapter the question was asked whether the systematics of the strange particle production follows a smooth lines as predicted by the thermal model or whether a sharp structure develops. The subsequent precision measurement of the K_S^0 presented in this work is one of the measurements to corroborate on the issue.

The whole argument about the sharp structures in the strangeness production was based on data collected by the NA49 experiment. The results were later challenged by the yields obtained by the NA57 collaboration.

The results presented in this work are in the agreement with data of NA49 and also the source of disagreement with NA57 was pointed out. With data at hand the interpretation of K_S^0 not following the thermal model of hadron gas is not statistically significant. Also in the analysis of the temperature of the neutral kaons no strong statement can be made. The situation would be clarified with the measurement at energy $\sqrt{s} = 60$ AGeV.

The neutral baryons did not reach the precision needed for the definitive comparison. More effort on the data analysis is needed for the solution of the discrepancies present in SPS data.

Summarizing, the main progress of this work is the precision measurement of the neutral kaon and the clarification of the experimental status. This measurement is an important step in the ambitious plan of building a database of strangeness production. The future project that will shed more light on the subject is the K_T^+ reconstruction. This work in progress in the CERES collaboration will give the spectrum and the precision ratio of the K^+/K^- . This ratio with cooperation of the measurement provided here can clarify the charged kaon production. Additional results can be obtained by reprocessing and the analysis of the short runs at beam momentum of 40 GeV/c and 80 GeV/c per nucleon with programs discussed in this thesis.

The new data on the energy region discussed will come from the energy scan of the RHIC collider and in the future, high statistics will be collected with new FAIR project currently under development. At the same time new opportunities will appear at the new LHC collider with the ALICE experiment under construction. In the new energy regime the strongly interacting matter will be studied with hadrochemistry and penetrating probes.

List of Figures

1.1	Historical plot (1983) of phase diagram of the nuclear matter in equilibrium and how it can be explored by ultra-relativistic heavy ions collisions [6]. For current version see Fig. 1.2.	2
1.2	Left: phase diagram of nuclear matter studied by LQCD and the experiments. Right: energy dependence of the temperature and the baryochemical potential. Plots from Ref. [9].	4
1.3	Particle ratios in data and thermal model at top RHIC energy. Good agreement between data and the thermal model is visible. Plot from Ref. [9] . .	6
1.4	Particle ratios as a function of the energy in the center of mass. The black line represents prediction of the parametrized thermal model [9]. The points show experimental data. In the SPS region the full points show NA49 values while the open points show the NA44 values for charged kaons and the NA57 values for hyperons. Plot from Ref. [9].	8
1.5	Prediction of the strangeness production systematics within the SMET, the plot is from Ref. [12]. Closed points: data from heavy ion experiments, open points: scaled nucleus-nucleus interactions. For definition of Fermi energy F and strangeness to entropy ratio E_s see text.	9
1.6	Temperature of charged kaons as a function of the collision energy. Closed symbols: heavy ion experiments, open symbols: nucleus-nucleus experiments. Plots from Ref. [13].	10
1.7	Transverse mass spectrum of ϕ mesons reconstructed in hadronic and leptonic channels at top SPS energy. Plot from Ref. [19].	12
2.1	The CERES setup.	20
2.2	The CERES Time Projection Chamber.	21
2.3	Left: number of events per burst. Right: number of files per calibration unit.	22

3.1	Acceptance in the transverse momentum – rapidity space. Upper row: K_S^0 decaying before the TPC (left) and the SD (right). Lower row: K_τ^+ decaying before the TPC (left) and the SD (right)	28
3.2	Longitudinal coordinate of the decay vertex for K_S^0 (left) and K_τ^+ (right)	29
3.3	Distribution of $\beta\gamma$ for K_S^0 (left) and K_τ^+ (right). The red line is for the setup with the TPC only and the black for the setup with the TPC+SD. Histograms are scaled to fit in the integral.	30
3.4	Estimation on the invariant mass resolution for K_S^0 (left) and K_τ^+ (right).	30
3.5	Combinatorial background for 2–body K_S^0 decay (left) and 3–body K_τ^+ decay (right). A red box represents the position of the kaon peak.	32
4.1	Before-after protection. Time to the previous (left) and to the next event (right)	39
4.2	Geometry of two approaching nuclei in the transverse plane	40
4.3	Signal from Multiplicity Counter. Black histogram: minimum bias data, red histogram: uncalibrated central data (arbitrary scaling), blue lines show multiplicity cuts corresponding to centrality of 50%, 20% and 7% of the geometrical cross section.	41
4.4	Calibrated centrality of the collected events, left panel shows the full spectra while the right is zoom on central events.	42
4.5	Multiplicity in the TPC.	43
4.6	Number of events after consecutive cuts for data sample in the production prod012	43
4.7	Number of events after consecutive cuts for data sample in the production prod013	44
4.8	Distribution of the number of fitted hits as a function of the polar angle	44
4.9	Distribution of the number of hits for positive (left) and negative (right) tracks. Shaded area shows the selected region	45
4.10	Distribution of the polar angle for positive (left) and negative (right) tracks. Shaded area shows the selected region	45
4.11	Distribution of the transverse momentum for positive (left) and negative (right) tracks. Shaded area shows the selected region	46

4.12	Number of tracks passing quality cuts	47
4.13	Invariant mass spectrum. Red points: same events, black points: mixed events scaled to match in integral.	49
4.14	Invariant mass spectra. Top left: ratio of same to scaled mixed events with the unity subtracted, Top right: mixed events subtracted from same events. Bottom row: the same data zoomed on the region of K_S^0	50
4.15	Small opening angle effects. Ratio of the distribution of $(\Delta\phi, \Delta\theta)$ of pairs in same over mixed events. Left panel: using ϕ_{R2M} , right panel: using $\phi_{firstHit}$	51
4.16	Correlation of multiplicity of positive and negative particles. Left panel: same events, right panel: mixed events	52
4.17	Correlation between momentum and multiplicity. Left panel: positive tracks, right panel: negative tracks.	53
4.18	Correlation between multiplicity and transverse momentum. Left panel: positive particles, right panel: negative particles.	54
4.19	Multiplicity distribution of positives (left) and negatives (right) tracks.	55
4.20	Multiplicity – momentum correlation for positive tracks	55
4.21	Total momentum asymmetry, left panel: directed flow, right panel: elliptical flow	59
4.22	Invariant mass spectrum of the Λ misidentified for K_S^0 . Left: invariant mass vs. polar angle of the proton. Right: mass spectrum of the Λ s in the CERES acceptance.	60
4.23	Armenteros-Podolanski plot. Same events (left) and the significance of the difference between same and mixed events (right)	62
4.24	Armenteros-Podolanski plot after the cut.	63
4.25	Invariant mass spectrum of $\pi^+\pi^-$ pairs. left: same and mixed events, right: ratio of same to mixed events after subtracting the unity.	64
4.26	Invariant mass spectrum of this signal of the K_S^0 . The spectrum is fit with the Gaussian to guide the eye.	64
5.1	Single track efficiency in a function of the polar and azimuthal angle. Left top: efficiency as a function of azimuthal angle with chamber structure visible. Right top: efficiency as a function of polar angle. Bottom: efficiency as a function of the polar angle zoomed on the borders of the acceptance.	72

5.2	Single track efficiency. Left top: efficiency as a function of total momentum. Right top: efficiency as a function of the longitudinal momentum. Bottom: efficiency as a function of transverse momentum for two definition of the fiducial volume: $\theta > 0.12$ rad. (left) and $\theta > 0.13$ rad. (right)	73
5.3	K_S^0 efficiency in rapidity bins as a function of the polar angle cut. Rapidity bins are shown by symbols: (1) – circles, (2) – squares, (3) – pointing up triangles, (4) – pointing down triangles, (5) – chevrons. Left panel: efficiency as a function of the cut. Right panel: efficiency divided by the reference efficiency with $\theta > 0.14$ rad.	74
5.4	Signal, acceptance and efficiency in the rapidity bins	76
5.5	Impact of different cuts. Left panel: a number of events after a given cut, right panel: fraction of events rejected by a given cut.	77
5.6	Impact of different cuts for bins (2)–(4). Left panel: a number of events after a given cut, right panel: fraction of event rejected by a given cut.	77
5.7	Details of the acceptance and efficiency. In consecutive panels: total signal expected in every bin, efficiency of decay topology, acceptance due to polar angle cut, acceptance due to Armenteros cut, efficiency due to track reconstruction and due to resolution of the mass. Rapidity bins depicted in colors: (2) – black, (3) – red, (4) – green, (5) – blue.	78
5.8	Overall efficiency and the correction factor, colors as in Fig 5.7.	80
5.9	Invariant mass spectra for rapidity bin $y \in (2 - 2.15)$. Consecutive panels show transverse momentum bins.	81
5.10	Invariant mass spectra for rapidity bin $y \in (2.15 - 2.30)$. Consecutive panels show transverse momentum bins.	82
5.11	Invariant mass spectra for rapidity bin $y \in (2.30 - 2.45)$. Consecutive panels show transverse momentum bins.	83
5.12	Parameters of the Gaussian fit to invariant mass spectra. Top: reconstructed mass using combined momentum (left) and <i>pcor3</i> (right). Bottom: peak resolution using combined momentum (left) and <i>pcor3</i> (right)	84
5.13	Peak extraction efficiency for two methods and two types of momentum. Top: integral of the Gaussian fit for combined momentum (left) and <i>pcor3</i> (right). Bottom: counting the entries using combined momentum (left) and <i>pcor3</i> (right)	86

6.1	Signal spectrum for four rapidity bins with the fit. The number on the figure shows the raw yield.	90
6.2	Extracted raw yield for four rapidity bins. The red points show the signal extracted from the best spectrum, the black points shows the mean value from the normalization scan.	91
6.3	Crosscheck of the raw yield extraction for all rapidity bins. Left panel: black – total signal in a rapidity bin, red – sum of signal in (p_T, y) bins. Right panel: difference between two methods normalized to statistical fluctuations.	93
6.4	Fit parameters: reconstructed mass and the mass resolution for four rapidity bins. Data are drawn as black points and Monte-Carlo as blue.	94
6.5	Transverse momentum and transverse mass spectrum for four rapidity bins.	95
6.6	Summary: the yield dN/dy obtained from the fit and by integration of the points. Temperature in the rapidity bins.	98
6.7	Stability of the Boltzmann fit. Left column: reconstructed yield as a function of the starting bin. Right column: reconstructed temperature. The rows are for rapidity bins. See text for details of fitting procedure.	100
6.8	Residuals of data points with respect to the fit for four rapidity bins. See text.	101
6.9	Results with different mixing strategy and cuts on the opening angle. Left: rapidity spectrum, green line: the reference data, red line: fit with constrained width, blue line: two-parameter fit. Right: reconstructed temperature in rapidity bins	102
6.10	Results obtained with the transverse momentum cut of $p_T > 0.15$ GeV/ c . Left: rapidity spectrum, green line: the reference data, red line: fit with constrained width, blue line: two-parameter fit. Right: reconstructed temperature in rapidity bins	103
6.11	Final result. Closed point: measured values with statistical errors, open points: reflection at midrapidity, statistical error of the fit is marked by a blue box and the systematic error by red lines.	104
7.1	Transverse momentum spectra for four rapidity bins.	106
7.2	Rapidity spectrum (left) and the reconstructed temperature (right)	106
7.3	Multiplicity density of charged particles dN_{ch}/dy in centrality classes (left panel), multiplicity density per participant (right).	108

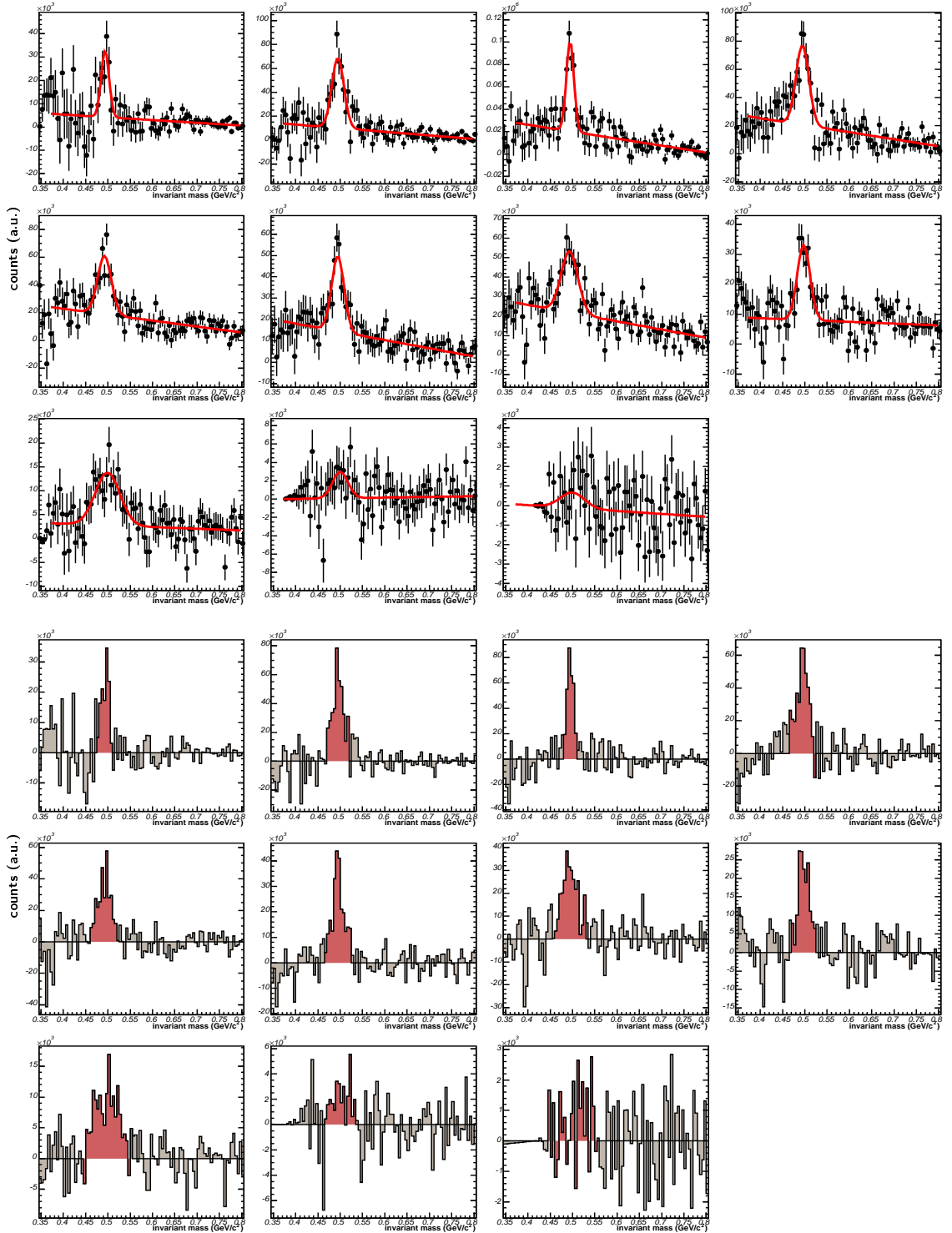
7.4	Comparison of CERES results with NA57. The former results are depicted with red closed points and reflected at midrapidity (open points) and fit with a Gaussian (blue line). NA57 results are depicted with gray points and fit a with gray line. For clarity no reflection at midrapidity is shown. Data from NA57 are from Ref. [23], scaled to CERES centrality.	109
7.5	Results from NA57. Left panel: acceptance for K_S^0 . Right panel: yield of K_S^0 for 5 centrality classes, note consistent width of all spectra. All plots from Ref. [23]	110
7.6	Comparison of CERES results with the mean value of the charged kaons from NA49 and preliminary results on neutral kaons. The CERES points are depicted in red, with the red fit. The NA49 charged kaons are shown as black points (note two points at midrapidity) and neutral kaons as blue triangles.	111
7.7	Fit of the thermal model to data at top SPS energy. Plot from Ref. [9]. . .	114
7.8	The full rapidity spectrum. The closed symbols represent measured and open symbols reflected points. The Gaussian fit is extended to range (-1, 7) and two lines show rapidity of the target and of the beam.	115
7.9	Energy density as a function of temperature calculated with lattice QCD. Plot from Ref. [56, 58].	116
7.10	Temperature of kaons. Positive kaons: green, negative kaons: blue, this analysis: red. The error bars represent statistical and systematic errors added linearly.	117
8.1	Acceptance for Λ . Upper panel: expected signal after acceptance cuts, lower panel: acceptance in transverse momentum – rapidity bins.	121
8.2	Λ reconstruction. Left: Armenteros plot, right: invariant mass spectrum, shaded region shows the position of the Λ peak.	122
8.3	Proton–pion invariant mass spectrum. Left panel: the spectrum, same events in black and mixed events in red. Right: ratio of the same events to mixed events, suppressed for unity. The spectra where normalized above the Λ mass.	123
8.4	Signal of the Λ with a Gaussian fit.	124
8.5	Extracted yield. Left column: raw yield, right column: statistical significance of the peak. Rows are for four rapidity bins.	126

8.6	Extracted mass and the resolution. Left column: offset of the reconstructed mass, right column: reconstructed width of the peak, data are depicted in red and the Monte-Carlo value in blue. Rows are for rapidity bins.	127
8.7	Corrected spectra in linear (left) and logarithmic scale (right). The Boltzmann fit with two parameters is depicted in blue and the fit with the common temperature in magenta. The black line shows total correction factor. Fit parameters are displayed on the panels.	128
8.8	Transverse mass spectra for four rapidity bins.	129
8.9	Analysis of the transverse momentum spectrum by fitting subsets of data. See text.	131
8.10	Rapidity spectrum of the Λ yield (left) and of the temperature (right).	132
8.11	Comparison of the Λ spectrum to NA57, the NA57 fit is presented as a black line. Left: linear scale, right: logarithmic scale.	132
8.12	Comparison of the Λ spectrum to NA49, the NA49 is presented as a black line. Left: linear scale, right: logarithmic scale.	133
8.13	Anti-proton – pion invariant mass spectrum. Left: the spectrum from same (red) and mixed pairs (black). Right: the ratio of same to mixed events after normalization.	134
8.14	$\bar{\Lambda}$ peak fit with a Gaussian.	134
8.15	Raw signal of $\bar{\Lambda}$ (left) and Λ (right) in 4 rapidity bins.	136
8.16	$\bar{\Lambda}$ to Λ ratio.	137
8.17	$\bar{\Lambda}$ to Λ ratio, comparison to NA49 (blue points) and NA57 (green line)	137

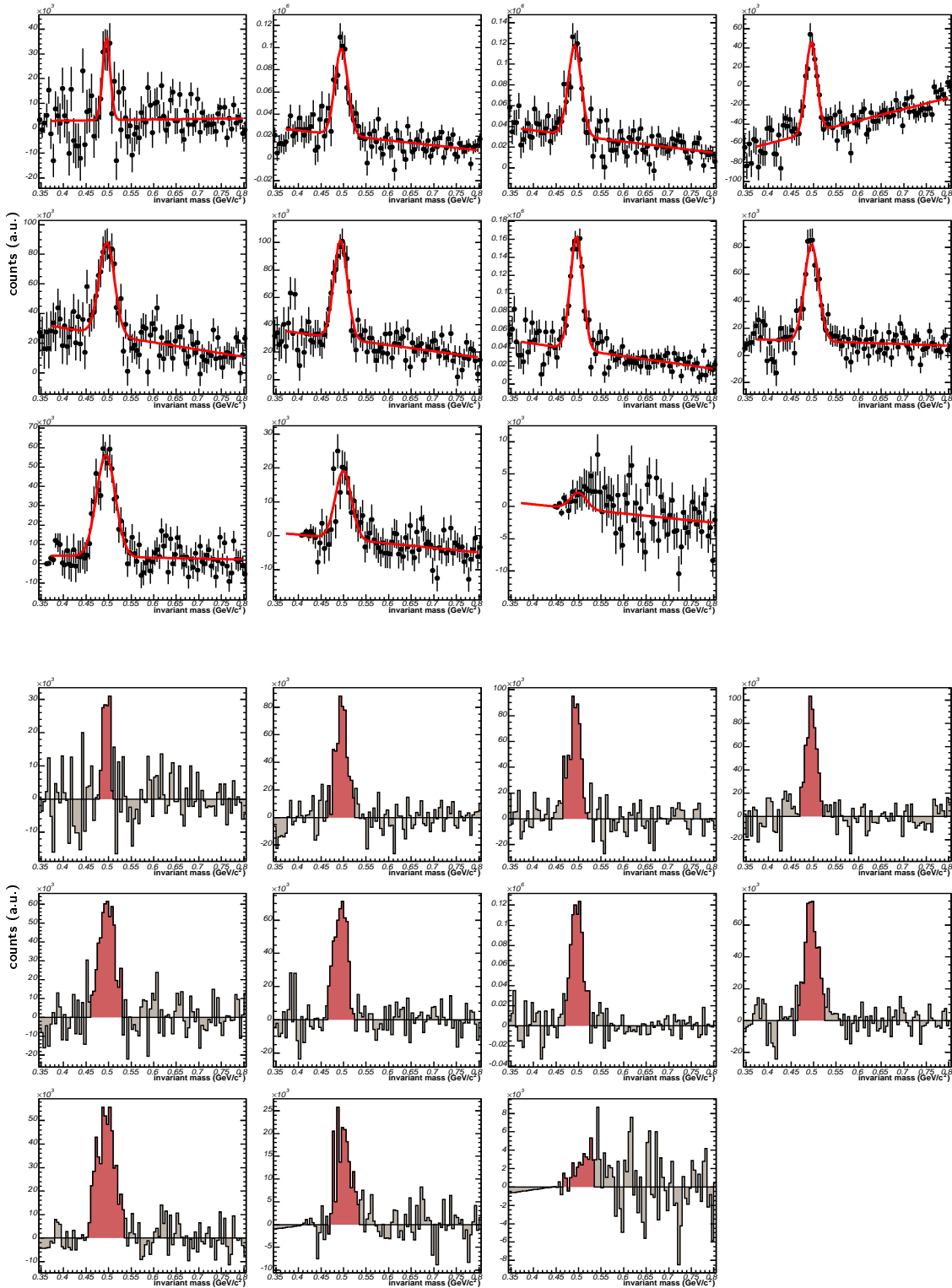
List of Tables

1.1	Compilation of the results on strangeness from NA49 (first column) and NA57 (second column) at top SPS energy. Data obtained or scaled to 5% of geometrical cross-section. The first error is statistical and the second systematic. See text for source of data.	13
2.1	Summary of DAQ system performance	23
2.2	Number of events and files in the step2 and step3c productions	24
3.1	Numerical values for the signal, background and significance.	31
4.1	Trigger codes and the number of triggers	39
7.1	Parameters of the collisions obtained from the Glauber model	108

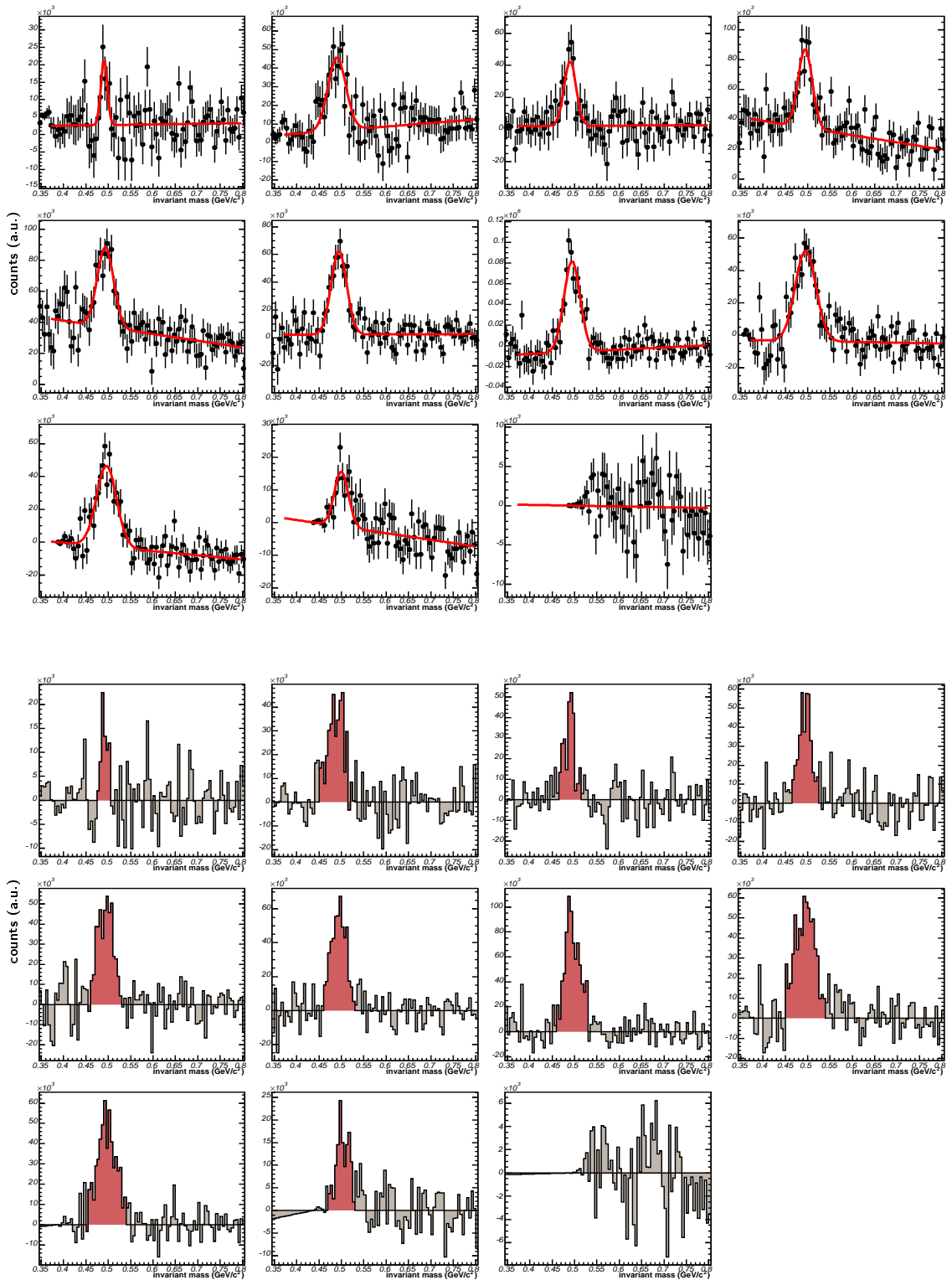
Appendix A: Raw signal of K_S^0



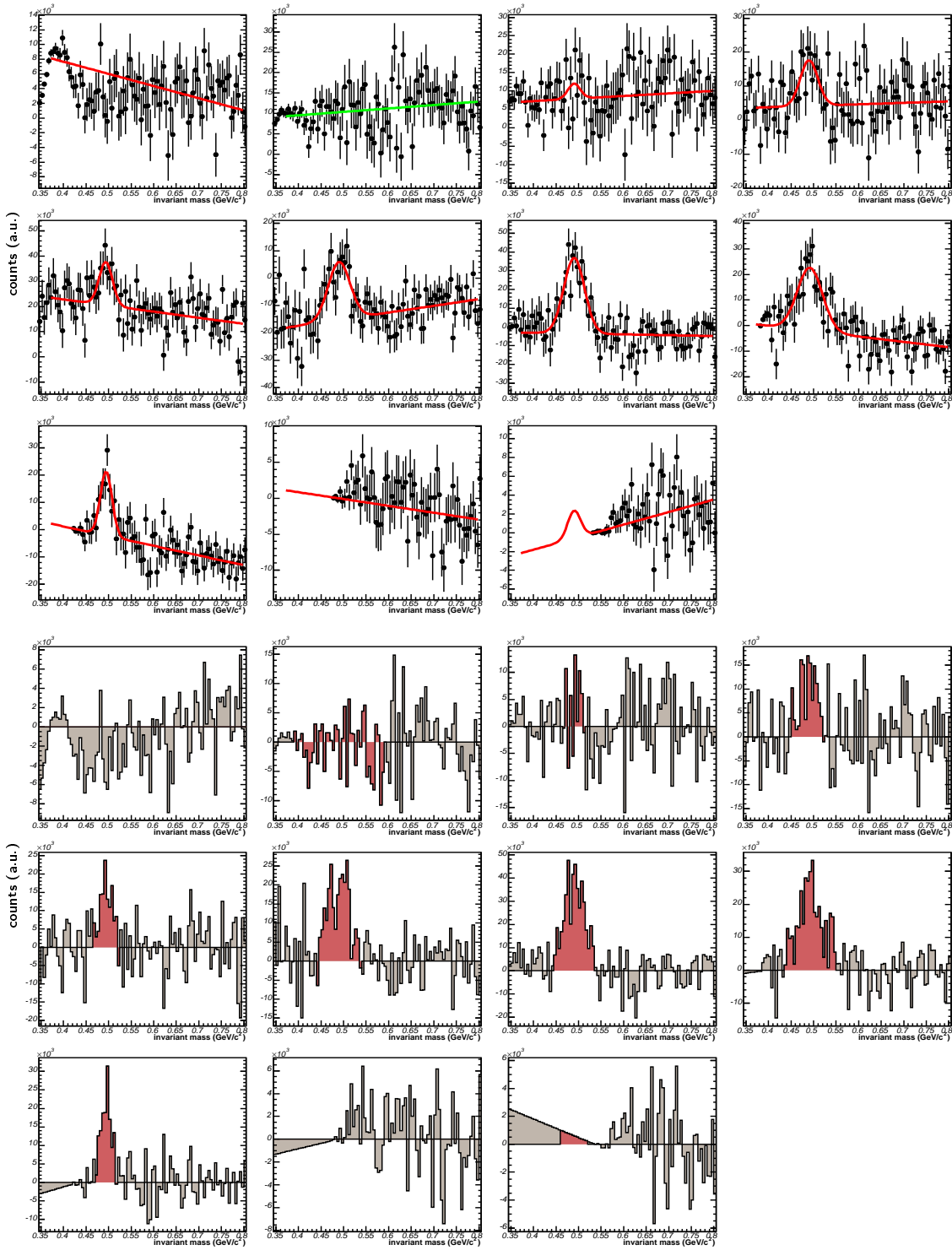
Signal in the invariant mass spectrum for rapidity range (2.00 – 2.15)



Signal in the invariant mass spectrum for rapidity range (2.15 – 2.30)



Signal in the invariant mass spectrum for rapidity range (2.30 – 2.45)



Signal in the invariant mass spectrum for rapidity range (2.45 – 2.60)

Bibliography

- [1] J.D. Bjorken, Phys. Rev. D27 (1983) 140
- [2] H. Satz, Nuclear Physics A715 (2003) 3c-19c
- [3] J. C. Collins and M. J. Perry, Phys. Rev. Lett. 34 (1975) 1353
- [4] N. Cabibbo and G. Parisi, Phys. Lett. 59B (1975) 67
- [5] S.A. Bass, *et al.* Prog. Part. Nucl. Phys. 41(1998) 225-370
- [6] G. Baym, Nucl. Phys. A698 (2002) xxiii
- [7] F. Karsch and E. Laerman, prepared for Quark-Gluon Plasma III, R. Hwa (ed.), hep-lat/0305025
- [8] P. Braun-Munzinger and J. Stachel, J. Phys. G28 (2002) 1971-1976
- [9] A. Andronic, P. Braun-Munzinger and J. Stachel, nucl-th/0511071
- [10] P. Braun-Munzinger, J. Stachel and Ch. Wetterich, Physics Letters B596 (2004) 61-69
- [11] P. Braun-Munzinger, K. Redlich and J. Stachel, prepared for Quark-Gluon Plasma III, R. Hwa (ed.), nucl-th/0304013
- [12] M. Gazdzicki and M. I. Gorenstain, Acta Phys. Polon. B30 (1999) 2705
- [13] R. Stock, J. Phys. G30 (2004) S633-S648
- [14] S. Eidelman, *et. al.*, Physics Letters B592 (2004) 1
- [15] L. Hoddeson (editor) *at al.*, The Rise of the Standard Model: Particle Physics in 1960s and 1970s, Cambridge, 1997
- [16] M. Gell-Mann and A. Pais, Phys. Rev. 97, 1387 (1955)
- [17] K. Lande, E. T. Booth, J. Impeduglia, L. M. Lederman and W. Chinowsky, Phys. Rev. 103 (1956) 1901-1904

- [18] K. Lande, L. M. Lederman and W. Chinowski, Phys. Rev. 105 (1057) 1925-1927
- [19] D. Adamova, *et al.* (CERES Collab.) nucl-ex/0512007
- [20] B. Alessandro, *at al.* (NA50 Collab.) Phys. Lett. B 555 (2003) 147
- [21] S.V. Afanasiev, *at al.* (NA49 Collab.) Phys. Lett. B 491 (2000) 59
- [22] M. Gazdzicki, Compilation of NA49 results, private communication
- [23] F. Antinori, *et al.* (NA57 Collab.) J. Phys. G31 (2005) 1345
- [24] G. Agakichiev, *at al.* (CERES Collab.) Eur. Phys. J. C41 (2005) 475-513
- [25] A. Marin (for the CERES Collab.) J. Phys. G30 (2004) S709-S716
- [26] see: <http://www.mysql.com>
- [27] T. D. Lee and C. N. Yang, Phys Rev. 105 (1957) 1671-1675
- [28] R. Brun and F. Rademakers, Nucl. Inst. & Meth. in Phys. Res. A 389 (1997) 81-86.
See also <http://root.cern.ch>
- [29] G. Krobath, Reconstruction of decay vertices of K_S^0 mesons at the CERES-experiment, diploma thesis, University Heidelberg, 2004.
- [30] W. Ludolphs, Measurement of Open Charm in 158 AGeV/c Pb-Au Collisions, dissertation, University Heidelberg, February 2006.
- [31] C. Adler *at al.* Nucl. Instrum. Meth. A 470 (2001) 488-499
- [32] D. Miskowiec, Centrality calibration of the CERES '2000 data, CERES internal note
- [33] C.A. Ogilvie, Nucl. Phys. A698 (2002) 3c-12c
- [34] G. Agakishiev, *et al.* (CERES Collab.) Nucl. Phys. A638 (1998) 467-470
- [35] K.H. Ackermann, *et al.* (STAR Collab.) Phys. Rev. Lett. 86 (2000) 402-407
- [36] A.M. Poskanzer and S.A. Voloshin, Phys. Rev. C 58 (1998) 1671-1678
- [37] M. Csanada, *et al.* Nucl. Phys. A742 (2004) 80-94
- [38] J. Adams, *at al.* (STAR Collab.) Phys. Rev. C 72 (2005) 014904
- [39] J. Podolanski and R. Armenteros, Phil. Mag. 45 (1954) 13.
- [40] H. Appelshauser, *et al.* (CERES Collab.) Nucl. Phys. A 752 (2005) 394-397

- [41] P. Fachini, Nucl. Phys. A 715 (2003) 462c-465c
- [42] R. Brun, F. Bruyant, M. Maire, A.C. McPherson and P. Zancarini, *GEANT3 User Guide*, CERN Data Handling Division DD/EE/84-1
- [43] see: <http://mathworld.wolfram.com/Chi-SquaredDistribution.html>
- [44] J. Milosevic, Strange Particle Production and Elliptic Flow from CERES, Strange Quark Matter Conference, Los Angeles, 2006
- [45] F. Antinori, *et al.* (NA57 Collab.) J. Phys. G30 (2004) 823
- [46] F. Antinori, *et al.* (NA57 Collab.) J. Phys. G31 (2005) 321
- [47] A. Mischke, *et al.* (NA49 Collab.) Nucl. Phys. A715 (2003), 453
- [48] S.V. Afanssiev *et al.* (NA49 Collab.) Phys. Rev. C66:054902,2002
- [49] D. Miskowiec for the CERES Collab., nucl-ex/0511010
- [50] R. Glauber, Opening talk of Quark Matter Conference, Budapest 2005
- [51] K.J. Eskola, K. Kajantie and J. Lindfors, Nucl. Phys. B323 (1989) 37
- [52] <http://www-linux.gsi.de/~misko/overlap>
- [53] D. Miskowiec, Charge particle multiplicity in the CERES '2000 data, CERES internal note, 2005
- [54] A. Andronic, private communication
- [55] M.D. Baker, *at al.* (PHOBOS Collab.) Nucl. Phys. A715 (2003) 65c
- [56] F. Karsch, Lect. Notes Phys. 583 (2002) 209-249
- [57] L. Van Hove, Phys. Lett. B118 (1982) 138
- [58] A. Andronic and P. Braun-Munzinger, hep-ph/0402291
- [59] A. Mischke, *et. al* (NA49 Collab) J. Phys. G 28 (2002) 1761-1768

Curriculum Vitae

Personal Data

Name	Sylwester
Surname	Radomski
Place of Birth	Otwock, Poland
Date of Birth	May 6, 1977
Marital Status	married, one child
Nationality	Polish

Education

09/1992 – 05/1996	XVIII Lyceum (Secondary School), Warsaw, Poland major: Mathematics and Computer Science
10/1996 – 11/2001	Faculty of Applied Physics and Mathematics, Warsaw University of Technology, Warsaw, Poland major: Computer aided Physics
05/2002 – 06/2006	Fachbereich Physik, Technische Universität Darmstadt Doctoral study

Research experience

07/1999 – 08/1999	Ecole des Mines de Nantes, Nantes, France Summer Student program
07/2000 – 12/2000	Brookhaven National Laboratory, New York, USA Summer Student in the STAR experiment
01/2002 – 05/2006	Gesellschaft für Schwerionenforschung, Darmstadt Doctoral fellowship and preparation of the thesis

Acknowledgments

I am sincerely indebted to my supervisor Prof. Dr. P. Braun-Munzinger for the opportunity to join the KP1 group at GSI and even more for many discussions on physics and data analysis.

My work is based on achievements of other people who built, run, and calibrated the CERES experiment. I am grateful to all the members of CERES for this effort in particular to the spokesperson Prof. Dr. J. Stachel.

I acknowledge discussions with Dr. D. Miskowiec, which led to improvement of the presented analysis. I would also like to thank Dr. A. Marin for introducing me to the CERES Monte-Carlo and the COOL software. I appreciate the help of Dr. A. Andronic with many discussions on the thermal model and data interpretation. I thank him also for the critical review of the text. I would like to thank all the people who read, commented and corrected this manuscript including in particular Dr. Kim Langfelder.

In my early days at GSI I worked on the development of software for the ALICE experiment (not discussed in this thesis). I would like to take the opportunity to thank my collaborators of that time, Dr. Y. Foka, Prof. Dr. A. Sandoval, and Prof. Dr. C. Blume.

I would like to take the opportunity to thank all the people who created computing tools for data analysis. I would like to thank ROOT team for the great framework and the computing division at GSI for the maintenance of the batch farm and data servers.

I am also indebted to the members of GSI CERES and ALICE TRD groups for many stimulating discussions during the lunch and coffee breaks.

Finally, I would like to thank my wife and my daughter for the support during the work on the results presented here.

Erklärung

Hiermit erkläre ich an Eides statt, daß ich die vorliegende Dissertation selbständig verfaßt, keine anderen als die angegebenen Hilfsmittel verwendet und noch keinen Promotionsversuch unternommen habe.

Darmstadt, den 12. Mai 2006,

gez. Sylwester Radomski

Unterschrift

